

# **JOURNAL OF HYDRO - METEOROLOGY**

**ISSN 2525 - 2208**



**VIETNAM METEOROLOGICAL AND  
HYDROLOGICAL ADMINISTRATION**

**No 20  
09-2024**



**Acting Editor-in-Chief**  
**Assoc. Prof. Dr. Doan Quang Tri**

- |                                      |                                   |
|--------------------------------------|-----------------------------------|
| 1. Prof. Dr. Tran Hong Thai          | 13. Assoc.Prof.Dr. Doan Quang Tri |
| 2. Prof. Dr. Tran Thuc               | 14. Assoc.Prof.Dr. Mai Van Khiem  |
| 3. Prof. Dr. Mai Trong Nhuan         | 15. Assoc.Prof.Dr. Nguyen Ba Thuy |
| 4. Prof. Dr. Phan Van Tan            | 16. Dr. Tong Ngoc Thanh           |
| 5. Prof. Dr. Nguyen Ky Phung         | 17. Dr. Dinh Thai Hung            |
| 6. Prof. Dr. Phan Dinh Tuan          | 18. Dr. Vo Van Hoa                |
| 7. Prof. Dr. Nguyen Kim Loi          | 19. TS. Nguyen Dac Dong           |
| 8. Assoc. Prof. Dr. Nguyen Van Thang | 20. Prof. Dr. Kazuo Saito         |
| 9. Assoc. Prof. Dr. Duong Van Kham   | 21. Prof. Dr. Jun Matsumoto       |
| 10. Assoc. Prof. Dr. Duong Hong Son  | 22. Prof. Dr. Jaecheol Nam        |
| 11. Dr. Hoang Duc Cuong              | 23. Dr. Keunyoung Song            |
| 12. Dr. Bach Quang Dung              | 24. Dr. Lars Robert Hole          |
|                                      | 25. Dr. Sooyoul Kim               |

### **Publishing licence**

No: 166/GP-BTTTT - Ministry of Information and Communication dated 17/04/2018

### **Editorial office**

No 8 Phao Dai Lang, Dong Da, Ha Noi  
 Tel: 024.39364963  
 Email: tapchikttv@gmail.com

### **Engraving and printing**

Ha Thanh Thang Long Printing And Trading Joint Stock Company  
 Tel: 0243.2022639

## **JOURNAL OF HYDRO-METEOROLOGY** **Volume 20 - 9/2024**

### **TABLE OF CONTENT**

- 1** **Ninh, L.V.; Tuan, N.H.; Tuan, N.C.; Anh, L.N.; Giang, N.T.; Van, C.T.** Applying a two-dimensional open-source hydrodynamic model to evaluate the riverbed change in the upstream of the Cuu Long River, An Giang Province
- 15** **Phuc, L.Q.; Ha, L.T.T.; Long, N.Q.** Stress distribution under coal pillars in the case of multi-seam mining: A case study at Thong Nhat Coal Mine, Vietnam
- 24** **Ha, L.T.T.** Multi-sensor points cloud data fusion for 3D building models: A case study in Halong city, Vietnam
- 37** **Nhu, N.Y.** A review on baseflow separation methods
- 52** **Hai, K.V.; Giang, N.T.; Bich, D.T.N.** Applying the variable infiltration capacity (VIC) model to reconstructing streamflow data in the Da River basin at Muong Te hydrological station
- 66** **Trung, D.T.** The integration of GNSS RTK and IMU with extended particle filter
- 75** **Duyen, L.Q.** Application of geomechanical models to predict sand production and propose well completion solutions for Well X in the Hai Thach field
- 84** **Trang, T.N.H; Duc, D.N.; Trung, L.V.; Phu, V.L.** Combining UAV and satellite images to assess forest changes: A case study in Phuoc Thuan commune, Xuyen Moc district, Ba Ria - Vung Tau Province in the period 2020-2023

*Research Article*

# Applying a two-dimensional open-source hydrodynamic model to evaluate the riverbed change in the upstream of the Cuu Long River, An Giang province

Luu Van Ninh<sup>1,3</sup>, Nguyen Huu Tuan<sup>2,3</sup>, Ngo Chi Tuan<sup>3</sup>, Le Ngoc Anh<sup>4</sup>, Nguyen Tien Giang<sup>3</sup>, Can Thu Van<sup>2\*</sup>

<sup>1</sup> An Giang Provincial Hydro-Meteorological Center; luuninhtv@gmail.com

<sup>2</sup> HCMC University of Natural Resources and Environment; nhtuan@hcmunre.edu.vn; ctvan@hcmunre.edu.vn

<sup>3</sup> Hanoi University of Science, VNU; giangnt@vnu.edu.vn; ngochituan@gmail.com

<sup>4</sup> Vanlang University; anh.lengoc@vlu.edu.vn

\*Corresponding author: ctvan@hcmunre.edu.vn; Tel.: +84–983738347

Received: 28 March 2024; Accepted: 06 May 2024; Published: 25 September 2024

**Abstract:** Riverbank erosion in the Mekong Delta, particularly along the Tien and Hau rivers and some primary and secondary tributaries, is undergoing highly complex and unpredictable changes, resulting in significant damage to the affected areas. The phenomenon of riverbank erosion here is caused by multiple factors, including intensified human activities such as sand mining, infrastructure development, and climate change. In recent years, the increasing activities of upstream Mekong River projects have led to a reduction in sediment deposition in the delta, which is considered one of the significant contributing factors to the increasing incidence of riverbank erosion. This paper will apply and build a two-dimensional open-source model (TELEMAC) to simulate in detail the sediment transport process during the 3-year period from 2017 to 2019 on the upstream section of the Tien and Hau rivers in An Giang province to evaluate and assess the sediment imbalance during this period and identify trends in riverbed erosion and deposition. As a result, in 3 years, the total silt deficit on the Tien River section is  $-36.6 \times 10^6 \text{ m}^3$ , on the Hau River is  $-2.7 \times 10^6 \text{ m}^3$ . At the same time, the erosion depth deepened by approximately 0.25–0.75 m (especially up to 1.0 m). This indicates an imbalance in sediment deposition and erosion, with a consistent trend of riverbed, banks, and shore erosion.

**Keywords:** Sediment transport; River bed evolution; TELEMAC 2D model.

## 1. Introduction

The Mekong Delta is the downstream of the Mekong river basin with an area of 40.9 thousand km<sup>2</sup>. This place has a dense river network, and its tributaries are quite complex. In the upstream of the Mekong River (Tan Chau - Tien River) and (Chau Doc - Hau River), where the two rivers flow into the delta, their width is about 60 m to 300 m and gradually widens to about 2-3 km in downstream. An Giang province is one of the two upstream provinces of the Mekong Delta receiving water from the Tien and Hau rivers from Cambodia. This province has a dense system of rivers and canals: Tien River, Hau River, Vam Nao River, Binh Di River, Chau Doc River along with large canals such as Xang Tan An Canal, Ong Chuong Canal, Xep Nang Gu... are the streams main and important watercourses. These main rivers and canals are experiencing changes in their riverbeds, causing complex erosion and riverbank landslides, causing the loss of dozens of hectares of land each year, causing

major consequences for life and property in the economic areas and residential areas along the river. In recent years, under the increasing adverse impacts of flow regimes as well as human activities, riverbank erosion has become more and more complicated and more frequent. This will be even more serious in the future because of climate change impacts from upstream development. The riverbank in An Giang province has quite strong and complex erosion. Among the 65 communes along the Tien and Hau rivers in An Giang province, there are currently 33 riverbank erosion areas (14 areas along the Tien river and 19 areas along the Hau river). Along both sides of the Tien and Hau rivers, there are districts where landslides occur frequently: An Phu, Phu Tan, Tan Chau, Cho Moi, Chau Phu, etc. Therefore, research, evaluation, and simulation of sand and mud developments and riverbank erosion here receive great attention and concern.

Research on the process of sedimentation and river bed erosion has been carried out and researched for a long time. Scientists around the world have focused research on directions such as: river morphology, river dynamics, modeling, in the laboratory combined with field measurements to determine the causes, mechanisms, and changes in the channel. Based on these, solutions were proposed to prevent and mitigate damages caused by bank erosion and channel sedimentation [1–7]. However, simulating bank erosion is still a challenging problem because the flow of water and sediment through channels changes continuously over time, and the diversity of bank materials in nature. This limits the accuracy of numerical models, which are often calibrated and applied to specifically simulate idealized natural river systems [8]. Furthermore, when integrated with the digital elevation model (DEM), the coarse or fine resolution of this model also greatly affects the accuracy of the model. In addition, the computation time and financial cost to perform the simulation are also very large, especially for large river basins with complex terrain. For example, for braided river sections, such as the Mekong River, the complexity of the problem is still a big challenge for scientists. It is difficult to select an appropriate approach for all cases [9].

Around the world, research has achieved progress in studying sediment transport and sand mining on rivers and has solved many complex practical problems such as: Calculate the sediment balance in the basin to determine sand reserves along the river and each mining location, using mathematical models and statistical methods; Solve economic problems combined with river dynamics problems, to determine the optimal exploitation plan that brings high economic efficiency with little impact on the environment and self-recovery after exploitation period; Combining social issues and harmonizing the rights of subjects in the community are also addressed [10–15], etc.

In Vietnam, riverbank erosion has recently been occurring nationwide, becoming increasingly complicated, directly affecting the lives and property of the people, the State, and prevention and control works. The study [16] has proposed a model to predict the process of erosion - sand and gravel deposition for coastal strips and estuaries at medium temporal scale (seasonal and annual), proposed scientific and technical solutions to prevent erosion and sedimentation and protect estuary coastal structures. The study [17] has identified the causes and mechanisms of evolution (accretion, erosion, displacement) of estuaries along the Central Coast, and proposed solutions to adapt and stabilize estuaries such as Tu Hien river estuary (Thua Thien - Hue), My A river estuary (Quang Ngai), Da Rang river estuary (Phu Yen) for socio-economic development and safety for fishermen and boats to avoid storms. The study [18] researched the rules of estuary evolution and evaluated the ability to escape floods under different evolution scenarios, taking into account sediment transport in the Vu Gia-Thu Bon river estuary. The study [19] has improved HOSODA's 3D model for calculating local erosion in the groin area, which was only applied to the case of bottom mud and unflooded sand, now taking into account the movement of suspended sand and submerged groynes. Applying physical models to experiment with continuous curves, formulas and charts were built to calculate the effectiveness of accretion techniques after circulation reversal works. The study [20] has identified the causes and mechanisms of

formation, movement and sedimentation of the Lai Giang estuary, Binh Dinh province, and proposed solutions to correct and prevent estuary sedimentation and stabilize flood drainage. Another research on forecasting sedimentation and erosion of the Dong Nai - Saigon river channel under the influence of the flood protection system in downstream [21].

For the Mekong Delta, studies [22–25] have researched erosion and sedimentation forecasts and prevention solutions on the river system in the Mekong Delta: Determine the location, scale, and speed of riverbank erosion and identify key erosion areas for the entire Tien and Hau rivers using remote sensing and GIS methods. Quantify causes, erosion mechanisms and factors affecting erosion for the Mekong River in focus areas. Other studies [9, 26–30] have done in-depth research on the causes and mechanisms of landslides in typical study areas on the Tien and Hau rivers and oriented solutions to predict riverbank erosion in the Mekong Delta. The study [31] used Landsat satellite images on the Google Earth Engine platform to study bank erosion of all major rivers in the Mekong Delta for the period 1989 to 2014. The study [32] built a riverbank erosion prediction model based on high-performance computing technology using GPUs combined with implementation based on empirical models and applications for some river sections of the Mekong Delta. The study [33] applied TELEMAC-3D model to simulate flow and sediment transport at the confluence area of the Hau river and the Vam Nao river. The study [28] combined the TELEMAC-2D and MIKE 21 FM models to analyze the causes affecting the level of riverbank erosion. Remote sensing imaging technology was used to analyze and determine the extent of riverbank erosion in the Tien River [34]. Thus, in addition to traditional methods such as: using empirical formulas, physical models, and actual surveys, there are also methods using numerical models, GIS, remote sensing images, etc. Nowadays, there exist many methods that leverage machine learning and artificial intelligence to evaluate the riverbed erosion and aggradation.

Regarding the application of hydrodynamic and sand sediment simulation models in river basins, it shows: 1-2- or 3-D models have been established, calibrated and tested in previous studies as well as within the framework of projects at all levels to see the usefulness of these tools [9, 15–22, 26–27]. However, it is seen that the models differ in terms of usage conditions, input data requirements for the model, level of complexity, computation speed and accuracy. Certainly, no model can be called the best because each model has different advantages and disadvantages. The most important thing is to choose the right model. The main factors affecting model selection include: (i) input and output data of the model, (ii) applicability, (iii) user's purpose, (iv) computer hardware responsiveness, (v) software purchase costs, and (vi) updateability. If considering the six factors to choose the model above, TELEMAC is a very suitable model in this evaluation study, especially suitable for individuals or organizations that do not have the financial ability. The TELEMAC model system has been developed by the National Laboratory of Hydraulics and Environment under the national center for Hydraulic research of Electricity France (EDF) since 1987. This is one of the leading river morphology hydrodynamic models in the world that can respond to forecasting the morphological change process for estuaries and coastal areas. The TELEMAC model has been applied in many studies around the world [35–38]. However, the biggest disadvantage of TELEMAC is that it is difficult to use and requires users to have certain knowledge of hydrodynamics and programming skills. This study applies the TELEMAC model to simulate and analyse the level of riverbed erosion by identifying the lack of sediment and sand in the flow.

## **2. Materials and methodology**

### *2.1. Methodology*

a) Hydrodynamic model (TELEMAC-2D): The TELEMAC-2D model solves the depth-averaged runoff equation based on the two-dimensional Saint-Venant equation [35].

The process of performing the simulation model is shown in Figure 1.

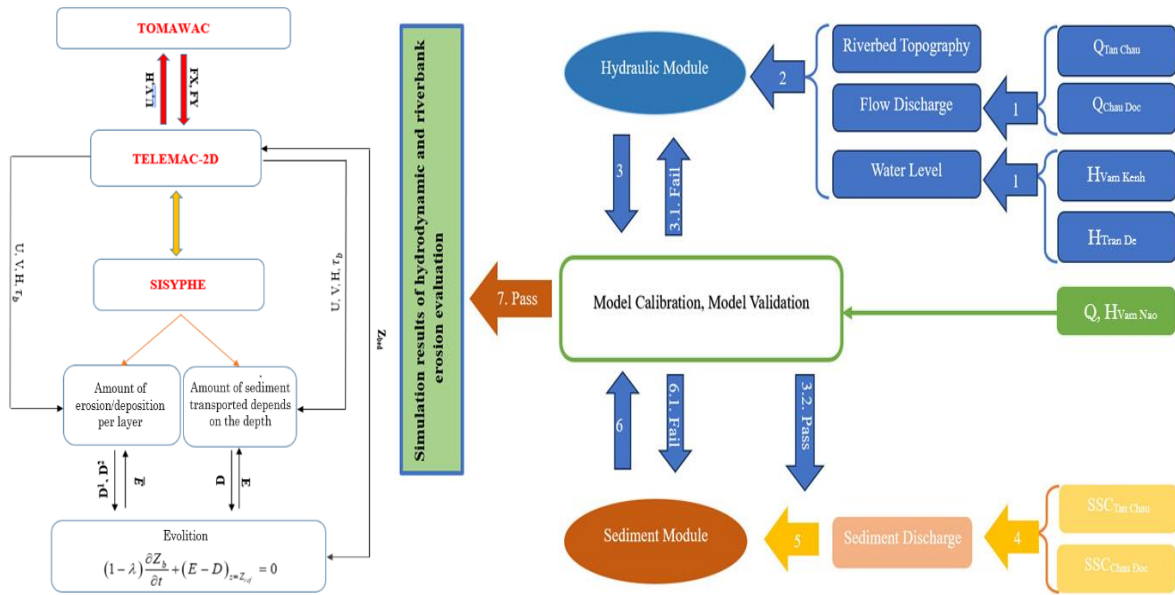


Figure 1. General flowchart of study using TELEMAC model.

Continuous equation:

$$\frac{\partial h}{\partial t} + \vec{u} \cdot \vec{\nabla}(h) + h \operatorname{div}(\vec{u}) = S_h \quad (1)$$

Momentum equation (x direction):

$$\frac{\partial u}{\partial t} + \vec{u} \cdot \vec{\nabla}(u) = -g \frac{\partial Z}{\partial x} + S_x + \frac{1}{h} \operatorname{div}(h v_t \vec{\nabla} u) \quad (2)$$

Momentum equation (y direction):

$$\frac{\partial v}{\partial t} + \vec{u} \cdot \vec{\nabla}(v) = -g \frac{\partial Z}{\partial y} + S_y + \frac{1}{h} \operatorname{div}(h v_t \vec{\nabla} v) \quad (3)$$

where  $h$  is the depth (m);  $u, v$  are the velocity in  $x$  and  $y$  directions (m/s);  $g$  is the gravitational acceleration ( $\text{m/s}^2$ );  $v_t, v_T$  are the momentum diffusion coefficient and substance diffusion coefficient, respectively;  $Z$  is the water level (m);  $S_h$  is the specific discharge (m/s);  $S_x, S_y$  are the external forces acting on a unit mass projected in the  $x$  and  $y$  horizontal directions ( $\text{m/s}^2$ ).

b) Morphodynamic model SISYPHE and Mixed sediment

Sediment transport equation (x and y directions) for vertically averaged suspended sediment concentration  $C = C(x, y, t)$  is described as:

$$\frac{\partial h C_k}{\partial t} + \frac{\partial (h U C_k)}{\partial x} + \frac{\partial (h V C_k)}{\partial y} = \frac{\partial}{\partial x} \left( h \varepsilon_s \frac{\partial C_k}{\partial x} \right) + \frac{\partial}{\partial y} \left( h \varepsilon_s \frac{\partial C_k}{\partial y} \right) + E^k - D^k \quad (4)$$

$$(E^k - D^k)_{Z_{\text{ref}}} = \omega_s (C_{\text{eq}}^k - C_{\text{ref}}^k) \quad (5)$$

The  $k$  is constant ( $k = 1$  - sand,  $k = 2$  - mud grains).

where  $h = Z_s - Z_f \approx Z_s - Z_{\text{ref}}$  is the depth, assuming the thickness of the bottom mud and sand layer is very thin;  $U$  is the average velocity in the  $x$  direction,  $V$  is average velocity in the  $y$  directions;  $E$  is an erosion unit;  $D$ : accretion unit;  $(E - D)$  is the amount of sediment stored;  $C_{\text{eq}}$  is the concentration of sediment in near the bottom;  $C_{\text{ref}}$  is the sediment concentration close to the bottom.

The vertical sediment concentration profile is described by Rouse's formula:

$$C(z) = C_{Z_{\text{ref}}} \left( \frac{z-h}{z} \times \frac{a}{a-h} \right)^R \quad \text{with} \quad R = \frac{w_s}{\kappa u_*} \quad (6)$$

where  $C_{Z_{\text{ref}}} = F \times C$

$$\begin{cases} F^{-1} = \frac{1}{(1-Z)} B^R (1-B^{(1-R)}) \Leftrightarrow R \neq 1 & \text{with } B = \frac{Z_{ref}}{h} \\ F^{-1} = -B \log B \Leftrightarrow R = 1 \end{cases} \quad (7)$$

The change in the riverbed elevation is computed using Exner’s equation as follows:

$$(1-\lambda) \frac{\partial z_b}{\partial t} + (E-D)_{z=Z_{ref}} = 0 \quad (8)$$

where  $\lambda$  is the void coefficient,  $z_b$  is the riverbed elevation.

## 2.2. Data

### a) Input data

Upstream boundary: flow taken at Tan Chau and Chau Doc station, average daily flow data. Average daily sand and sediment concentration range (SSC) taken from Tan Chau and Chau Doc station period 2017-2019 (3 years).

Downstream boundary taken at water level stations at coastal estuaries at Vam Kenh, Ben Trai, Binh Dai, Tran De, average daily water level data period 2017-2019.

Testing boundary used to calibrate and verify hydraulics and silt content were taken at My Thuan and Can Tho hydrological stations.

### b) Establishing domain

The computational domain is an unstructured grid with 124,644 elements and 8,126 nodes covering areas, river channels, and riverbanks. The maximum element length is 40.0 m and the minimum is 5.0 m (Figure 2).

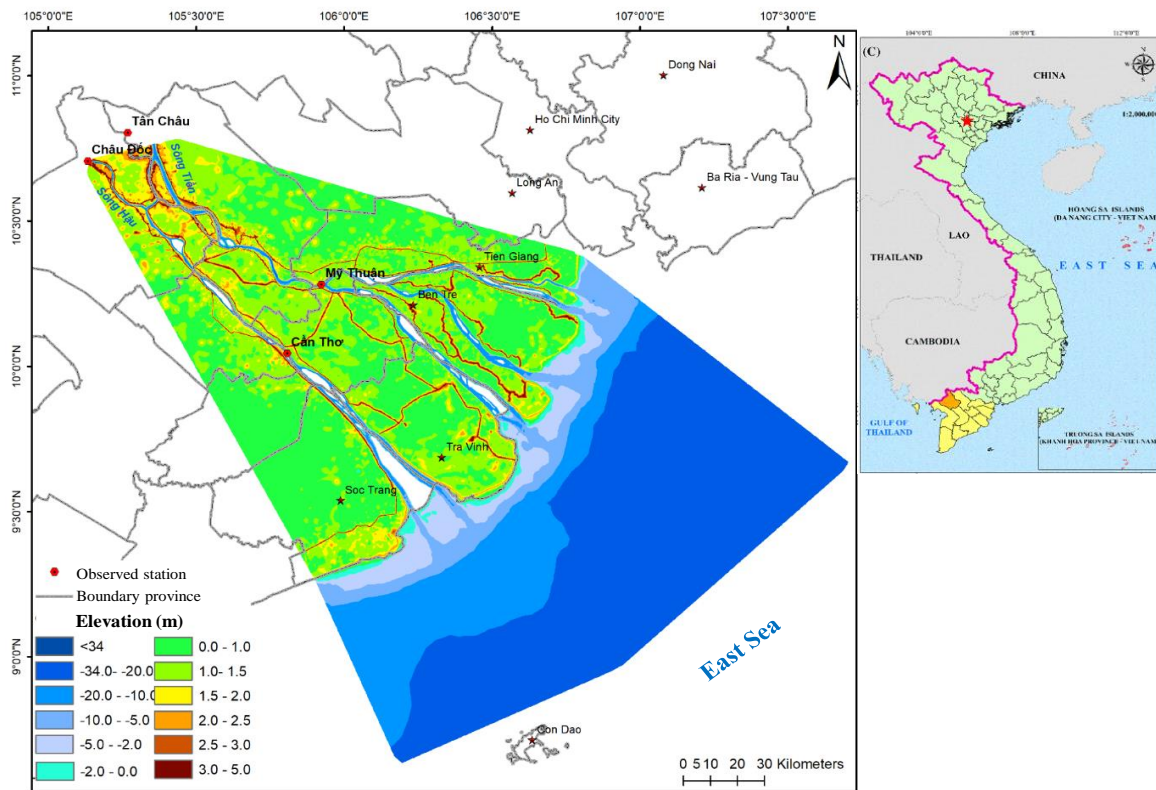
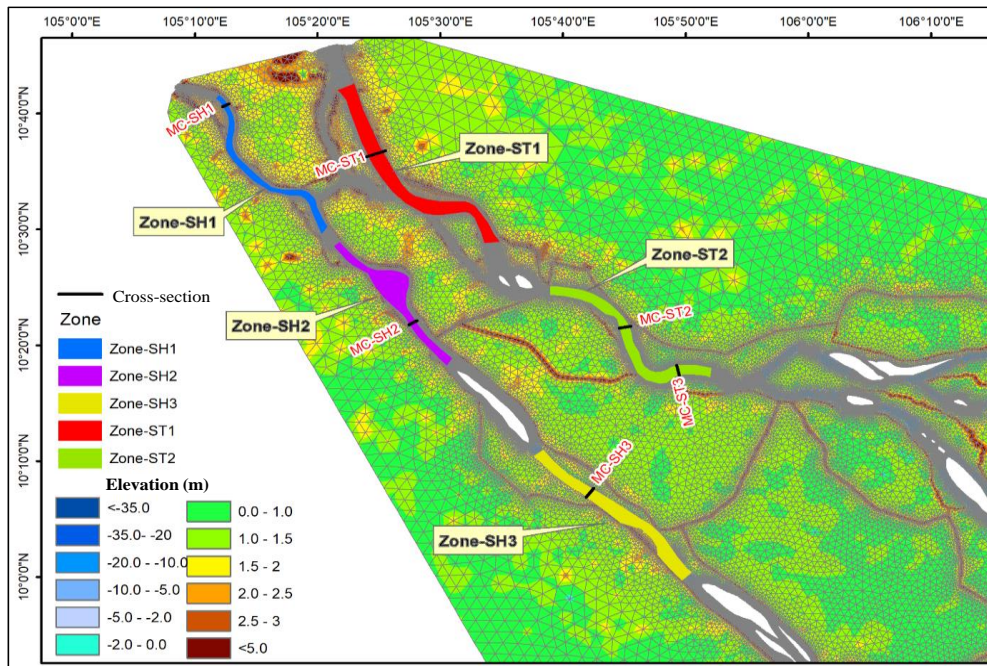


Figure 2. Topography of the computational domain [28].

The terrain data consists of elevation data with a resolution of  $20\text{ m} \times 20\text{ m}$ . Additional surveying and detailed calculations were conducted to refine the riverbed terrain data, achieving a resolution of 3-5 m. The data is inherited from [28]. The model setup is illustrated in the hydraulic schematic (Figure 3). The process, model validation is conducted after model calibration to check the reliability of the selected parameters with changed input factors.

Calculation time: Since there is no measured water level data that coincides with the time of survey, in this study, the period of water level calibration and validation will be chosen different from the time of calibration and validation of flow rate and direction.



**Figure 3.** Research river section (ST1, SH1) and calculation grid.

c) Set of parameters

The model validation process is conducted after adjusting the model to recheck the reliability of selected parameters with changed input factors.

Hydrodynamic model: Manning's friction law is applied with friction coefficients from 0.015-0.032 varying in space.

Sediment transport model: The composition of sand and mud particles on the Tien and Hau rivers is very uneven and complex, ranging from gravel to silt and clay with diameters mainly of particles with diameter  $d = 0.008-8.0$  mm. In this study, the bottom structure is established in the form of mixed sand mud consisting of two sand grain components ( $d = 0.30 \times 10^{-3}m$ ) and mud ( $d = 0.028 \times 10^{-3}m$ ). The sediment content in each layer is:  $C_1 = 160$ ;  $C_2 = 260$  ( $kg/m^3$ ). Sedimentation critical stress  $\tau_b = 1000$  Pa; Erosion critical stress  $\tau_{ce1} = 0.022$  N/m<sup>2</sup>,  $\tau_{ce2} = 0.26$  N/m<sup>2</sup>, the settling velocity of sand and mud particles is  $v_s = 0.15$  mm/s (sand) and  $v_s = 0.035$  mm/s (mud) corresponding to sand and mud composition. The active layer is set to 0.05 m and the simulation time step is 120s.

The simulation results of the numerical model depend greatly on the simulation parameters and these parameters are gradually accurate through the model calibration process. The basic parameters are summarized in Table 1.

**Table 1.** The parameters in the model TELEMAC-2D - Sisyphe.

Parameter	Value	Unit
Model TELEMAC2-D (Hydrodynamic)		
Law of friction	4 (Manning's)	
Friction coefficient	0.015-0.030	m <sup>1/3</sup> /s
Turbulence model	2 (Elder)	
Kinematic viscosity coefficient	10-Jun	m <sup>2</sup> /s
Secondary currents	<input checked="" type="checkbox"/>	
Tidal Flats	<input checked="" type="checkbox"/>	



Parameter	Value	Unit
Model SISYPHE (Sediment transport)		
Sediment characteristics	Mixed sediment	
Grain diameter	0.33 (sand); 0.035 (mud)	mm
Grain porosity	0.37	
Bed layer	2	
Active layer	0.05	m
Sludge content per layer	70; 80 (from top to bottom)	kg/m <sup>3</sup>
Erosion critical stress of mud	0.021; 0.085	N/m <sup>2</sup>
Critical shear velocity for mud deposition	1000	m/s
Partheniades constant	1.5×10 <sup>-4</sup>	kg/m <sup>2</sup> /s
Effect of slope	<input checked="" type="checkbox"/>	
The sediment content is balanced close to the bottom	$C_{eq} = \frac{0.331(\theta' - \theta_c)^{1.75}}{1 + 0.72(\theta' - \theta_c)^{1.75}}$	
Settling velocity	0.15 (sand); 0.035 (mud)	mm/s
Influence of secondary flow	<input checked="" type="checkbox"/>	
Crust friction	$k_s' = 3.6d_{50}$	mm
Time step	120	s

Simulation scenario: According to research, under the condition of a complete upstream hydroelectric system, the amount of sediment and sand reaching Tan Chau and Chau Doc will be reduced by about 80% compared to 2015 [27]. According to the latest report of the Mekong River Commission Secretariat (April 22, 2024, Phnom Penh, Cambodia), the average sand and sediment content (g/l) decreased by 8% in Tan Chau and 5% in Chau Doc [34]. However, these data only reflect the amount of sediment at Tan Chau and Chau Doc stations, it does not show the river morphology relationship, that is, how the sediment imbalance occurs. This study will simulate in detail the sediment transport process during the 3-year period from 2017 to 2019 on the mainstream of the Tien (ST1) and Hau (SH1) rivers in the upstream of An Giang province to evaluate the sediment imbalance and identify trends in riverbed accretion and erosion.

### 3. Results and Discussion

#### 3.1. Results of model calibration and validation

The results of water level calibration and validation are shown in Table 2, Figure 4. The criteria show that the results are good: MSE = 0.2-0.47; ME = 0.05-0.2; Nash = 0.72-0.89.

**Table 2.** Water level error and correlation values.

Station	Min		Max		Average		ME	MAE	MSE	R	NASH
	OBS	SIM	OBS	SIM	OBS	SIM					
Dry season 2018											
Can Tho	-0.87	-1.22	1.42	1.38	0.39	0.19	0.20	0.28	0.32	0.90	0.76
My Thuan	-1.20	-1.24	1.40	1.80	0.28	0.24	0.04	0.21	0.47	0.90	0.85
Flood season 2018											
Can Tho	-0.24	-0.52	1.91	2.15	0.75	0.60	0.15	0.20	0.20	0.96	0.72
My Thuan	-0.84	-1.03	1.79	2.00	0.47	0.42	0.05	0.17	0.33	0.98	0.89

OBS: observation, SIM: Simulation, ME: average absolute error, MAE: average error, MSE: square error, R: Correlation coefficients.

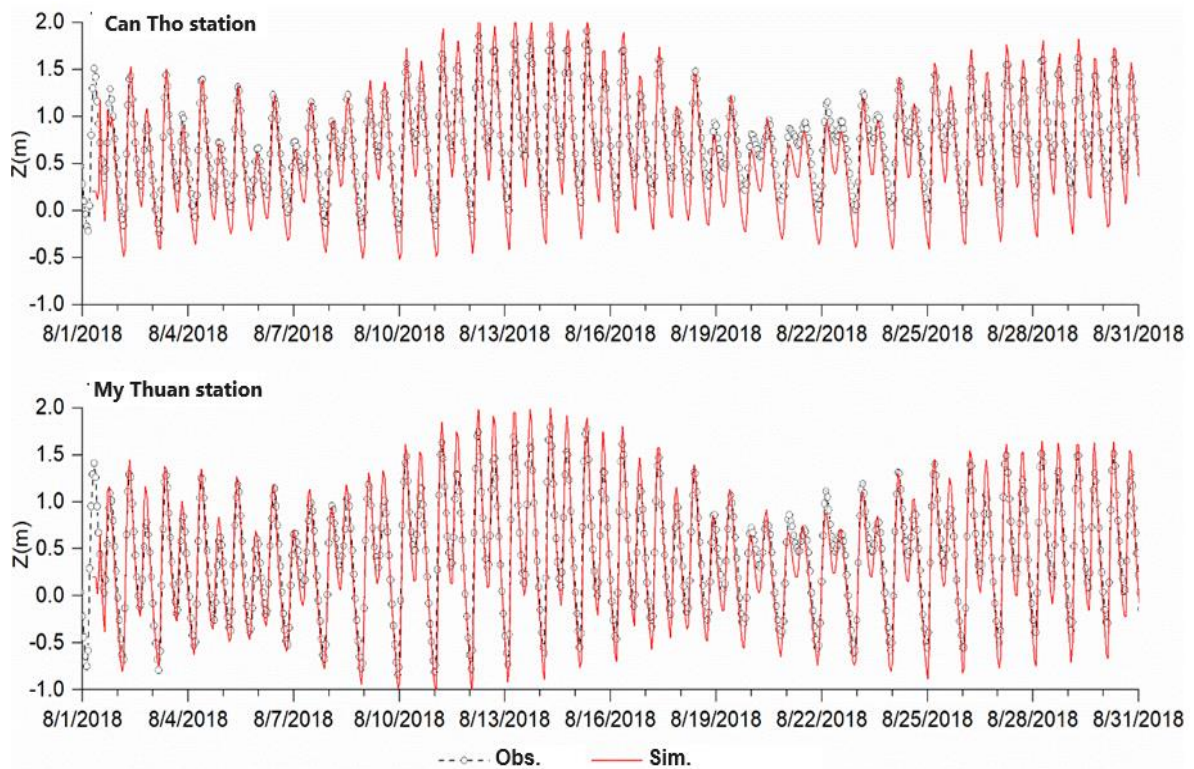


**Figure 4.** Illustration comparing water level process between simulation and actual measurements during the flood season (8/2018).

The results of discharge calibration and validation at Can Tho and My Thuan stations are shown in Table 3, Figure 5. The calibration results give quite good results:  $R = 0.90-0.95$  and Nash = 6.8-0.84.

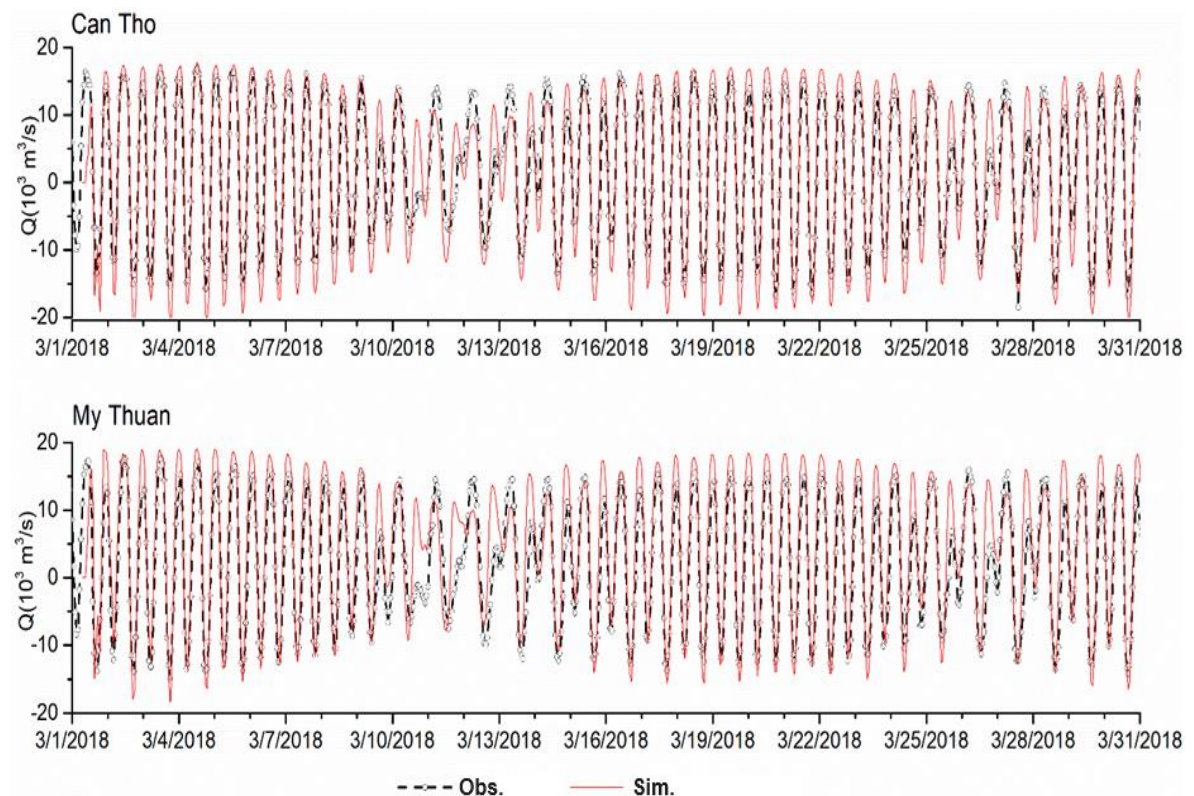


**Figure 5.** Illustration comparing discharge process between simulation and actual measurements during the flood season (8/2018).

**Table 3.** Discharge error and correlation values.

Station	MIN		MAX		TB		ME	MAE	R	NASH
	OBS	SIM	OBS	SIM	OBS	SIM				
Dry season 2018										
Can Tho	-18.5	-21.4	16.8	17.7	2.0	1.8	0.2	3.3	0.95	0.84
My Thuan	-15.0	-18.3	17.6	19.1	2.3	4.6	2.3	3.6	0.90	0.74
Flood season 2018										
Can Tho	-2.9	-13.2	23.5	22.4	15.3	12.8	2.4	2.7	0.91	0.68
My Thuan	-3.8	-1.3	25.6	27.0	17.5	17.7	0.1	2.1	0.90	0.70

Suspended sediment content (SSC): Calibration and validation results at Can Tho and My Thuan stations are shown in Table 4, Figure 6. Calibration and validation results show that the error between simulation and actual measurement is very low. Seasonal changes in sediment and sand content are regular and consistent with seasonal flow changes. Thus, the simulation results are very good, showing that the model is highly reliable.

**Table 4.** Suspended sand and sediment content error and correlation values.

Station	Min		Max		Average		ME	MAE	MSE
	OBS	SIM	OBS	SIM	OBS	SIM			
Dry season 2018									
Can Tho	0.015	0.018	0.038	0.025	0.026	0.022	0.004	0.005	0.00003
My Thuan	0.018	0.030	0.046	0.040	0.033	0.033	0.000	0.006	0.00004
Flood season 2018									
Can Tho	0.062	0.094	0.122	0.182	0.093	0.131	0.038	0.042	0.000
My Thuan	0.093	0.175	0.320	0.279	0.218	0.217	0.001	0.039	0.002

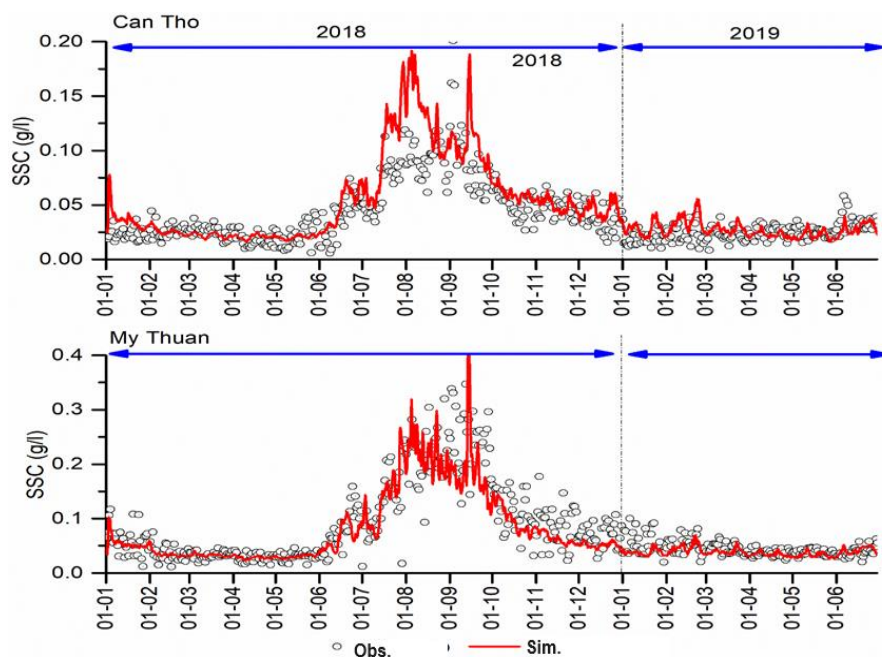


**Figure 6.** Illustration comparing SSC between simulation and actual measurements from 1/2018 - 6/2019.

The results of adjusting and testing the parameters of the open-source model TELEMAC 2D (Sisyphus - Mixed sediment) show the reliability of the parameters.

### 3.2. Simulation results

On the Tien River, at section ST1, the sediment flow passing through has a value of  $Q_{tb} = 1,327 \text{ kg/s}$ ,  $Q^+ = 9,872 \text{ kg/s}$ ,  $Q^- = -4,668 \text{ kg/s}$ . At the Cross section SH1 On the Hau River, the transport volume of sediment and sand is much smaller than that on the Tien River. the sediment flow passing through has a value of  $Q_{ave} = 232 \text{ kg/s}$ ,  $Q^+ = 5,605 \text{ kg/s}$ ,  $Q^- = -408 \text{ kg/s}$ .

On the Tien River at section (ST1), in the dry season, the maximum suspended sand transfer rate is from  $6.4 \times 10^{-3} \text{ m}^2/\text{s}$ , in flood season is  $7.5 \times 10^{-3} \text{ m}^2/\text{s}$ . Meanwhile, at section (SH1) on the Hau river, the sand transfer rate is smaller than that of the Tien river. In the dry season, the greatest value is  $3.5 \times 10^{-3} \text{ m}^2/\text{s}$ , in flood season is  $7.0 \times 10^{-3} \text{ m}^2/\text{s}$ .

After 3 years, the total deficit in sediment and sand compared to the beginning of the simulation period is  $-36.6 \times 10^6 \text{ m}^3$  at the section (ST1) and  $-2.7 \times 10^6 \text{ m}^3$  at the section (SH1).

Also from the simulation results, it shows that upstream of Tien River, the right bank tends to accumulate, the left bank tends to erode (there are many erosion locations from 0.25-0.5 m). For upstream of the Hau River, both banks tend to erosion and the level of erosion is also quite high, from 0.5-0.75 m, even up to 1.0 m in many places.

Thus, the upstream area is not able to balance sediment and always tends to lose sediment due to the process of transporting sediment from the upstream to the downstream area. Therefore, the upstream erosion trend is almost inevitable (Figures 7-8).

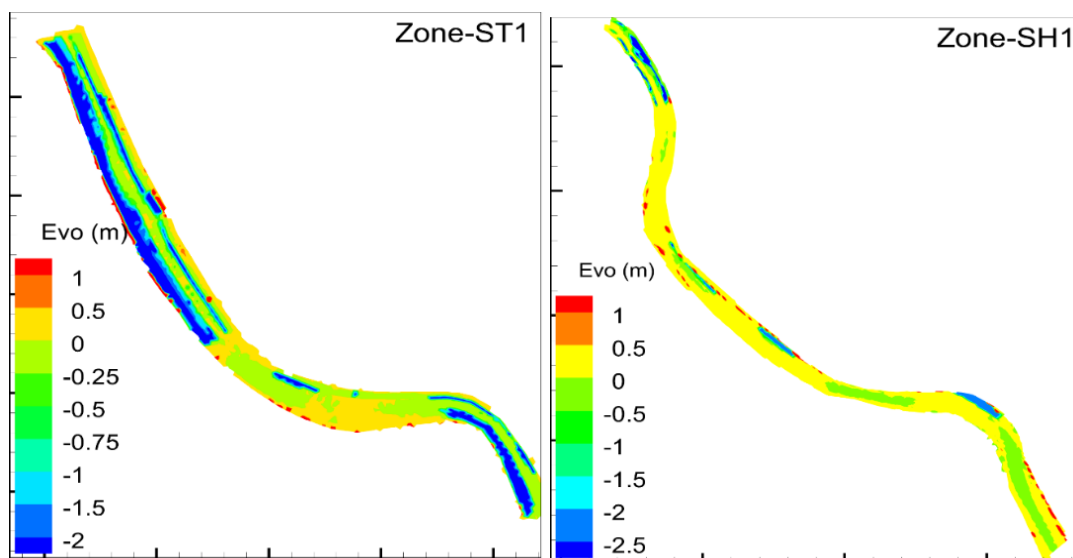


**Figure 7.** Illustration of bottom changes in the study areas.

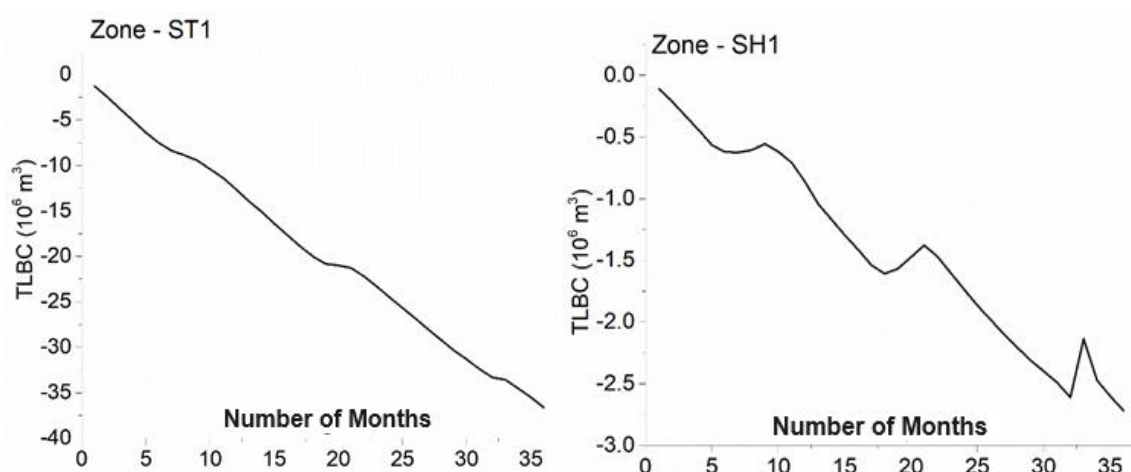


**Figure 8.** Illustrates the total of sediment accumulated at two study locations.

Due to the influence of seasonal regime, the sediment transport volume in the flood season is larger than in the dry season. During the dry season, sediment and sand are transported in both directions, but the amount of sediment and sand transported in the positive direction appears more often than in the opposite direction. During the flood season, sediment transport is mainly in the positive direction and this is even more evident when moving upstream.

#### 4. Conclusion

In this study, the TELAMAC 2D model (Sisyphé - Mixed sediment) was applied and built for the main river system in the Mekong Delta with a set of parameters that were calibrated and validated to achieve a good level with Nash index  $> 0.68$  (good), correlation coefficient  $R > 0.85$  (very good) and errors are all within allowable limits. This shows the reliability of the model as well as the stability of the model parameters.

Simulation results of the sediment transport process and assessment of the sediment balance for the two upstream sections of the Tien and Hau rivers (An Giang province) have shown that after 3 years, the total amount of sediment lost over Tien River section is  $-36.6 \times 10^6 \text{ m}^3$  at section (ST1) and  $-2.7 \times 10^6 \text{ m}^3$  at section (SH1). The erosion depth deepened by approximate 0.25-0.75 m (especially up to 1.0 m). Thus, the upstream area has an imbalance in sediment and sand and always tends to erode the riverbed, banks and beaches. These values are not fundamentally different from previous studies such as [26, 27].

With this result, this research makes a small contribution to the development of the TELEMAC open-source model with the world scientific community. Furthermore, the simulation results have partly shown the trend of riverbed erosion and aggradation in the upstream section of the Cuu Long River, in An Giang province.

The application and use of the open-source model have great potential, but further research and applications are needed to demonstrate its usefulness. This study is only the first step, and more research is needed in other basins.

Calibration and validation results do not yet cover all hydrological and hydraulic conditions and different mining activities, so the stability and reliability of the parameter set is limited.

The calculation results of the value of sediment deficiency are only at a relative level. Simulations for longer sections and the impact of human activities on the river are needed to show more realistic results.

**Authors contribution statement:** Research ideas, build scientific: C.T.V., N.T.G.; Research methodology: C.T.V., N.T.G.; Data collection and processing: N.H.T., L.V.N.; Modeling: L.N.A., N.H.T., N.C.T., L.V.N.; Write the manuscript and correct the article: C.T.V.; Editing and finishing: N.T.G., L.V.N.

**Acknowledgments:** This article is resulted from the An Giang provincial project “Research on building an early warning system for riverbank erosion due to extreme weather phenomena based on artificial intelligence”, code 373.2024.02. In addition, the study inherits data from the project of the Ministry of Natural Resources and Environment, code: TNMT.2018.02.13. The authors gratefully acknowledge this support.

**Competing interest statement:** The authors declare no conflict of interest.

#### References

1. Blazewski, R.; Pilarczyk, K.W.; Przedwojski, B. River training techniques: Fundamentals, Design and Applications, Rotterdam, 1995.
2. Massimo, R.; Casagli, N. Stability of streambanks formed in partially saturated soils and effects of negative pore water pressures: the Sieve River (Italy). *Geomorphology* **1999**, *26*(4), 253–277.

3. Massimo, R.; Darby, S.E. Modelling river-bank-erosion processes and mass failure mechanisms: progress towards fully coupled simulation. *Dev. Earth Surf. Processes* **2007**, *11*, 213–239.
4. Rosgen, D.L. A practical method of computing streambank erosion rate. Proceedings of the Seventh Federal Interagency Sedimentation Conference, 2001, 2, pp. 9–15.
5. Scott, S.H.; Jia, Y. Simulation of sediment transport and channel morphology change in large river systems US-China workshop on advanced computational modelling in hydroscience & engineering, September 19-21, Oxford, Mississippi, USA, 2002.
6. Winterbottom, S.J.; Gilvear, D.J. A GIS - based approach to mapping probabilities of river bank erosion: regulated river Tummel, Scotland. *Regul. Rivers: Res. Manage.* **2000**, *16*, 127–140.
7. Wu, W.M. CCHE2D Sediment Transport Model”, Technical Report No. NCCHE-TR-2001- 3, National Center for Computational Hydroscience and Engineering, The University of Mississippi, 2001.
8. Piégay, H.; Darby, S.E.; Mosselman, E.; Surian, N. A review of techniques available for delimiting the erodible river corridor: a sustainable approach to managing bank erosion. *River Res. Appl.* **2005**, *21*(7), 773–789.
9. Van, C.T.; Tuan, L.A.; Tuan, N.C.; Viet, C.T.; Anh, L.N. Application of two-dimensional hydrodynamic model (MIKE 21FM) to simulate the sediment regime on Hau river, piloted in Long Xuyen city - An Giang province. *Sci. Technol. Dev. J.: Sci. Earth Environ.* **2021**, *5*(SI2), 1–13.
10. Jason, B.; Cullen, P.; Dixon, G.; Pemberton, M. Monitoring and management of streambank erosion and natural revegetation on the lower Gordon River, Tasmanian Wilderness World Heritage Area, Australia. *Environ. Manage.* **1995**, *19*(2), 259–272.
11. Clark, L.A.; Wynn, T.M. Methods for determining streambank critical shear stress and soil erodibility: Implications for erosion rate predictions. *Trans. ASABE* **2007**, *50*(1), 95–106.
12. Couper, P.R.; Maddock, I.P. Subaerial river bank erosion processes and their interaction with other bank erosion mechanisms on the River Arrow, Warwickshire, UK. *Earth Surf. Processes Landforms* **2001**, *26*(6), 631–646.
13. Duró, G.; Crosato, A.; Kleinhans, M.G.; Uijttewaal, W.S.J. Bank erosion processes measured with UAV-SfM along complex banklines of a straight mid-sized river reach. *Earth Surf. Dynam.* **2018**, *6*, 933–953.
14. Bigham, K.A.; Moore, T.L.; Vogel, J.R.; Keane, T.D. Repeatability, sensitivity, and uncertainty analyses of the bancs model developed to predict annual streambank erosion rates. *J. Am. Water Resour. Assoc.* **2018**, *54*(2), 423–439.
15. Tien, P.H. et al. Forecasting the phenomenon of erosion and sedimentation on the coast and estuaries and prevention solutions. General report, State-level project, 2005.
16. Thanh, L.D. et al. Research and propose solutions to stabilize coastal estuaries in the Central region. General report, Key state-level projects. KC.08.07/06-10, 2010.

17. Cat, V.M. et al. Research solutions to flood drainage, prevent erosion and sedimentation at the Vu Gia - Thu Bon river estuary. General report, Key state-level projects, 2002-2003.
18. Hau, L.P. et al. Research on scientific and technological solutions for river correction works systems in key sections of the Northern and Southern Deltas. General report, Key state-level projects KC.08.14/06-10, 2010.
19. National Key Laboratory of River and Sea Dynamics, Vietnam Institute of Water Resources Sciences. Research on scientific and technological solutions to prevent sedimentation and stabilize flood drainage at Lai Giang river estuary. General report, Mard-level projects, 2008-2010.
20. Te, V.T. et al. Research and forecast of sedimentation and erosion of Dong Nai - Saigon river channel under the impact of anti-flooding and environmental improvement works system for Ho Chi Minh City. General report, Key state-level projects, Code: 21G/2009/HĐ-ĐHTL, 2012.
21. Hung, L.M. et al. Research the impact of sand mining activities on changes in the Mekong River channel (Tien River, Hau River) and propose reasonable management and exploitation planning solutions. General report, Key state-level projects, code: ĐTĐL 2010T/29, 2013.
22. Hung, L.M. et al. Research on forecasting Mekong River bank erosion. General report, Key state-level projects, 2001.
23. Hung, L.M. et al. Research on forecasting erosion and sedimentation of channel beds and propose prevention measures for the river system in the Mekong Delta. General report, Key state-level projects, KC-08.15, 2004.
24. San, D.C.; Hung, L.M. Law of changing width and depth ratio at stable cross-section along Tien River. *J. Agric. Rural Dev.* **2001**.
25. Hai, H.Q.; Trinh, V.T.M. Correlation of erosion - sedimentation in some areas of the Tien and Hau rivers. *J. Earth Sci.* **2011**, *31(1)*, 37–44.
26. Kim, T.T. et al. Modifying BEHI (bank erosion hazard index) to map and assess the levels of potential riverbank erosion of highly human impacted rivers: a case study for Vietnamese Mekong river system. *Environ. Earth Sci.* **2023**, *82*, 554. <https://doi.org/10.1007/s12665-023-11249-8>.
27. Hoang, T.B.; Duong, N.B.; Phong, N.C. Sand and sediment transport regime in the Mekong Delta in the upstream development scenario. *J. Irrig. Sci. Technol.* **2019**, *57*, 47–57.
28. Son, N.T.; Duc, N.A.; et al. Research to determine the cause of riverbank erosion and propose technology to warn and predict the level of riverbank erosion in some serious landslide areas in the Mekong Delta, Code: TNMT.2018.03.13, 2021.
29. Van, C.T.; Son, N.T.; Tuan, N.C. Research and experimental application of empirical formulas to calculate riverbank erosion in Tien river in Mekong Delta. *J. Environ. Sci. Eng. A* **2021**, *10*, 116–123.
30. Khanh, N.T.; Tuan, N.H.; Nu, H.T.T.; Van, C.T. Application of 2D hydro-dynamic model to simulate the suspended sediment on the Tien river, Cao Lanh district, Dong Thap province. *J. Hydro-Meteorol.* **2023**, *16*, 77–88.

31. Khoi, D.N.; Dang, T.D.; Pham, L.T.H.; Loi, P.T.; Thuy, N.T.D.; Phung, N.K.; Bay, N.T. Morphological change assessment from intertidal to river dominated zones using multiple-satellite imagery: a case study of the Vietnamese Mekong Delta. *Reg. Stud. Mar. Sci.* **2020**, *34*, 101087.
32. Institute of Computational Science and Technology. Building a riverbank erosion prediction model based on high-performance computing technology using GPUs combined with implementation based on empirical models and applications for some river sections of the Mekong Delta. General report, Key state-level projects, code: NĐT.28.KR.17, 2021.
33. Tanh, N.T.N. et al. Apply TELEMAC3d to simulate flow and sediment transport at the confluence area of Hau river and Vam Nao river (landslide area of My Hoi Dong commune). General report, An Giang province level projects, 2021.
34. Binh, D.V. et al. A novel method for river bank detection from Landsat satellite data: A case study in the Vietnamese Mekong Delta. *Remote Sens.* **2020**, *12(20)*, 3298.
35. Moser, D.K.; Zenz, G. 2D numerical simulations of embankment dam failure due to overtopping. Proceedings of the 21<sup>st</sup> TELEMAC-MASCARET User Conference, 15-17<sup>th</sup> October 2014 Grenoble - France. ARTELIA Eau & Environment, 2014, pp. 51–57.
36. Villaret, J.M.; Kopmann, H.R.; Merkel, U.; Davies, A.G. Morphodynamic modeling using the TELEMAC finite-element system. *Comput. Geosci.* **2013**, *53*, 105–113.
37. Goll. Direct Simulations of Bed Forms of the River Elbe, Germany. Proceedings of the 21<sup>st</sup> TELEMAC-MASCARET User Conference, 15-17<sup>th</sup> October 2014 Grenoble - France. ARTELIA Eau & Environment, 2014, pp. 153–157.
38. MRC. MRC Sediment monitoring. Proceeding of the 2<sup>nd</sup> Mekong Roundtable, 22 April 2024, Phnom Penh, Cambodia, 2024.



*Research Article*

# **Stress distribution under coal pillars in the case of multi-seam mining: A case study at Thong Nhat Coal Mine, Vietnam**

**Phuc Quang Le<sup>1,2</sup>, Ha Thu Thi Le<sup>1,4</sup>, Long Quoc Nguyen<sup>1,3\*</sup>**

<sup>1</sup> Hanoi University of Mining and Geology, Hanoi, Vietnam; lequangphuc@humg.edu.vn; lethithuha@humg.edu.vn; nguyenquoclong@humg.edu.vn

<sup>2</sup> Research Group: Sustainable Development of Mining Science, Technology and Environment (SDM), Hanoi University of Mining and Geology, Hanoi, Vietnam; lequangphuc@humg.edu.vn

<sup>3</sup> Innovations for Sustainable and Responsible Mining, Hanoi University of Mining and Geology, Hanoi, Vietnam; nguyenquoclong@humg.edu.vn

<sup>4</sup> Geomatics in Earth Sciences Research Group, Hanoi University of Mining and Geology, Hanoi, Vietnam; lethithuha@humg.edu.vn

\*Corresponding author: nguyenquoclong@humg.edu.vn; Tel.: +84–916196336

Received: 27 March 2024; Accepted: 9 May 2024; Published: 25 September 2024

**Abstract:** The presence of an overlying coal pillar (OCP) strongly influences the stress distribution and deformation of the surrounding rock of the roadway and working face. In this paper, the stress distribution characteristics under the coal pillar are analyzed through numerical simulation using the FLAC3D program. Multi-coal seam mining conditions at Thong Nhat coal mine were selected as the technical foundation. Research results show that the presence of coal pillars acts as a bridge to transfer loads from the roof rock strata to the floor, and therefore it forms a high-stress concentration zone with an oval shape under the coal pillar. Caused by stress superposition, abutment stress distribution rules are affected by the distance from the roadway or working face to the OCP. In the concentrated stress zone of the OCP, the abutment pressure at the roof and floor of the roadway increases by 2 times and puts the road into a dangerous deformation condition. Meanwhile, when the working face approaches the OCP, the front abutment pressure value increases 1.3 times, and the range of the high-stress zone increases 2 times. Thus, the presence of OCP has changed the stress distribution law in the direction of increasing the value and distribution range of the maximum stress area, and it affects the roadway and working face of the coal seam below. The research results of this article will be an important document as a basis for researching technical solutions to meet the requirements for safe mining in underground coal mines.

**Keywords:** Coal pillar; Stress distribution; Abutment pressure; Multi-seam mining; Roadway; Longwall face.

---

## **1. Introduction**

In the realm of coal mining, particularly in multi-seam operations, the stress distribution beneath coal pillars is a critical factor influencing mine stability. The coal pillars, acting as primary support structures, bear the overburden pressure and redistribute stresses within the seam. In multi-seam mining, the interaction of stresses between seams adds complexity to this distribution. The stress concentration around the pillars can lead to pillar failure and ground control problems, posing significant safety risks. Therefore, understanding and accurately predicting the stress distribution under these conditions is crucial for safe and efficient mining operations.

In underground coal mining, the success of a mining enterprise is determined by many factors. One of them is the stability of roadways and longwall faces. This task becomes even more complicated when multi-coal seams mining. In the mining plan of underground coal mines in Vietnam, the mining order is carried out sequentially from the upper seam to the lower seam. In this case, the longwall face or roadway in the lower coal seam is placed under the gob or coal pillar of the upper coal seam. Production practice and theory have proven that the coal pillar of the upper coal seam will become a place where stress from the roof rock strata is concentrated, and this can increase abutment pressure to a seriously threatening level to the safe production of coal mines [1, 2]. Studies on the influence and control of OCP on roadway stability and the exploitation of the lower coal seam have been the focus of many scientific works. Liu et al. combined theoretical analysis with field testing, allowing them to detect abnormal magnitudes of abutment pressure when mining coal seams under the OCP [3]. The study [4] used numerical simulation and theoretical analysis to obtain the asymmetric stress distribution law under the coal pillar. With this result, they research and design the optimal location of the roadway to increase roadway control and labor safety. The study [5] studied the stress distribution law in the upper coal pillar according to soil mechanics principles and numerical analysis. They discovered an abnormal increase in the value stress on the roof of the roadway and longwall face when their position is under the stress concentration zone of OCP. Xia, Huang et al. focused on studying the influence of the OCP on the cracking of hard strata, and the abutment pressure under the coal pillar in case of dual effect when multi-seam mining [6–8].

In addition, there are some other notable projects such as Investigation of strong strata behaviors in the close-distance multiseam coal pillar mining [9], this study delves into the behaviors of strong strata in the context of close-distance multiseam coal pillar mining, providing valuable insights into the dynamics of such environments. Coupling control on pillar stress concentration and surface cracks in shallow multi-seam mining [10], it focuses on the interplay between pillar stress concentration and surface cracks in shallow multi-seam mining, offering a comprehensive understanding of the factors influencing these phenomena when applying technical solutions of coal mining and gas extraction without coal pillar in multi-seam with low permeability [11]. These studies investigate the failure mechanisms of gob-side roadways under the pressure of overlying coal pillars in multiseam mining, as well as the design considerations for multi-seam mines intended for coal extraction [12, 13]. Implementing a rational coal pillar design in multi-seam mining, and achieving the coupling control of underground concentrated stress and surface fractures [14]. In order to boost underground coal production in India, supports are essential. Longwall mining, which involves an array of chain pillars, is used in multi-seam longwall mining panels in India's deepest coal mine. This method helps in maintaining the stability of the mine and ensures the safety of the miners while maximizing the extraction of coal [15]. In the research [16], the authors first obtained the rock by using a coal mine with multi-seam mining in Datong as a case study. Then, based on the geological conditions, we proceeded with the physical analysis. This approach allows us to understand the complexities of multi-seam mining and provides valuable insights for improving mining efficiency and safety. The next steps of the study would likely involve further analysis and testing based on these physical conditions. The extensive and interconnected movements of multi-seam goaf have exacerbated issues when the longwall is mined under the edge of mining panels and remnant pillars within the mine. This situation presents significant challenges in maintaining the stability of the mine and ensuring the safety of the miners. It underscores the need for careful planning and robust support structures in multi-seam mining operations. Further research and development are required to mitigate these issues and enhance the efficiency and safety of longwall mining under such complex conditions [17]. The study [18] aims to understand the dynamics of coal pillar positions and their impact on the stability and safety of mining operations. It provides

valuable insights into the optimal positioning of coal pillars to prevent potential hazards and improve the efficiency of multi-seam mining operations. Further details would likely involve the specific methodologies used and the findings from the Research.

The studies related to the coal pillars mentioned above focus on the instability of coal pillars and the law of stress propagation through the coal pillar to the floor. However, in small slope angles areas of the coal seam, OCP may be perpendicular to the longwall face and the lower roadway. In this case, studies on the stress distribution characteristics in the OCP that affect the roadway and longwall face under are not much. The resonance effect of stress in the OCP and the abutment stress in front of the longwall face is very complicated. To clarify this issue, the article takes the mining conditions at coal seams 4C and 3C in the Thong Nhat coal mine as the research object.

## 2. Materials and Methods

The technical foundation for this study is mining conditions at 4C and 3C coal seams in the Thong Nhat coal mine, Quang Ninh region, Vietnam. Coal seam 3C is located under and the distance between the two seams is 7.5 m. Coal seam 4C was mined first, in which a 25 m-wide coal pillar was left in the gob. The roadway and longwall faces at coal seam 3C are perpendicular to the coal pillar of seam 4C. The relationship of the coal pillar at seam 4C with the roadway and longwall face at seam 3C is presented in Figure 1. Coal seams 4C and 3C are in depth 313 m and 320.5 m, respectively. They have a slope angle of 70 and a thickness of 3m and 4.5 m, respectively. The surrounding rocks are respectively layers of claystone, siltstone, and sandstone. See Figure 2 for map of the research area and stratigraphic columns in the study area. For the physical and mechanical properties of surrounding rocks, see Table 1.

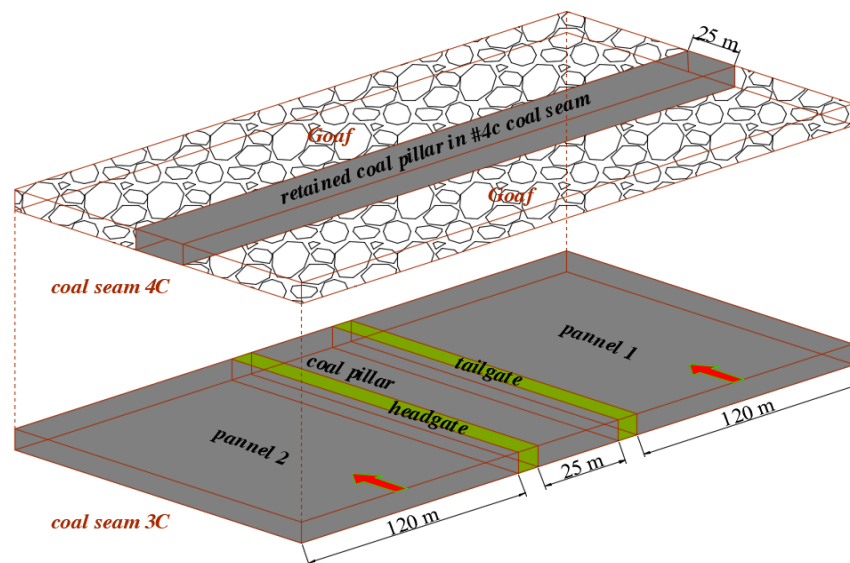


**Figure 1.** Three-dimensional diagram of the relative position of the OCP with roadways and longwall faces.

**Table 1.** Properties of rocks and coal in the study area.

Type rock	Tensile strength (MPa)	Bulk modulus (GPa)	Shear modulus (GPa)	Poisson's ratio	Cohesion (MPa)	Friction angle (deg.)	Density (kg/m <sup>3</sup> )
Fine-sandstone	1.75	8.120	3.642	0.30	3.15	38	2840
Sandstone	1.63	7.451	3.240	0.31	3.21	34	2775
Mudstone	0.98	2.342	0.950	0.32	2.16	30	2556
Siltstone	1.25	1.826	0.609	0.34	1.83	26	2250
Coal	0.5	0.755	0.486	0.26	1.45	19	1460

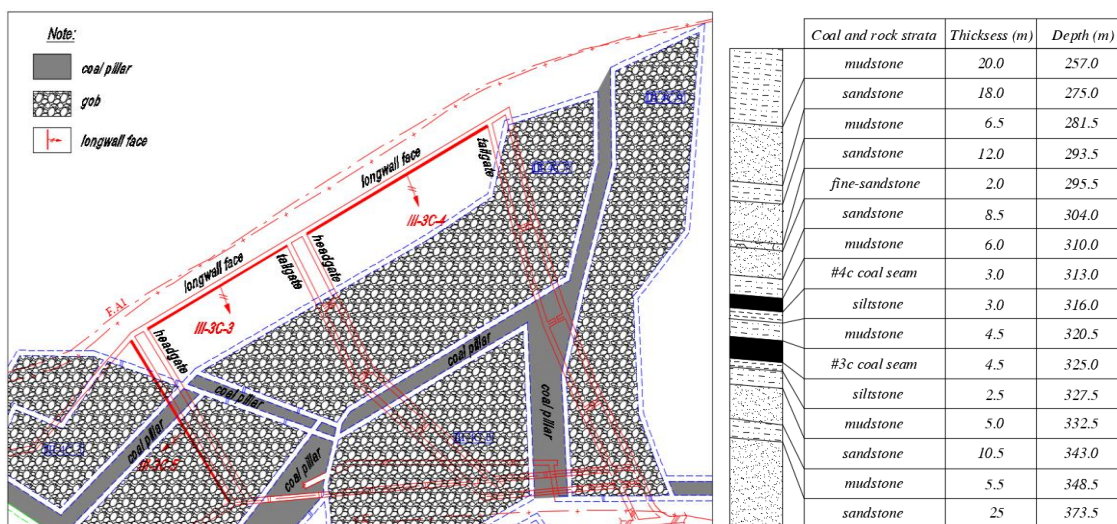


Figure 2. Map of the research area, stratigraphic and petrographic column.

The numerical modeling research method with the Flac3D program is used in this study: FLAC3D (Fast Lagrangian Analysis of Continua in 3 Dimensions) is numerical modeling software for geotechnical analyses of soil, rock, groundwater, constructs, and ground support. FLAC3D utilizes an explicit finite volume formulation that captures the complex behaviors of models that consist of several stages, show large displacements and strains, exhibit non-linear material behavior, or are unstable (including cases of yield/failure over large areas, or total collapse). This is a finite element model with construction materials such as coal and stone considered elastic materials that meet the Mohr-Coulomb durability criteria [19]. The model dimensions are 350 m long, 265 m wide, and 140 m high. The side boundaries of the model have been fixed to displacements in the horizontal direction, and the bottom boundary has been fixed to displacements in the horizontal and vertical directions. The top boundary of the model is not constrained in displacement. Natural load is applied to the upper boundary of the model with a vertical stress of 6.5 MPa. The upper specific gravity is assumed to be 0.025 MN/m<sup>3</sup>, and gravity is also applied. The stratigraphic and rock mechanical parameters used in the model are similar to the study area conditions at seams 4C and 3C of the Thong Nhat coal mine (Table 1). The model structure diagram is presented in Figure 3.

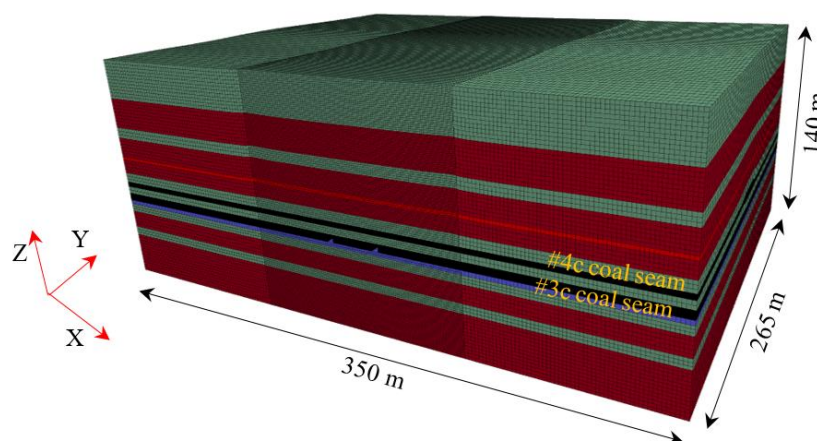
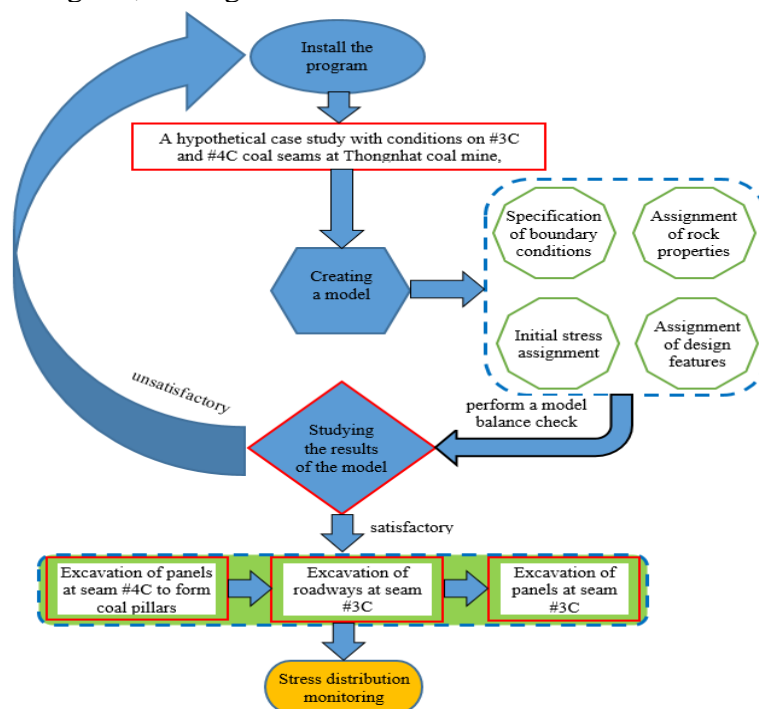


Figure 3. Structure diagram of the simulation model.

In this model, the 4C coal seam is exploited first. During the exploitation of seam 4C, coal pillars with a width of 25 m are formed in the gob. Next, two roadways were excavated in the 3C coal seam in a direction perpendicular to the coal pillar. Finally, panels on the 3C coal seam are mined in a direction perpendicular to the coal pillar. The distance between coal

seams and their distribution depth is similar to Figure 2. During model implementation, stress data is extracted at the location of coal pillars, roadways, and longwall faces. Model's research structure diagram, see Figure 4.



**Figure 4.** Research structure diagram.

### 3. Results and Discussions

#### 3.1. Stress distribution under the coal pillar

When there is no OCP, crack development occurs under the gob of the 4C seam to a certain extent. Therefore, when mining coal seam 3C, the integrity of the coal seam and its roof is broken, it causes a certain pressure drop during the mining of the coal seam. In the presence of OCP, stress concentrations are formed in the coal pillar [20]. The coal pillar then acts as a bridge to transfer stress to the coal seam 3C (Figure 5).

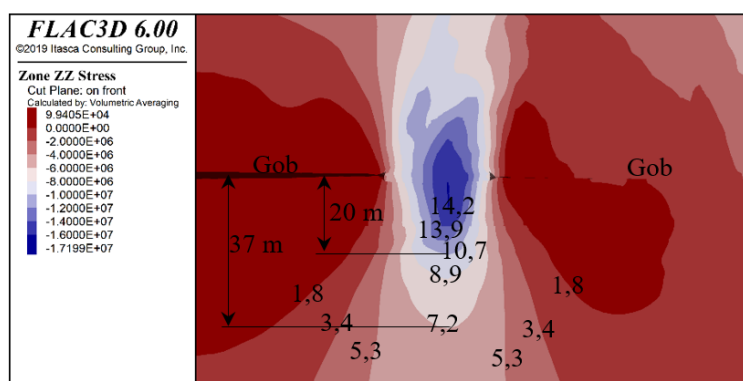


**Figure 5.** Vertical stress distribution under the coal pillar.

Figure 5 shows that the coal pillar completely bears the load of the roof rock strata. Therefore, there is quite a high stress concentration in the coal pillar. The stress at the center of the coal pillar is 17.2 Mpa and then gradually decreases to the two sides. Under the gob area, the vertical stress is quite small, only 1.8-3.4 Mpa. However, near the coal pillar, stress increases rapidly. The high-stress zones under the coal pillars are oval and appear to extend vertically. At a distance 37 m under OCP, the vertical stress is 7.2 Mpa, nearly equal to the

initial static stress. And then, the vertical stress increases rapidly when approaching the coal pillar. The vertical stress is 10.7 Mpa at a distance of 20 m under the coal pillar. This value is respectively 15.5 Mpa and 16.3 Mpa when distances 10 m and 5 m, correspond.

Production practice shows that high stress in the surrounding rock is an unfavorable working environment for underground coal mining. In this condition, the risk of rock burs can occur and threaten labor safety. Especially when mining coal seams at close distances, the status of roadway deformation and support destruction often at the Thong Nhat coal mine. Therefore, it is necessary to eliminate OCP when multi-seam mining.

### 3.2. Stress distribution when the roadway is excavated under the coal pillar

Corresponding to the research conditions at seams 4C and 3C at the Thong Nhat coal mine (the distance between the two seams is 7.5 m), the stress distribution when excavating the roadway under the coal pillar is shown in Figure 6.

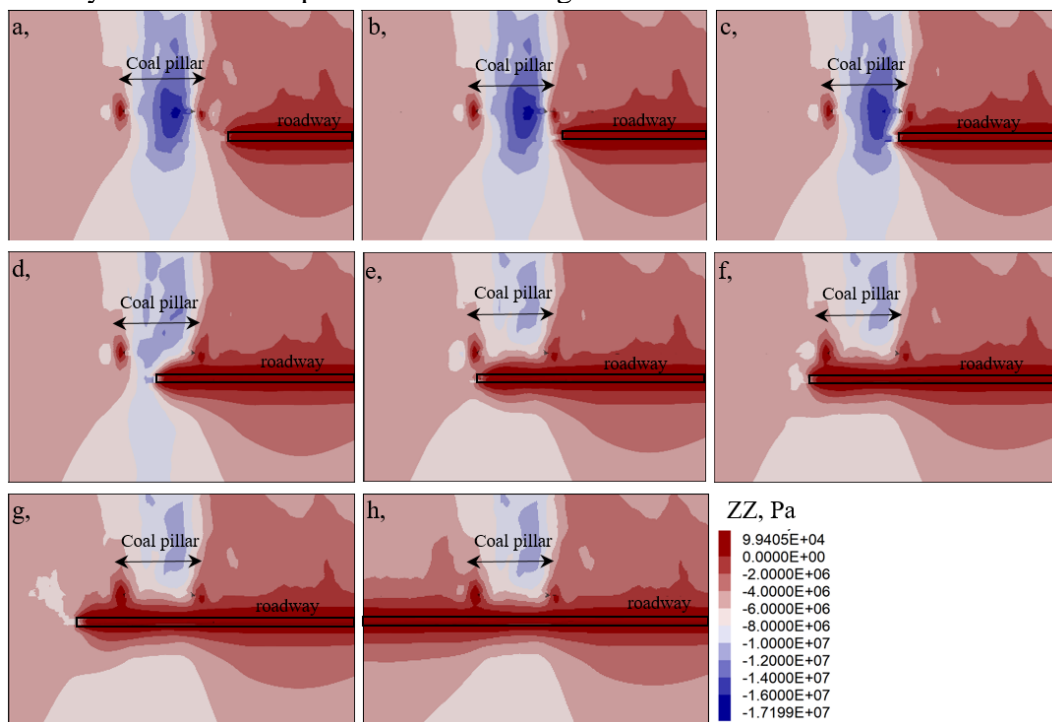


**Figure 6.** The stress distribution under the coal pillar corresponds to the distance to the working face of the roadway: (a) 20 m from the coal pillar; (b) 10 m from the coal pillar; (c) meet the coal pillar; (d) in the middle of the coal pillar; (e) when starting to pass the coal pillar; (f) pass 10 m coal pillar; (g) pass 20m coal pillar; (h) completely surpasses the coal pillar.

Figure 6 shows a significant change in stress distribution when excavating the roadway under the coal pillar. When the roadway is far from the coal pillar, the stress distribution in the surrounding rock of the roadway follows the normal law. However, when the roadway approaches the coal pillar, the superposition of stress from the coal pillar and the abutment pressure in front of the working face of the roadway increases. Specifically, when the distance between the coal pillar and the working face of the roadway is 20 m, the front abutment pressure is 6.2 Mpa and increases to 9.6 Mpa at a distance of 10 m. When the roadway begins to enter the area under the coal pillar, the superposition of stress from the coal pillar causes the maximum stress value to increase to 13.1 Mpa. When the roadway was excavated to the middle of the coal pillar, the maximum stress value began to decrease to 10.6 Mpa. However, almost all the stress from the coal pillar is transmitted to the roof of the roadway, the stress value reaches 10.5 Mpa. This can be explained by the failure of the surrounding rock mass the effect of eliminating the stress concentration in front of the roadway, and the roadway under the coal pillar would bear the entire load loaded of OCP. Therefore, there is a high risk

of rock bursts on the roof of the roadway. As the roadway begins to pass the coal pillar, the abutment stress in front of the roadway decreases to 8.2 Mpa and is stable at 6.0 Mpa. The stress area from the coal pillar loading on the roadway remains unchanged compared to the previous case.

Figures 6e-6g, 6h show a large stress area from the coal pillar with a stress value of 10-10.5 Mpa acting on the roof of the roadway. At the same time, a high-stress zone with a stress value of about 8.3 Mpa is also formed on the floor of the roadway. These stress values are almost 2 times higher than in other areas. At this location, the roadway is pressed from both roof and floor, causing the phenomenon of falling roof rocks and floor heave. This explained the deformation of roadways that frequently occurred when excavating them under coal pillars. According to statistics at the Thong Nhat coal mine, the frequency of repairing these roadways is every 4-5 months. Frequent roadway repairs have hurt production efficiency and labor safety.

### 3.3. Stress distribution when mining panels under coal pillars

The stress distribution in front of the longwall face when performing panel mining under the influence of coal pillars is shown in Figure 7.

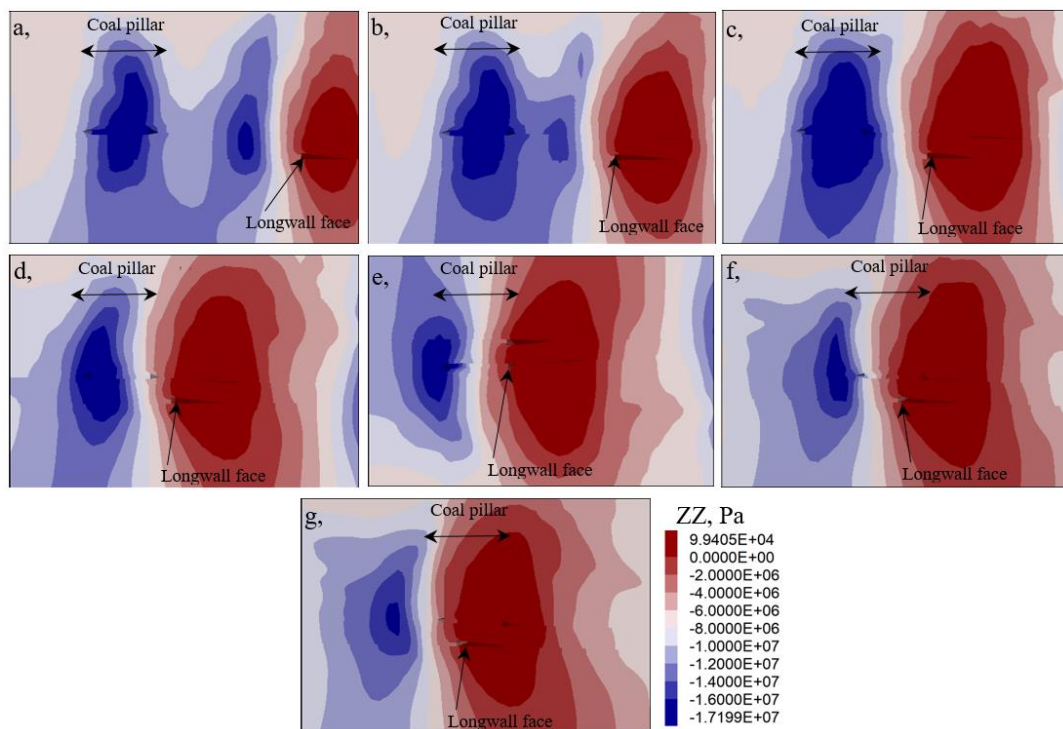


**Figure 7.** Stress distribution in front of the longwall face under the influence of the OCP, when the distance between the longwall face and the coal pillar: (a) 70 m, (b) 50 m, (c) 30 m, (d) 10 m, (e) approaching OCP, (f) in the middle of OCP, (g) passing the OCP.

As seen in Figure 7, the stress distribution in front of the working face differs greatly in the cases of the absence or presence of the OCP. When the distance between the longwall face, and the OCP is 70 m, the abutment stress in front of the longwall face increases, then decreases and increases again due to the stress concentration under the OCP. In Figure 7a, the abutment stress is formed in the form of two peaks in front of the longwall face. A maximum stress of 15.3 MPa was observed at a distance of 15 m from the longwall face, while the maximum stress under the coal pillar was 17.2 Mpa. As the longwall face advances, the abutment stress peak in front of the longwall face decreases to 13.8 MPa at a distance of 50m. The main reason is that the gob area next to the coal pillar of the upper seam has been unloaded and reduced the stress concentration, so the stress of the surrounding rock is

significantly reduced. As the longwall face continues to excavate forward and at a distance of 30 m from the coal pillar, the abutment stress in front of the longwall face only remains a single peak under the coal pillar. The maximum value of abutment stress does not change much, however, under the interference of the stress in front of the longwall face and the stress under the pillar, the high-stress area is expanded 1.5 times compared to the coal pillar. It can be seen that OCP strongly impacts the longwall face within a range of less than 50 m and a rapid increase in stress in the coal seam. When the longwall face is at a distance of 10 m and approaches the coal pillar, the front abutment stress area gradually narrows and shifts to the opposite side. The maximum stress value remains at 17.2 Mpa. When the longwall face is in the middle of the OCP, the abutment stress peak begins to move away from the coal pillar, and the maximum stress value is 16.3 Mpa. When the longwall face passes the OCP, the abutment stress in front of the longwall face returns to normal with a maximum stress value of 13.3 Mpa at a distance of 15m and then stabilizes at 12.6 Mpa.

Figure 7 implies in the absence of OCP, the maximum stress in front of the longwall face is lower. In the presence of OCP, the maximum stress value is higher and the distribution range is wider. As the longwall face approaches the OCP, the abutment stress increases sharply and maintains a high value. The area affected by stress concentration in OCP is larger and stable control of the longwall face becomes more difficult.

#### 4. Conclusion

- Simulation results show that the appearance of OCP will form an oval-shaped enhanced stress concentration zone. The coal pillar acts as a bridge to transmit the entire load of the roof rock strata to the coal seam below, significantly affecting the stress distribution when excavating the roadway and mining panels. In the presence of OCP, the maximum stress will be higher and spread across the width of the OCP. Residual stress from the coal pillar will compress the roadway vertically from the roof and floor. Therefore, if not well supported and corresponding technical solutions are applied, the roadway will deform and be destroyed.

- The presence of OCP affects the stress distribution in front of the longwall face. When the longwall face in the lower coal seam is far from the coal pillar, the stress distribution in front of the longwall face is relatively stable and follows the law of abutment pressure. When the longwall face approaches the OCP, the superposition of the coal pillar's stress and the abutment stress causes the maximum value of the stress to increase significantly and expand the influence area by 1.5 times. With this condition, the scope of overburden collapse in the roof and working face expands and causes rockburst safety risks.

- The result of the research found the law of stress distribution under the coal pillar. This is an important factor in finding solutions to ensure safety when excavating roadways and mining longwall faces of the adjacent seam below. The main gap in the research is that the model can only simulate a specific geological case. The variation in thickness and slope angle of the rock layers has not yet been considered. However, this is also the basic foundation for developing subsequent research projects according to different parameters of coal seam thickness, distance between coal seams, and other parameters. The research results will be the basis for mine managers to develop plans and operate mines safely.

**Author contribution statement:** Generating the research idea; statement of the research problem; analysis of research results and data preparation; wrote the draft manuscript: P.Q.L., H.T.T.L.; Analyzed and interpreted the data, wrote the draft manuscript: L.Q.N.

**Acknowledgements:** This research was funded by the Viet Nam Ministry of Education and Training, grant No: B2024–MDA–03 (Research, evaluate influencing factors, and propose technical solutions to ensure roadway stability in the case of multi-coal seam mining, with gentle slopes in the Quang Ninh region).

**Competing interest statement:** The authors declare no conflict of interest.



## References

1. Zhang, Z.; Deng, M.; Bai, J.; Yan, S.; Yu, X. Stability control of gob-side entry retained under the gob with close distance coal seams. *Int. J. Min. Sci. Technol.* **2021**, *31*(2), 321–332.
2. Ju, J.F.; Hu, G.L. Influence of leading instability in the upper dip coal pillar boundary to the strong strata behaviors during the working face out of the pillar. *J. China Coal Society.* **2012**, *37*(7), 1080–1087.
3. Liu, C.Y.; Yang, J.X.; Liu, J.R. Mechanism of strong pressure reveal under the influence of mining dual system of coal pillar in Datong mining area. *J. China Coal Society.* **2014**, *39*(1), 40–46.
4. Lei, X.U.; Hailiang, Z.; Dongkun, G.; Bo, L.I. Principal stress difference evolution in floor under pillar and roadway layout. *J. Min. Saf. Eng.* **2015**, *32*(3), 478.
5. He, Y.; Huang, Q.; Ma, L.; Wang, Q.; Fan, D. Research on roof weighting mechanism of coal pillar mining in shallow buried closely spaced multi-seams. 2023.
6. Xia, B.; Jia, J.; Yu, B.; Zhang, X.; Li, X. Coupling effects of coal pillars of thick coal seams in large-space stopes and hard stratum on mine pressure. *Int. J. Min. Sci. Technol.* **2017**, *27*(6), 965–972.
7. Huang, Q.; Du, J.; Chen, J.; He, Y. Coupling control on pillar stress concentration and surface cracks in shallow multi-seam mining. *Int. J. Min. Sci. Technol.* **2021**, *31*(1), 95–101.
8. Cheng, W.; Nong, Z.; Guichen, L.; Nianchao, Z. De-stressed mining of multi-seams: Surrounding rock control during the mining of a roadway in the overlying protected seam. *Min. Sci. Technol.* **2011**, *21*(2), 159–164.
9. Mu, H.; Bao, Y.; Song, D.; Su, D. Investigation of strong strata behaviors in the close-distance multiseam coal pillar mining. *Shock Vib.* **2021**, 1–14.
10. Huang, Q.; Du, J.; Chen, J.; He, Y. Coupling control on pillar stress concentration and surface cracks in shallow multi-seam mining. *Int. J. Min. Sci. Technol.* **2021**, *31*(1), 95–101.
11. Yuan, L. Technique of coal mining and gas extraction without coal pillar in multi-seam with low permeability. *J. Coal Sci. Eng.* **2009**, *15*(2), 120–128.
12. Mu, H.; Wang, A.; Song, D.; Su, D.; Li, D. Failure mechanism of gob-side roadway under overlying coal pillar multiseam mining. *Shock Vib.* **2021**, 1–13.
13. Tati, B. Multi-seam coal mining. *J. South. Afr. Inst. Min. Metall.* **2011**, *111*(4), 231–242.
14. Huang, Q.; Cao, J. Research on coal pillar malposition distance based on coupling control of three-field in shallow buried closely spaced multi-seam mining, China. *Energies* **2019**, *12*(3), 462.
15. Ghosh, N.; Agrawal, H.; Singh, S.K.; Banerjee, G. Optimum chain pillar design at the deepest multi-seam longwall workings in India. *Min. Metall. Explor.* **2020**, *37*, 651–664.
16. Tian, C.; Yang, X.; Sun, H.; Liu, Y.; Hu, Q. Experimental study on the overburden movement and stress evolution in multi-seam mining with residual pillars. *Energy Sci. Eng.* **2019**, *7*(6), 3095–3110.
17. Zhu, Z.; et al. Overburden movement characteristics of top-coal caving mining in multi-seam areas. *Q. J. Eng. Geol. Hydrogeol.* **2018**, *51*(2), 276–286.
18. He, Y.; et al. Research on roof weighting mechanism of coal pillar mining in shallow buried closely spaced multi-seams, 2023.
19. ITASCA. Fast Lagrangian Analysis of Continua User's Guide; Itasca Consulting Group Inc.: Minneapolis, MN55401, USA. 2019. <https://www.itascacg.com/search>.
20. Phuc, L.Q. Cause and solution to roadway deformation in Vietnam underground coal mines. *Inżynieria Mineralna* **2021**, *2*(1), 381–390.

*Research Article*

# Multi-sensor points cloud data fusion for 3D building models: A case study in Halong City, Vietnam

Ha Thu Thi Le<sup>1,2\*</sup>

<sup>1</sup> Hanoi University of Mining and Geology, Hanoi, Vietnam; lethithuha@humg.edu.vn

<sup>2</sup> Geomatics in Earth Sciences Research Group, Hanoi University of Mining and Geology, Hanoi, Vietnam; lethithuha@humg.edu.vn

\*Corresponding author: lethithuha@humg.edu.vn; Tel.: +84-983115967

Received: 28 April 2024; Accepted: 04 June 2024; Published: 25 September 2024

**Abstract:** Three-dimensional building models play a crucial role in urban planning, emergency response, disaster management, and decision-making. Multi-sensor data fusion has recently attracted significant interest in the Geomatics research community. This approach addresses the limitations of individual sensors, allowing for the creation of comprehensive 3D models of structures and improving object classification. This study focuses on developing approaches that combine various geospatial technologies to produce a complete 3D model of common urban architectures, including high building, neighboring villa, and individual home. This research used flexibly employ UAV aerial imagery, ground photography, and terrestrial LiDAR scanning to collect the necessary information for constructing complete 3D models of each characteristic urban structure. Different point cloud datasets will be processed, merged, and used to generate the completely 3D models. The experimental results have produced complete 3D models with accuracy achieved with  $\Delta x$ ;  $m\Delta y$ ;  $m\Delta z$  all below 10 cm for the experimental buildings. With the accuracy of the 3D models, it is entirely possible to achieve accuracy in horizontal plane and height for the 1:500 scale terrain map.

**Keywords:** 3D building models; Multi-sensor points data fusion; Halong city; Vietnam.

---

## 1. Introduction

Buildings are some of the most significant features in urban environments and are modeled for a range of uses, such as simulating air pollution, estimating energy use, detecting urban heat islands, and many other applications [1]. Three-dimensional (3D) building models play a crucial role in urban planning, emergency response, disaster management, and decision-making processes. 3D buildings aim to represent the geometry and appearance of reality, enabling us to see the city as it currently exists, how it appeared in the past, and how it is likely to appear in the future. Efficiently creating these models enhances digital library content concerning buildings and infrastructure and provides managers with essential tools for visualization and decision-making [2]. The concept of a three-dimensional (3D) model or representation is frequently linked to the future due to its status as an increasingly utilized and evolving technology [3]. Advanced technologies in recent years have enabled the creation of accurate and intricate 3D models for depicting buildings as they were constructed [4]. There are some different data acquisition techniques used to create the 3D object modeling: lidar, radar, camera (photogrammetry), and total stations [2, 5–7]. Images captured by drones are utilized to attain exceptionally detailed 3D models, enabling the reconstruction of both the geometry and texture of the examined objects [1, 8–10]. Drones are now extensively employed for data gathering and 3D reconstruction objectives.

The quality of the resulting 3D data significantly relies on factors such as the specifications of the sensors utilized, the setup of the photogrammetric network, and the outcomes of image orientation. The growing adoption of UAVs in surveying tasks is largely attributed to their lightweight design and affordability. UAVs, which are unmanned, reusable motorized devices, generally hover vertically at low altitudes just a few meters above objects [1, 11]. Moreover, through the implementation of UAV photogrammetry, UAVs can swiftly gather data and offer high-resolution aerial photographs. Subsequently, the gathered data can be employed to recreate the terrain of a model representing the research area, resulting in highly detailed 3D mapping and modeling. This process considers factors such as image overlap, scale adjustments, and flight altitude [12]. Scanning surveys offer an advantage in terms of time efficiency, as they are automated and capable of capturing numerous details in a single scan, minimizing the risk of overlooking any details. In the current development trend, 3D Laser Scanning technology (TLS - Terrestrial Laser Scanner) is becoming known and applied in surveying and inspecting structures, gradually replacing the aforementioned devices due to its higher accuracy than UAVs, as the scanner is fixed on the ground. The 3D Laser Scanning equipment has the capability to collect numerous point clouds in space, which capture the detailed surface shapes of objects. Each point in these clouds contains coordinate information (XYZ) and color parameters. Besides, ground-based digital camera is another low-cost data acquisition technique, which is currently used in 3D modeling applications [13–18]. Unfortunately, however, digital cameras are restricted by line-of-sight limitations. Consequently, it can be observed that each data acquisition method has its own strengths and weaknesses. Hence, the fusion of data emerges as a critical concern for generating accurate 3D object models [19–21].

In Vietnam, the government has determined that developing smart cities is the best choice to support the current urbanization and economic growth process. Quang Ninh province and Ha Long city are making significant progress to align with the Government's strategy and priorities for smart city development in Vietnam. When constructing comprehensive 3D information models for urban areas, it's crucial to consider the distinctive features of coastal cities in Vietnam, considering the specific conditions present in each locality throughout the country. Previous domestic studies have shown that researching the construction of 3D models for some urban construction projects by integrating geospatial technologies remains limited. Moreover, the majority of recent studies only utilize a single type of geospatial technology to collect 3D information of individual construction objects [22, 23]. There have been few studies describing the process of integrating geospatial technologies to build high-precision 3D models for complex and characteristic structures such as coastal urban areas in Vietnam.

This research focuses on two main goals: (1) To propose a process for applying geospatial technology in collecting 3D spatial information for characteristic construction objects in coastal urban areas; (2) To develop high-precision 3D models for characteristic construction objects in Ha Long city, Quang Ninh province. Vietnam encounters a new challenge when it comes to processing data from diverse sensor sources. Currently, research predominantly concentrates on managing data from a solitary technology type, like UAV or aerial Lidar, terrestrial Lidar, or ground-based stereophotography. Managing data from a single sensor source is considerably simpler than handling data from multiple sensor sources with differing resolutions. Consequently, this persists as a challenge in developing thorough 3D models for particular construction projects in Vietnam.

## **2. Materials and Method**

### *2.1. Description of the study site*

The experimental area is located in Bai Chay ward and Hung Thang ward, Ha Long city, Quang Ninh province, Vietnam (Figure 1a), primarily encompassing the high-end coastal

urban area developed by BIM Group. The urban area consists of individual villas and adjacent villas. Additionally, it includes internal transportation systems, water supply and drainage systems, and public facilities serving the community. There are also several high-rise buildings along the main roads, serving as residences, hotels, or office headquarters for various organizations.



**Figure 1.** The study site.

Phat Linh Hotel Ha Long is a 5-star luxury hotel, located at A9, Lot 1, Ha Long Marine Boulevard, Ha Long city, Quang Ninh Province (Figure 1a). Phat Linh Hotel is a tall as being at least 120 m, continuously habitable building having 25 floors (Figure 1b).

The individual building is the Hạ Long New Day 2 hotel, a 5-story structure with an area of approximately 70 m<sup>2</sup>, located as shown in Figure 1 (yellow boundary). The area surrounding the building is quite open. Architecturally, the building has a simple design typical of small hotels, with the front featuring large glass windows on the first floor and smaller windows on the upper floors (Figure 1c).

The neighboring villa consists of two rows of 5-story houses facing away from each other, currently in the handover and usage phase. The architecture is characterized by square geometric shapes, numerous glass windows, and uniformity among the units (Figure 1d).

## 2.2. Methodology

The methodology of this study can be categorized into three phases: data acquisition, data processing, result and accuracy assessment (Figure 2).

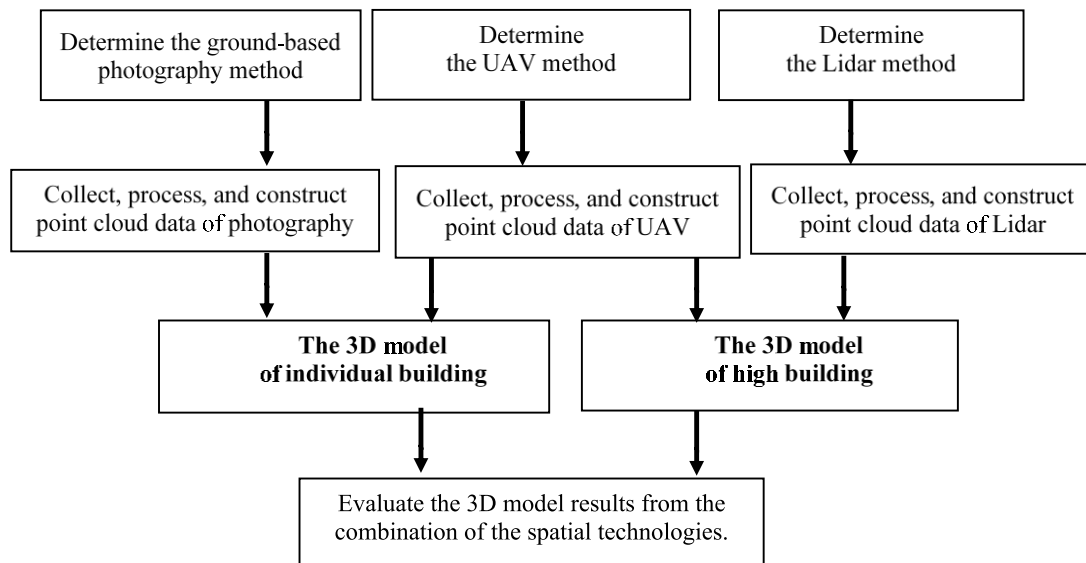


**Figure 2.** The flowchart of study.

### 2.2.1. Data acquisition

#### a) TLS data collection

FARO FOCUS<sup>3D</sup> X130 TLS has been used as the main scanning system to capture point cloud data from different locations. During the field operation, 11 scans have been completed around the high building to capture the details of the building and create a good overlap between the scans (Figure 3a). FARO FOCUS<sup>3D</sup> X130 has an integrated camera that allows the acquisition of the images needed to assign RGB values to every single point cloud.

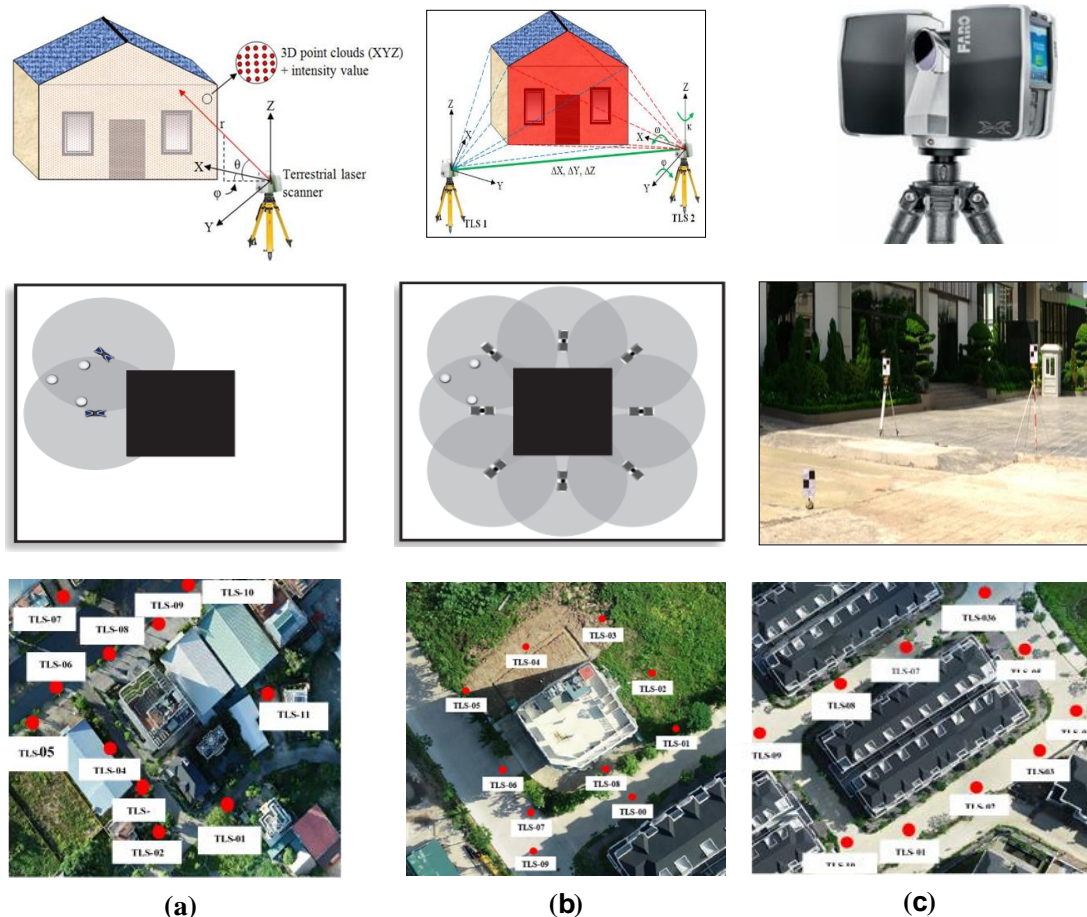


**Figure 3.** FARO FOCUS3D X130 TLS has been used to collect data.

**b) UAV image acquisition**

The UAS data acquisition has been performed using a low-cost DJI Phantom 4 Pro, in order to acquire a complete coverage of the building of interest, the flights have been planned and then executed for high building, individual building, and neighboring villa (Figure 4).

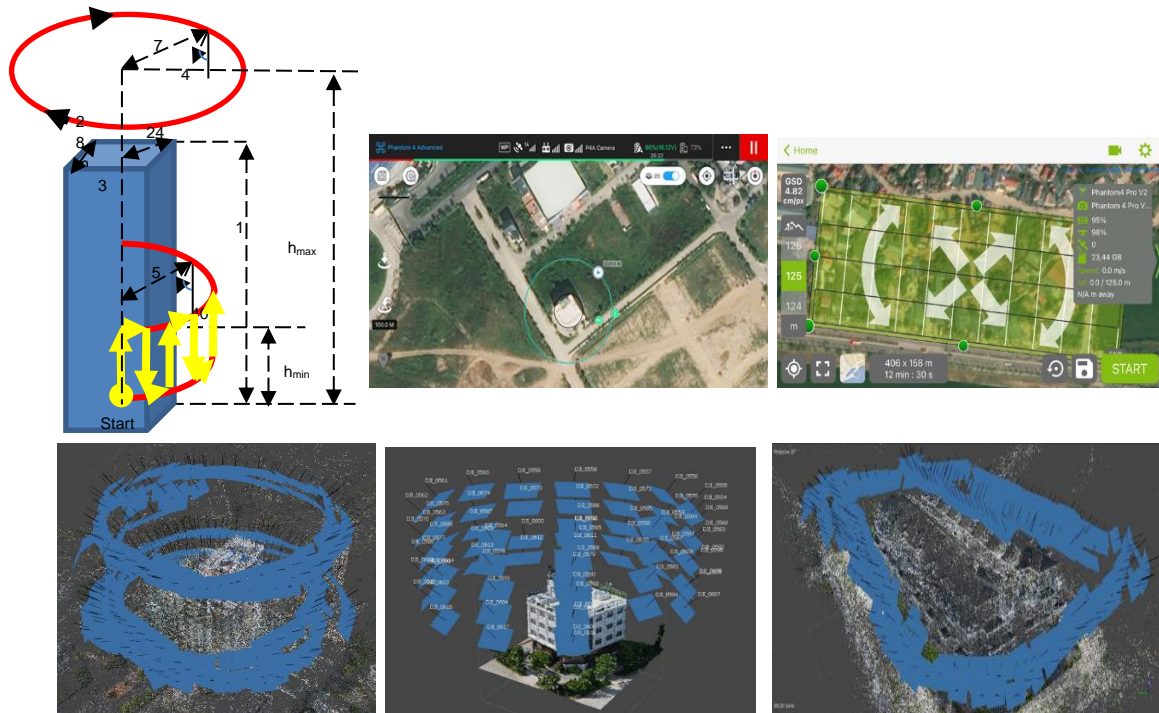


**Figure 4.** Data acquisition techniques by DJI Phantom 4 Pro V2.0.

**c) Ground-Based digital camera data collection**

The task of designing the photo capture route essentially involves arranging the digital photography stations. Based on the accuracy requirements, camera parameters, and the characteristics of the field, the parameters for each ground photo capture route for buildings are determined (Figure 5).

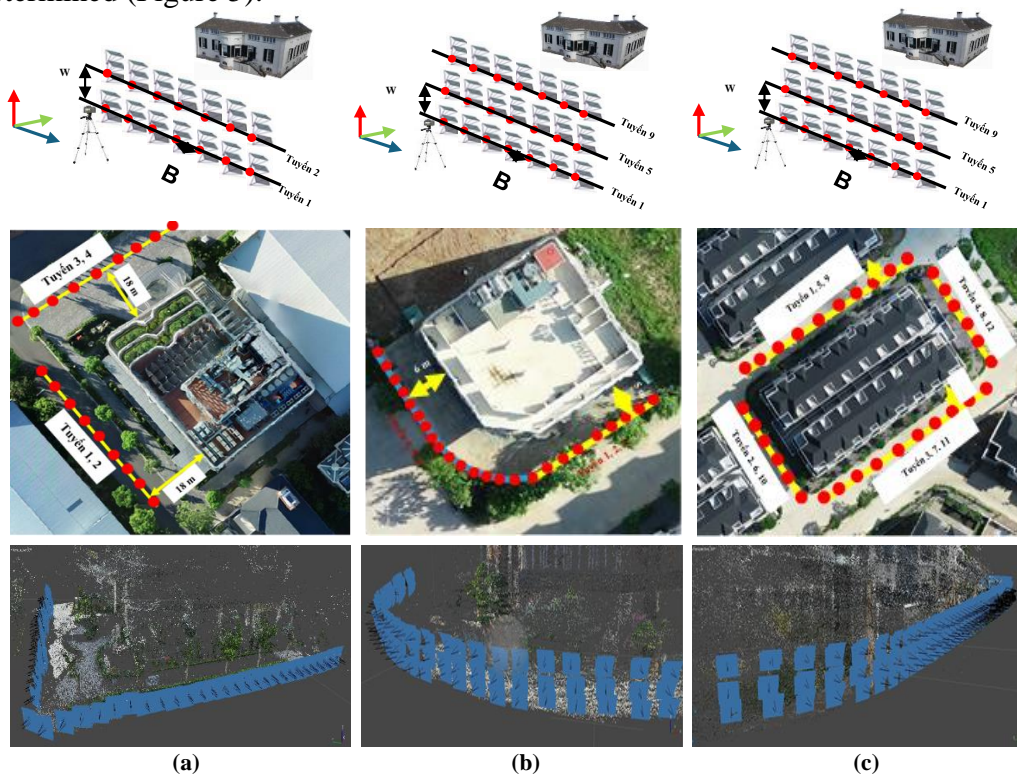


**Figure 5.** The collected data from the terrestrial camera (TC).

### 2.2.2. Data processing

Integration of point clouds from multi-sensor: To improve the accuracy of the point cloud after merging, the ICP method is used [24]. Before concatenation, the UAV, TC and TLS point clouds are filtered for noise (Figures 6, 7). Filter noise from point clouds to remove points of unimportant objects such as wires, trees, etc. or points that were wrong in previous processing. In addition, noise filtering also reduces the capacity of the point cloud. Because the TC and TLS point cloud have a higher density of points and higher accuracy, it is used as the base point cloud and the UAV point cloud is the composite point cloud.

The data concatenation process consists of two steps: Coarse Alignment and Fine Alignment. In which, in the raw coupling step, it is necessary to select at least 4 duplicate points on two points cloud. This can be a focal point, a control point, or a sharp feature on two points cloud. During the exact matching stage, there is a notable increase in the number of points involved in the matching process, resulting in enhanced accuracy of data matching albeit at the expense of longer processing time. The concatenation of point cloud data in both steps is executed using Cloudcompare software.

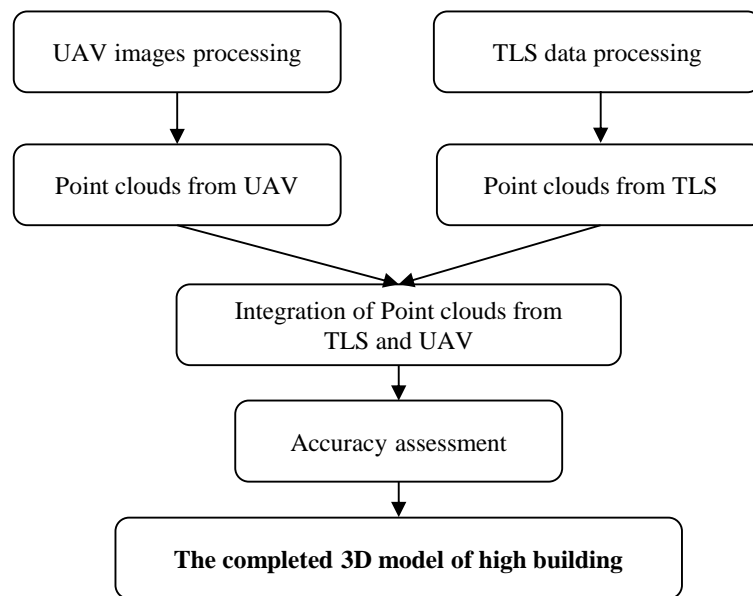


**Figure 6.** Flowchart in data processing phase for high building.

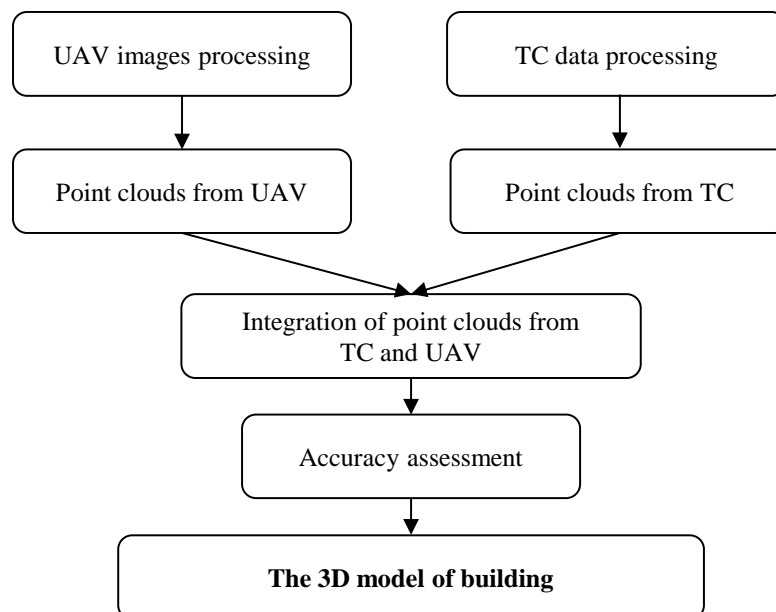


**Figure 7.** Flowchart in data processing phase for individual building and neighboring villa.

### 2.2.3. Accuracy assessment

To evaluate the accuracy of 3D point clouds integrating geospatial technologies of construction projects, it is necessary to arrange the above image control points on the surface and around high buildings and independent buildings, and adjacent villa area. The points are arranged evenly on all sides of the building, with the point layout diagram as shown below.

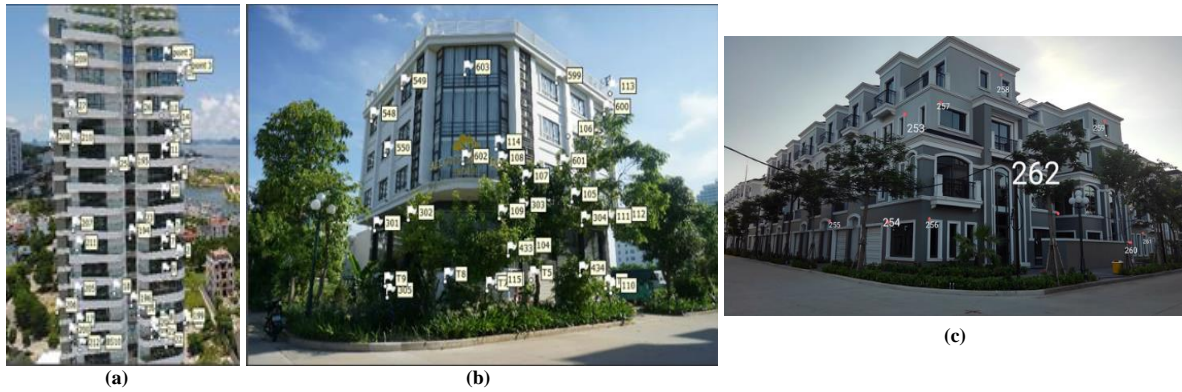


**Figure 8.** Distribution of image control points and checkpoints.

## 3. Results and discussion

### 3.1. Points cloud data of buildings

#### a) Point clouds from TLS data

The processing TLS data includes steps: (1) create project, (2) import data of scanning stations (Import), (3) process scan stations (Processing), (4) merge scan stations and evaluate accuracy (Registration), (5) create a cloud point cloud (Create point cloud), and export point cloud (Export).

With TLS data, scans are dumped in SCENE software, handling point clouds creation and station pairing. The result of the processing is point clouds as shown in Figure 9.

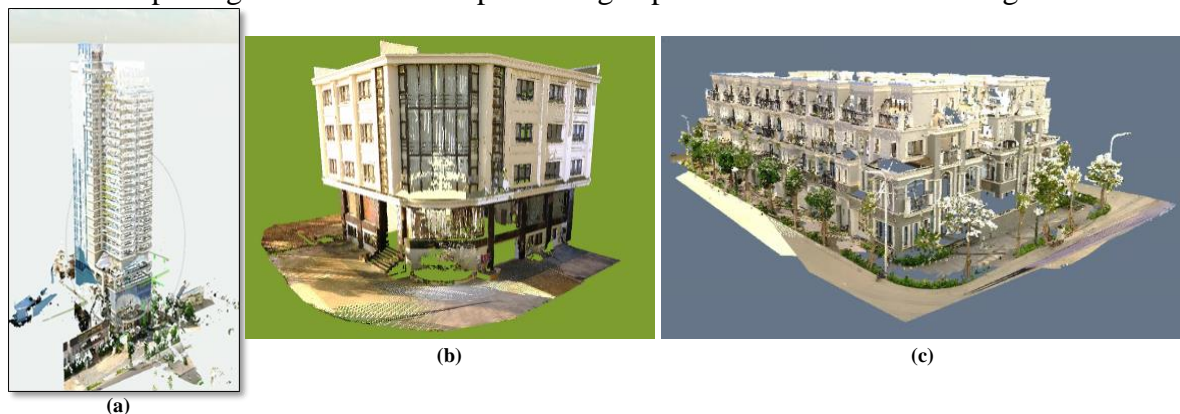


**Figure 9.** Point clouds from TLS data.

The data scanned from the FARO FOCUS3D X130 TLS device was transferred to a computer and processed using the SCENE software. The stations were aligned, and the accuracy was assessed, and the results were exported in E75 format. The outcome of the processing is point clouds as shown in Figures 9a-9c.

#### b) Point clouds from UAV images

UAV image data processed on the software is Agisoft Metashape. Software Agisoft uses SfM algorithms include steps: (1) Identify the above features image through using a special transformation algorithm multi-scale feature (SIFT); (2) Matching points featured; (3)



Orientation in and out of the image; (4) Creating dense point clouds. The result of the processing is point clouds as shown in Figure 10.

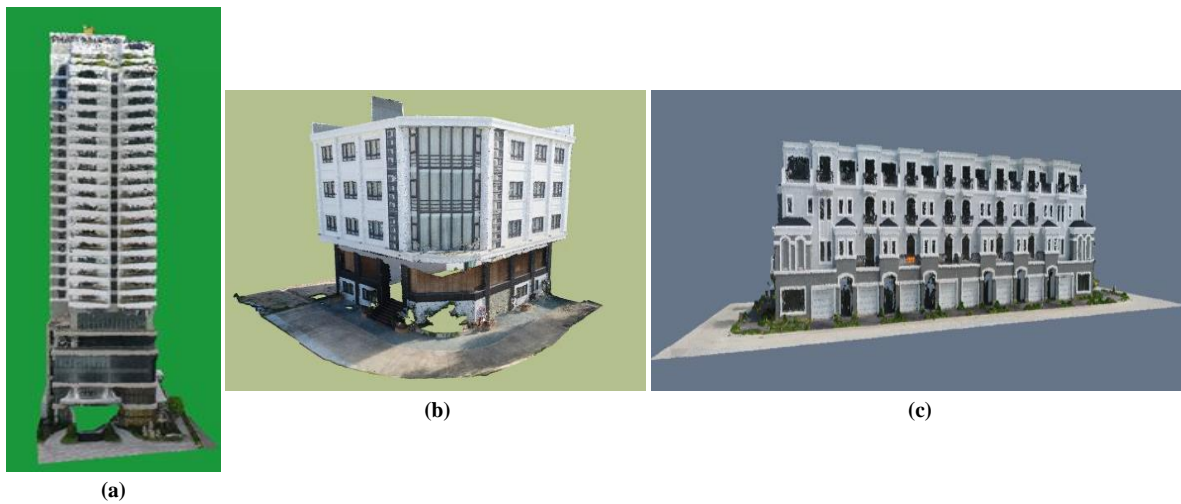


**Figure 10.** Point clouds from UAV data.

The creation of 3D models and processing of UAV images for high buildings, independent buildings, and adjacent villas were conducted using the specialized software Agisoft Metashape. This process yielded a dense point cloud for the high building, individual building, and adjacent villa, as illustrated in Figures 10a-10c.

c) Point clouds from terrestrial camera (TC) data

The terrestrial camera image data processed on the software is Agisoft Metashape. Software Agisoft uses SfM algorithms include steps: (1) Identify the above features image through using a special transformation algorithm multi-scale feature (SIFT); (2) Matching points featured; (3) Orientation in and out of the image; (4) Creating dense point clouds. The result of the processing is point clouds as shown in Figure 11.

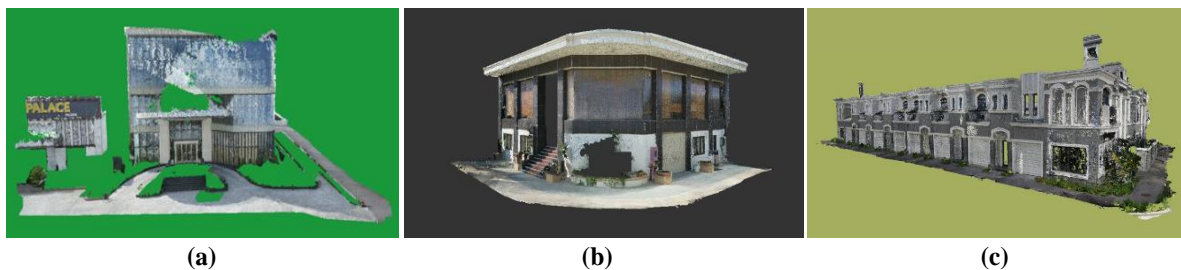


**Figure 11.** Point clouds from TC data.

Processing ground-based images and creating 3D models were conducted using the specialized image processing software Agisoft Metashape. The procedure was similar to processing UAV images. The result is a point cloud model of the high building, independent buildings, and adjacent villas, as shown in Figures 11a-11c.

*3.2. Multi-sensor points cloud data fusion for 3D building models*

a) Integration of point clouds from UAV and TLS for the high building

The iterative closest point (ICP) algorithm consistently converges monotonically to the nearest local minimum of a mean-square distance metric. Empirical evidence indicates that the convergence rate is especially fast in the initial iterations. Consequently, with an appropriate set of initial rotations and translations for a specific class of objects characterized by a certain “shape complexity”, it is possible to globally minimize the mean-square distance metric across all six degrees of freedom by evaluating each initial alignment (Figures 12-14).

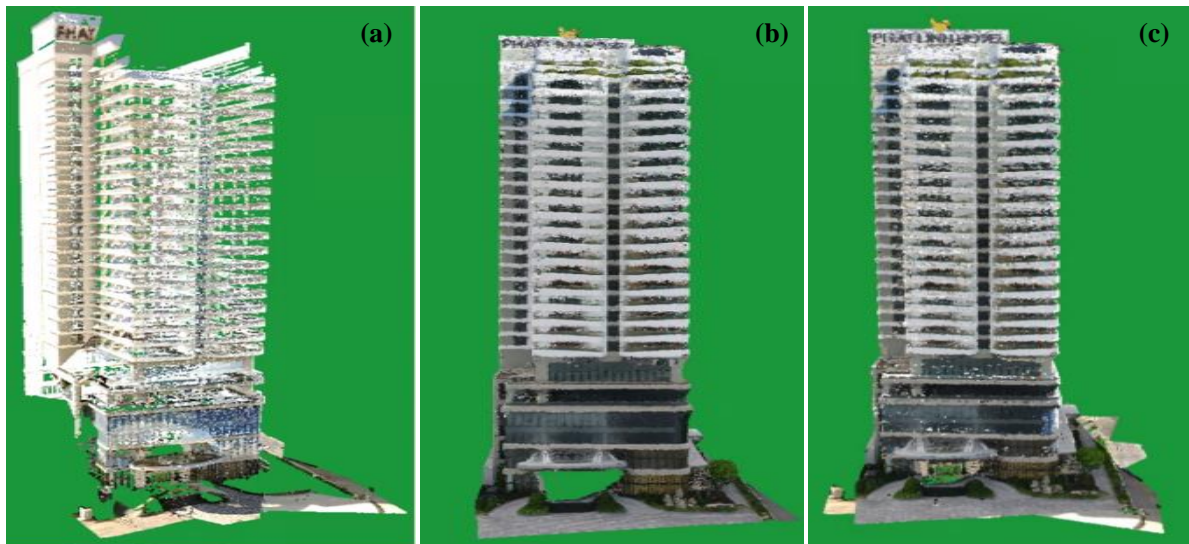


**Figure 12.** High building’s TLS point cloud after noise filtering (a), High building’s UAV point cloud after noise filtering (b), High building’s UAV and TLS point cloud after precision matching (c).

b) Integration of point clouds from UAV and TC for the independent building and neighboring villa



**Figure 13.** Independent building’s TC point cloud after noise filtering (a), Independent building’s UAV point cloud after noise filtering (b), Independent building’s UAV and TC point cloud after precision matching (c).

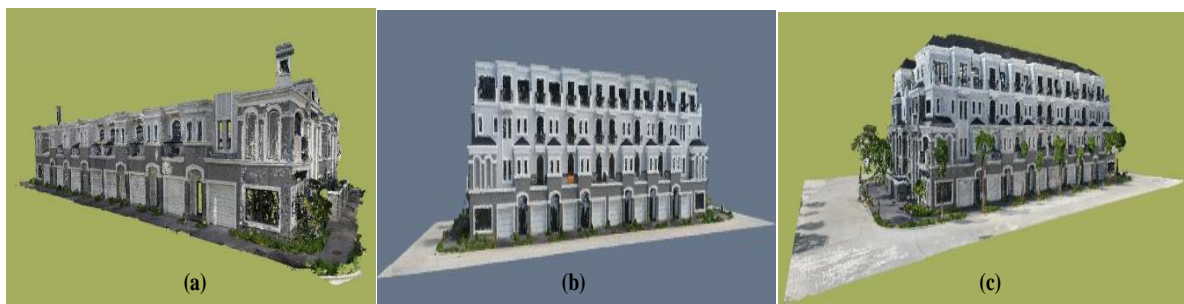


**Figure 14.** Neighboring villa’s TC point cloud after noise filtering (a), Neighboring villa’s UAV point cloud after noise filtering (b), Neighboring villa’s UAV and TC point cloud after precision matching (c).

### 3.3. Accuracy assessment

The reliability of these datasets was assessed by calculating the root mean square error (RMSE) between the coordinates of points on the generated orthophoto and those obtained from GPS measurements. A lower RMSE value signifies higher accuracy. The value of RMSE is shown in Tables 1-3.

**Table 1.** Results of assessing the accuracy of point clouds fusion from UAVs and TLS of high building.

No	$M_x$ (cm)	$M_y$ (cm)	$M_p$ (cm)	$M_h$ (cm)
3	-0.8	-0.8	1.1	0.9
6	0.4	-3.2	3.3	-1.7
18	4.4	-0.6	4.4	6.1
23	3.8	2.0	4.3	4.3
197	-2.3	-2.9	3.7	-0.9
203	-6.3	-1.9	6.5	-0.7
205	-5.9	-5.7	8.2	-2.4
212	-2.0	4.4	4.8	-19.5
RMSE	3.8	3.1	5.0	7.5

The results of assessing the accuracy of point clouds fusion from UAVs and TLS of high building are presented in Table 1. The root mean square errors are  $m\Delta x = 3.8$  cm;  $m\Delta y = 3.1$  cm;  $m\Delta z = 5.0$  cm. With the accuracy of the checkpoints as shown in Tables 1, the 3D model can fully achieve high accuracy.

**Table 2.** Results of assessing the accuracy of point clouds fusion from UAVs and TC of independent building.

No	$M_x$ (cm)	$M_y$ (cm)	$M_p$ (cm)	$M_h$ (cm)
599	-0.36006	-1.08958	1.14753	-2.3491
107	0.187597	0.561629	0.592132	0.46285
105	-0.26855	0.225359	0.350582	0.238866
549	-1.3453	-2.81343	3.118529	-0.76773
RMSE	0.715331	1.53857	1.69673	1.26283

**Table 3.** Results of assessing the accuracy of point clouds fusion from UAVs and TC of neighboring villa.

No	$M_x$ (cm)	$M_y$ (cm)	$M_p$ (cm)	$M_h$ (cm)
244	-0.5	1.1	1.2	1.9
245	-0.7	1.6	1.7	4.0
246	-0.3	-2.7	2.7	2.8
267	-0.7	0.3	0.7	-0.2
269	-1.3	-0.8	1.5	-1.3
276	-1.8	-1.1	2.1	-0.3
206	0.4	-0.5	0.7	0.2
209	2.1	0.4	2.1	-0.9
211	0.4	-0.4	0.6	3.2
212	0.9	-1.7	1.9	-1.3
RMSE	1.4	1.3	1.7	2.1

The results of assessing the accuracy of point clouds fusion from UAV and TP technologies for independent building and adjacent villa rows are presented in Tables 2 and 3. Based on the coordinate measurements (x, y, z) of the characteristic points on the terrain, including door and building corner angles (in Figures 8b, c), directly on the 3D model of the point cloud obtained after processing the image capture results, and used for comparison with the coordinate measurements (x, y, z) of the corresponding characteristic points measured by the non-prism mode of the total station. With the accuracy of the checkpoints as shown in Table 2, Table 3, the 3D model can fully achieve accuracy in terms of the horizontal plane and height for the 1:500 scale topographic map.

### 3.4. Discussion

From the results of the 3D point clouds and the assessment process of the accuracy of the merged point clouds from different technologies, it is evident that this integration process has generated complete point clouds, each technology exhibiting its own advantages and

disadvantages. Each device allows for the measurement and representation of a portion of the object (e.g., independent building). Therefore, a solution combining devices and technologies to fully measure and represent an object needs to be proposed, tailored to specific cases as demonstrated in this study. For high buildings with more than 10 floors, the combination of UAV and TLS technologies proves to be more reasonable and effective.

For buildings with 10 floors or fewer, combining UAV and terrestrial photogrammetry (TP) technologies would be more reasonable and effective. The reason is that terrestrial photogrammetry technology is more cost-effective than lidar scanning but provides comparable accuracy. However, the limitation of this method is that the data collection process outside the field is longer, and the distance from the terrestrial photogrammetry image capture point to the object must be calculated reasonably to obtain dense and accurate point clouds.

#### 4. Conclusion

This study has proposed a comprehensive process for constructing complete 3D models for several distinctive construction projects in coastal urban areas. The overall procedure is proposed with the integration of geospatial technologies, including UAV aerial photography, ground-based photography, and terrestrial LiDAR scanning, to build highly accurate 3D models for the research area, which is suitable for the current technological and human resource conditions in Vietnam.

The findings of this study recommend that for high buildings with more than 10 floors, the combination of UAV and TLS technology proves to be more reasonable and effective. Meanwhile, for buildings with 10 floors or fewer, integrating UAV technology with terrestrial photogrammetry (TP) would be more reasonable.

In our study, we constructed 3D building models using point clouds generated from data collected by low-cost DJI Phantom 4 Pro drone equipment and the Sony 7R ground-based camera, and the FARO FOCUS3D X130 TLS. The point clouds derived from the Sony and FARO FOCUS3D X130 TLS devices were dense and provided high resolution; however, they had limitations in coverage, especially for building roofs. On the other hand, the point clouds generated by the UAS presented a comprehensive building model, albeit with lower resolution. The integration of these technologies is a trend that future research in Vietnam is likely to increasingly adopt.

**Author contribution statement:** Generating the research idea; statement of the research problem; analysis of research results and data preparation; wrote the draft manuscript: H.T.T.L.; Analyzed and interpreted the data, wrote the draft manuscript: H.T.T.L.

**Competing interest statement:** The authors declare no conflict of interest.

#### References

1. Bouziani, M.; Chaaba, H.; Ettarid, M. Evaluation of 3D building model using terrestrial laser scanning and drone photogrammetry. *Int. Arch. Photogramm. Remote Sens. Spatial Inf. Sci.* **2021**, *XLVI-4/W4-2021*, 39–42.
2. Nex, F.; Remondino, F. UAV for 3D mapping applications: a review. *Appl. Geomatics* **2013**, *6(1)*, 1–15.
3. Böhm, J.; Brédif, M.; Gierlinger, T.; Krämer, M.; Lindenberg, R.; Liu, K.; Michel, F.; Sirmacek, B. Te IQmulus urban showcase: automatic tree classification and identification in huge mobile mapping point clouds. *Int. Arch. Photogramm. Remote Sens. Spatial Inf. Sci.* **2016**, *XLI-B3*, 301–307.
4. Kaartinen, H.; Hyypä, J.; Kukko, A.; Jaakkola, A.; Hyypä, H. Benchmarking the performance of mobile laser scanning systems using a permanent test field. *Sensors* **2012**, *12(12)*, 12814–12835.
5. Früh, C.; Zakhor, A. An automated method for large-scale, ground-based city model

- acquisition. *Int. J. Comput. Vision* **2004**, *60*(1), 5–24.
6. Tack, F.; Buyuksalih, G.; Goossens, R. 3D building reconstruction based on given ground plan information and surface models extracted from spaceborne imagery. *ISPRS J. Photogramm. Remote Sens.* **2012**, *67*, 52–64.
  7. Colomina, I.; Molina, P. Unmanned aerial systems for photogrammetry and remote sensing: A review. *ISPRS J. Photogramm. Remote Sens.* **2014**, *92*, 79–97.
  8. Fischer, A.; Kolbe, T.H.; Lang, F.; Cremers, A.B.; Förstner, W.; Plümer, L.; Steinhage, V. Extracting buildings from aerial images using hierarchical aggregation in 2D and 3D. *Comput. Vision Image Understanding* **1998**, *72*(2), 185–203.
  9. Stilla, U.; Soergel, U.; Toennessen, U. Potential and limits of InSAR data for building reconstruction in built-up areas. *ISPRS J. Photogramm. Remote Sens.* **2003**, *58*(1-2), 113–123.
  10. Wang, Y.; Huang, X.; Gao, M. 3D model of building based on multi-source data fusion. *Int. Arch. Photogramm. Remote Sens. Spatial Inf. Sci.* **2022**, *XLVIII-3/W2-2022*, 73–78. <https://doi.org/10.5194/isprs-archives-XLVIII-3-W2-2022-73-2022>.
  11. Whitehead, K.; Hugenholtz, C.H. Remote sensing of the environment with small unmanned aircraft systems (UASs), part 1: A review of progress and challenges. *J. Unmanned Vehicle Syst.* **2014**, *2*, 69–85. <https://doi.org/10.1139/juvs-2014-0006>.
  12. Ha, L.T.T.; Long, N.Q. Combination of UAV image and terrestrial photogrammetry to build 3D geospatial data for smart cities. *J. Hydro-Meteorol.* **2013**, *749*, 21–31. [https://doi.org/10.36335/VNJHM.2023\(749\).21-31](https://doi.org/10.36335/VNJHM.2023(749).21-31).
  13. Barnhart, T.B.; Crosby, B.T. Comparing two methods of surface change detection on an evolving thermokarst using high-temporal-frequency terrestrial laser scanning, Selawik River. *Alaska Rem. Sens.* **2013**, *5*, 2813–2837. <https://doi.org/10.3390/rs5062813>.
  14. Erdélyi, J.; Kopác'ik, A.; Lipták, I.; Kyrinovic, P.; Automation of point cloud processing to increase the deformation monitoring accuracy. *Appl. Geomat.* **2017**, *9*(2), 105–113. <https://doi.org/10.1007/s12518-017-0186-y>.
  15. Fan, J.; Wang, Q.; Liu, G.; Zhang, L.U.; Guo, Z.; Tong, L.; Peng, J.; Yuan, W.; Zhou, W.; Yan, J.; Perski, Z.; Sousa, J. Monitoring and analyzing mountain glacier surface movement using SAR data and a terrestrial laser scanner: A case study of the Himalayas North Slope Glacier Area. *Rem. Sens.* **2019**, *11*(6), 625. <https://doi.org/10.3390/rs11060625>.
  16. Xu, Z.; Xu, E.; Wu, L.; Liu, S.; Mao, Y. Registration of terrestrial laser scanning surveys using terrain-invariant regions for measuring exploitative volumes over open-pit mines. *Rem. Sens.* **2019**, *11*(6), 606. <https://doi.org/10.3390/rs11060606>.
  17. Harmening, C.; Neuner, H. A spatio-temporal deformation model for laser scanning point clouds. *J. Geod.* **2020**, *94*, 1–25. <https://doi.org/10.1007/s00190-020-01352-0>.
  18. Whitehead, K.; Hugenholtz, C.H. Remote sensing of the environment with small unmanned aircraft systems (UASs), part 1: A review of progress and challenges. *J. Unmanned Vehicle Syst.* **2014**, *2*, 69–85. <https://doi.org/10.1139/juvs-2014-0006>.
  19. Sayab, M.; Aerden, D.; Paananen, M.; Saarela, P. Virtual structural analysis of Jokisivu open pit using “structure-from-motion” unmanned aerial vehicles (UAV) photogrammetry: Implications for structurally-controlled gold deposits in Southwest Finland. *Rem. Sens.* **2018**, *10*, 1–17. <https://doi.org/10.3390/rs10081296>.
  20. Chhatkuli, S.; Satoh, T.; Tachibana, K. Multi sensor data integration for an accurate 3D model generation. *Int. Arch. Photogramm. Remote Sens. Spatial Inf. Sci.* **2015**, *XL-4/W5*, 103–106. <https://doi.org/10.5194/isprsarchives-XL-4-W5-103-2015>.
  21. Hannes, P.; Martin, S.; Henri, E. A 3-D model of castle Landenberg (CH) from combined photogrammetric processing of terrestrial and UAV based images. *Int.*

*Arch. Photogramm. Remote Sens. Spatial Inf. Sci.* **2008**, *37*, 93–98.

22. Long, V.P.; et al. Flying and taking photos with an unmanned aerial vehicle (UAV) creates a 3-dimensional (3D) spatial map. *J. Surv. Mapp. Sci.* **2017**, *31*, 23–28.
23. Duy, B.T. Constructing a three-dimensional model of Hanoi National University using handheld cameras and its applications in this three-dimensional model, Project code: QC.05.02. Summary report of the national university-level scientific research project conducted by the University of Technology and Management. 2011, pp. 60.
24. Hu, Z. ICP algorithm for 3D surface registration. *Highlights Sci. Eng. Technol.* **2022**, *24*, 94–98.

*Research Article*

## **A review on baseflow separation methods**

**Nguyen Y Nhu<sup>1\*</sup>**

<sup>1</sup> Vietnam National University, University of Science; nguyennhu@hus.edu.vn

\*Corresponding author: nguyennhu@hus.edu.vn; Tel.: +84–869110757

Received: 27 April 2024; Accepted: 5 June 2024; Published: 25 September 2024

**Abstract:** Baseflow separation is essential for effective water management, drought assessment, and groundwater resources protection. Despite its importance, baseflow observations are often limited to small-scale studies. To address this limitation, researchers have developed various baseflow separation methods. This paper reviews and analyzes existing studies which have developed or used the baseflow separation methods. A total of 43 studies are described, with a detailed review of 26 of them, focused on baseflow separation methods. Even if existing methods have already focused on baseflow separation, however, various methods produce divergent outcomes, primarily due to the inherent challenges in directly observing the flow process associated with each technique. A minority of methods are anchored in physical science, particularly noticeable during waning streamflow periods. Notably, certain methods dynamically adjust baseflow estimates in response to precipitation intensity, an approach that, while intuitive, lacks a physical rationale and introduces subjectivity, especially when precipitation events conflate. Filter methods, despite their apparent rigor compared to graphical techniques, they suffer from a lack of physical underpinning regarding their operational frequency and orientation and are often constrained by arbitrary limits to avert baseflow estimates from surpassing total streamflow or descending into negative values. While the process-based methodology enhances accuracy by employing physical principles to gauge baseflow across both arid intervals and rainy spells, the veracity of hydrological models is intimately tied to the data's availability and integrity. The main recommendations resulting from this review are that combining the strengths of different baseflow separation methods can lead to more robust results. For example, starting with a digital filter method for initial separation and refining it with physical-based approaches. Leveraging advancements in computational power and algorithms can help in handling complex calculations and iterative processes more efficiently, leading to more accurate baseflow estimations.

**Keywords:** Baseflow separation; Graph separation; Isotope; Digital filters; Process-based; Subsurface flow.

---

### **1. Introduction**

In the context of precipitation within a watershed, the flow pathway is established at the outlet of the basin, encompassing various water sources. Distinguishing the proportions of these different flow components necessitates dividing the flow into surface flow and base flow [1–2]. Studying baseflow characteristics is crucial for understanding runoff processes, streamflow interactions, and groundwater significant. Researchers also examine baseflow recession, spatial and temporal scale, to estimate aquifer parameters from streamflow data [3–6]. Specifically, the base flow separation, also known as the hydrological flow component or groundwater component, represents a fundamental problem in both technical hydrology and applied hydrology. It involves analyzing terrain slopes and calculating convergence, which significantly influences the overall hydrological behavior.

Generally, base flow constitutes the lower portion of the hydrograph with minimal variability. It finds application in industrial and agricultural water supply, water resource security, non-point source pollution assessment, water resource evaluation, and flow regime modeling [7]. During dry seasons, base flow serves as the primary contributor to river flow, maintaining the baseflow regime and playing a crucial role in sustaining ecosystems, providing stable water supply for livelihoods, and safeguarding ecological environments. Furthermore, the separation of base flow has substantial implications for regional water resource planning and protection of stream ecosystems.

Base flow separation methods are tools used to distinguish between base flow and stormflow within a river’s discharge. These methods are crucial for hydrological studies because they allow us to understand and quantify the contribution of groundwater to river flow, which is vital for managing water resources sustainably. However, our understanding of base flow dynamics remains incomplete. The separation of base flow remains a challenge in hydrological and ecohydrological research. Scholars both within and beyond national borders have shown widespread interest in this topic in recent years, resulting in notable advancements and breakthroughs. While various separation methods exist, most of them rely on empirical approaches based on flow characteristics. These methods often use graphical techniques or mathematical formulas to separate the hydrograph, the graphical representation of streamflow over time, into its different components. Achieving a consensus on base flow separation is challenging due to the interdisciplinary nature, involving climatology, physical geography, hydrogeology, and other scientific domains. The scarcity of experimental data further complicates the development of universally accepted methods. Despite extensive discussion and development of separation methods, comprehensive analysis comparing these available methods is lacking. This gap hinders the ability of hydrologists and water managers to select the most appropriate method for their specific context. Our research is the first attempt to address this gap by providing a systematic review of base flow separation methods. We evaluate their development and assess their application in contemporary hydrological studies. By highlighting the strengths and limitations of each method, we offer guidance for researchers to choose suitable techniques for their unique environmental and hydrological conditions. This work has the potential to significantly influence hydrology, ecology, hydrogeology, and water management by providing a clearer understanding of base flow dynamics and improving the selection process for separation methods.

## 2. Baseflow component

Baseflow, originating from groundwater aquifers [8–9], or other delayed sources [1, 7, 10], seeps into the groundwater and contributes to streamflow. It can also be categorized as shallow baseflow (from upper subsurface layers) and deep baseflow (from deeper sources). Deep baseflow provides consistent streamflow even during prolonged droughts. Total flow combines baseflow and direct runoff, with baseflow index (BFI) quantifying the groundwater’s contribution. Hydrograph separation distinguishes surface flow from baseflow.

Baseflow is the average flow during the driest periods over recent years, as estimated in hydrological forecasts. Baseflow helps prevent excessively prolonged water drawdown if it constitutes a significant proportion of the total flow. Typically,

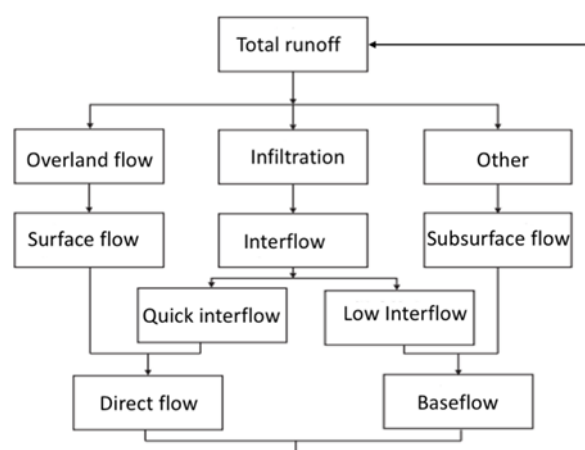


**Figure 1.** The flow components [11].



baseflow is truncated at a certain threshold level, and subsequent predictions and convergence are added back to the baseflow.

In the field of applied hydrology, the overall flow in rivers and streams is typically divided into two primary components. Surface flow refers to the runoff that occurs directly over the land surface during rainfall events. It includes water flowing over impermeable surfaces, such as roads, rooftops, and paved areas. Baseflow represents the sustained contribution of groundwater to streamflow. It is the portion of flow that persists even during dry periods when direct precipitation is minimal. Groundwater flow and subsurface flow (such as flow through soil layers) contribute to baseflow. However, these components cannot be entirely separated due to their interconnected nature. Groundwater flow and subsurface flow are not explicitly distinguished because they cannot be entirely separated.

Therefore, applied hydrologists differentiate between surface flow and baseflow, categorizing precipitation into direct runoff, infiltration, and other losses. Baseflow is generated, and the infiltration process replenishes soil water storage until saturation occurs. Any remaining infiltrated water eventually contributes to baseflow.

The process of streamflow formation is complex, involving interactions between surface water, subsurface flow, and groundwater. Hydrologists use various methods to study and quantify these components. Currently, the concept of baseflow in hydrograph separation primarily includes both subsurface flow and deep baseflow. This deep baseflow results from delayed contributions, such as lateral groundwater flow or other sources.

Concise summary of the characteristic features of baseflow based on research papers [9, 12, 13] as follow:

1. Before a runoff event begins, low flow primarily consists of baseflow.
2. Following the rising limb, the baseflow persists for some time.
3. Baseflow reaches its peak after the total runoff reaches peak as the sub-surface storage and routing effect.
4. Baseflow recession typically follow an exponential decay function.
5. The baseflow rejoin the total flow as quickflow ceases.

### **3. Materials and methods**

An analytical synthesis of forty-three scholarly inquiries dedicated to the formulation or application of baseflow separation was conducted. The term “baseflow” encompasses a spectrum of baseflow reseach.

#### *3.1. Search procedure*

To conduct a comprehensive search for literature on baseflow separation, the following strategies were used:

1. Terms and their combinations can be used: “Baseflow separation”; “Hydrograph separation”; “hydrograph analysis”; “Groundwater-surface water interaction”; “Streamflow components”; “Hydrological modeling and baseflow”; “Aquifer recharge estimation”. Boolean operators like “AND” and “OR” can be used to combine these terms for more refined searches, such as “baseflow separation AND hydrological modeling” or “groundwater-surface water interaction OR aquifer recharge”. These criteria and search terms will help ensure that the review is thorough, up-to-date, and relevant to the field of hydrology, particularly concerning the baseflow separation methods.

2. The selected data sources: Web of Science, Scopus, and Google Scholar combine rigor, breadth, and accessibility, ensuring a comprehensive review of baseflow separation methods. Researchers can confidently rely on these platforms to inform their investigations and advance hydrological science.

3. Beyond traditional databases, exploring institutional repositories, government reports, and technical bulletins can yield valuable insights. These sources often contain unpublished data and practical applications.

4. Studies published within a period from 1980 until now, to ensure the review captures the traditional as well as recent advancements in baseflow separation methods. Peer-reviewed articles, conference proceedings, and scientific reports to ensure the credibility and scientific validity of the information. Preference for articles published in journals with a high impact factor or a specific focus on hydrology and water resources. Studies that specifically address baseflow separation methods, including theoretical development, empirical studies, and application-based research. Papers that contribute to understanding the mechanisms of baseflow, its quantification, and the impact of different separation techniques on hydrological modeling.

### 3.2. Selection of studies and analytical criteria

Researchers initiate the selection process by systematically reviewing the titles and abstracts of relevant articles retrieved from databases. Articles that align with the study's focus on baseflow separation methods are retained for further evaluation.

The research conducted a thorough analysis by carefully selecting a subset of studies that significantly differed from others due to their unique characteristics, methodologies, or findings. Specifically, we focused on studies that proposed or employed techniques for baseline separation. This refined set consists of 26 chosen studies. In Section 4, we explore these 26 studies in detail.

## 4. Baseflow separation methods

Baseline separation methods encompass various techniques, categorizing these methods helps organize the diverse approaches, making it easier for researchers to understand and apply them, allow practitioners to quickly identify relevant techniques based on specific research goals or analytical requirements.

Efforts to distinguish baseflow from streamflow continuously over time can be grouped into four main approaches: (1) graphical, (2) tracer-based, (3) process-based approach, and (4) digital filter. Except for geochemical data, most of these methods rely solely on streamflow data. They are not universally applicable under all streamflow conditions and typically involve only a few parameters with well-defined physical interpretations.

### 4.1. Graphical Method

This hydrological approach involves graphically segmenting streamflow data to distinguish baseflow characteristics based on hydrological and geological features of different catchments. It assumes that between consecutive and distinct rainfall events, baseflow in a basin is equivalent to streamflow. In other words, during non-rainfall periods, the streamflow consists primarily of baseflow. To estimate baseflow under these conditions, a set of graphical extrapolation rules is applied to streamflow data. The hydrographs (Figure 2) before applying the separation method were compared with the after one. Or the tracer-based method has been used to verify the applied methods. It primarily includes the following techniques:

**Straight line Method:** This method connects flow with straight lines. Hydrologists use characteristic inflection points to segment baseflow, especially suitable for delineating baseflow and estimating groundwater resources in closed mountainous catchments. The segmentation is based on monthly average flow values, with a minimum flow threshold serving as the reference point. Below this threshold, the flow represents annual baseflow. In this approach, a diagonal line connects the flood peak and the inflection point of the recession limb in the daily streamflow hydrograph (Figure 3). The portion below this line corresponds

to baseflow. The vadose zone conditions play a crucial role: When the vadose zone is thick and intense rainfall occurs within a short period, preventing groundwater recharge, baseflow can be segmented using a horizontal line on the flow recession curve. Conversely, when the vadose zone is thin, and groundwater recharge increases after rain, an oblique line can be used to separate baseflow.

For long-term baseflow segmentation, hydrologists often choose representative years from streamflow records. They create average daily flow duration curves for each year and use maximum monthly flows during the dry season (typically over a 3-month period). The small value used as a reference for segmenting the base flow is determined through the cross-sectional method. This method involves identifying the peak discharge point and the inflection point (also known as the branching point) along the river. The process connects these two points with a straight line. For high-flow seasons and multi-stage flood events, it is necessary to divide the river into segments below the diagonal line, representing the base flow during the flood season, which supplements the flow during the dry season. In general, the peak elevation of the flood peak is more distinct and easier to determine, while the inflection point of the recession segment requires using a pre-established comprehensive low-flow point for assessment. The comprehensive recession curve is constructed by extracting and plotting a set of recession curves that exclude the influence of rainfall on the river flow. These curves are horizontally shifted to align the tails of each recession segment. The outer envelope of this set of recession curves represents the comprehensive recession curve.

The construction of a comprehensive recession curve is a complex task, and manual drawing calculations are time-consuming and inefficient. To improve computational speed and meet the accuracy requirements for planning and engineering design, many scholars turn to computer-based methods.

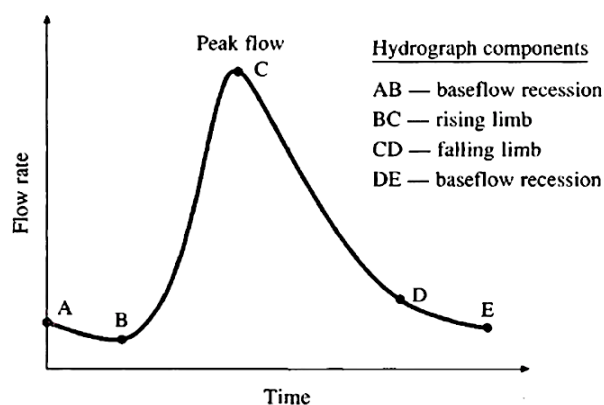


**Figure 2.** Components of discharge hydrograph [11].

**Fixed based method:** During a flood, the river has extra water, and this can seep into the ground, adding more water to the groundwater. After the flood, as the floodwater goes down, the baseflow also goes down because there is less water coming from the groundwater. Even after the flood, the groundwater can continue to feed the river, which increases the baseflow again. The inflection point is a spot in this process where things change direction - like when the base flow starts to increase after the flood. Where this point is located depends on how the river and the groundwater affect each other (Figure 3). The method described uses a time interval, called *N*, to measure how long it takes for the river to go from full flood back to normal [11].

**Tracing the flow:** Starting from when the floodwater has gone down, looking back in time to find where the water level started dropping quickly.

**Connecting points:** draw a line from this point back to a point on the graph that's *N* time units before the peak of the flood.

$$N = A^{0.2} \tag{1}$$

where *A* represents the catchment area; *N* denotes the direct runoff time. The typical time interval falls within the range of 3 to 11 days.

**Variable Slope Method:** Starting from the beginning of the surface flow, we extend the flow path forward as described above. Conversely, from the end point of the surface flow,

we extend the base flow path backward until it intersects a vertical line passing through the inflection point on the downstream water branch. Finally, we connect these intersection points with straight segments (Figure 3).

The graphical methods, exemplified by the work of the Institute of Hydrology [14] and Sloto and Crouse [15], use specific criteria to distinguish baseflow from surface runoff based on streamflow hydrograph analysis. By visually identifying recession limbs and inflection points, graphical methods provide insights into baseflow behavior. However, different graphical rules can lead to significantly different baseflow estimates using the same streamflow data. Some rules produce linearly increasing baseflow estimates during individual rainfall events, regardless of variations in rainfall and streamflow. However, these estimates may not be physically realistic. While the graphical approach is based on some physical reasoning, it is not always well-founded physically. One limitation is that it can become problematic when two or more rainfall events overlap [16]. Consequently, it is not particularly useful for baseflow separation over long periods of time.

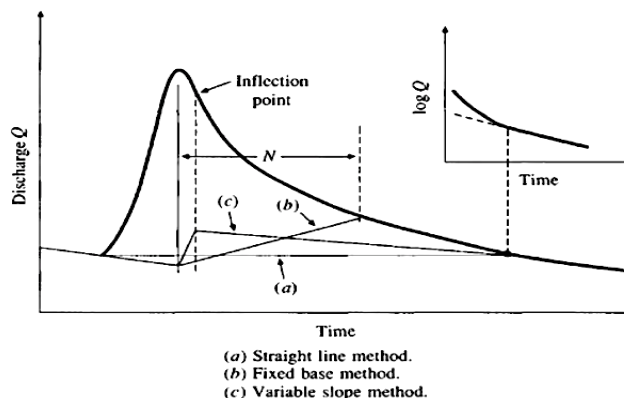


**Figure 3.** The diagram depicts the baseflow separation methods [11].

#### 4.2. Process-based approach

This method is also known as analytical approach, which based on fundamental rules governing the formation of subsurface flow. This approach solves equation related to storage, discharge, and water balance equations for underground reservoirs. It uses models to estimate plant water use, soil absorption capacity, and water penetration into underground layers. The approach characterizes each component of a river's base flow by its rate of change, origin, and the volume of water infiltrating from the ground. Mathematical models, such as the Sherman Unit Hydrograph and Horton Infiltration Equation, are employed to separate base flow from total streamflow. The Sherman Unit Hydrograph is instrumental in determining the flow process from rainfall-runoff to base flow, while the Horton Infiltration Equation is used to solve for base flow [17]. The widespread application of technologies (e.g., Remote Sensing, Geographic Information Systems), along with distributed hydrological models (e.g., SHE, SWAT, and TOPMODEL), provides effective methods for segmenting base flow within hydrological processes [18]. Birtles [19] represents the amount of water that infiltrates the ground surface and contributes to groundwater recharge. It includes rainfall, snowmelt, and other forms of precipitation that percolate into the soil. Birtles expressed groundwater recharge as a function of surface infiltration, curve-fitting parameters, groundwater recharge rate. This approach incorporated the subsurface processes to estimate groundwater recharge and provide valuable insights into the baseflow dynamics. The analytical approach in hydrology, while robust, the accuracy of hydrological models is heavily dependent on the availability and quality of data. In many cases, there might be a lack of spatial-temporal data, which can limit the effectiveness of the models. The baseflow index (BFI) and visual inspection are used to compare different methods.

#### 4.2. Isotopic hydrograph segmentation method

This approach involves separating streamflow into surface runoff and baseflow using various tracers. The consistency of the separated baseflow was evaluated with isotope-tracer

data [20–24]. Regarding isotopic hydrograph segmentation, there are currently three internationally recognized approaches:

1) Time-Based Separation: Divides the flow into event water and pre-event water, also referred to as “new water” and “old water”. Event water typically originates from rainfall, while pre-event water is stored prior to precipitation.

2) Mechanism-Based Separation: Classifies flow into Hortonian overland flow, variable-source slope flow, saturation-excess flow, interflow, and baseflow. These mechanisms account for changes in source conditions or varying slopes.

3) Geographical Separation: Based on spatial locations before water enters a stream, considering whether it is stored in the vadose zone or saturated zone. However, studies often do not explore the spatiotemporal distribution of isotopic abundance, and the flow pathway is divided into surface runoff and subsurface flow.

In reality, the isotopic composition of environmental water is influenced by factors such as precipitation amount, temperature, topography, and other conditions, with a wide range of variability. Additionally, the  $^{18}\text{O}$  isotopic signature in groundwater flow within a catchment exhibits significant variations during rainfall events, particularly in arid conditions. Although the spatial and temporal variations are small, neglecting the time-dependent changes in isotopic composition of precipitation would lead to serious errors in hydrograph segmentation. Researchers [25, 26] have utilized isotopes (including  $^{18}\text{O}$ ) in precipitation and river flow to delineate hydrological processes. They propose that the influence of subsurface flow cannot be overlooked in the flow pathway. Notably, the dominant input for observed dissolved aluminum concentrations can be attributed to subsurface flow [27–28].

The study [29] employed monitoring devices from three water sources to segment stormflow, revealing that the flow in the vadose zone significantly contributes to the stormflow component within the catchment.

Gonzales et al. [30] meticulously evaluated various baseflow estimation techniques within a lowland region in the Netherlands. Their investigation encompassed both tracer-based and non-tracer-based methods, shedding light on the intricate dynamics of groundwater-surface water interactions. The tracer approach revealed responsiveness of groundwater to rainfall events in the study area. During flood events, surface water predominantly contributed to the measured discharge. The rating curve method utilizes empirical relationships between streamflow and water stage (discharge rating curves). It provides reliable estimates of baseflow. Eckhardt’s [2] approach employs digital filters to separate baseflow from total streamflow. It also yielded robust baseflow values. In summary, their comprehensive analysis underscores the importance of both tracer-based insights and sophisticated estimation techniques in understanding baseflow dynamics. However, these approaches are always labor-intensive, require extensive data and sampling, and cannot be applied to past events due to the absence of necessary chemical data [30]. Chemical reactions during the mixing of components, tracer measurements, and elevation effects on the isotopic composition introduce uncertainties in tracer-based methods. These uncertainties can lead to less reliable baseflow estimation results.

### 4.3. Digital Filter Approach

To simplify the process of separation baseflow, various time series analysis methods have been proposed. These methods primarily include the digital filtering method, smooth minimal method, and time step method. The baseflow process line obtained using digital filter methods was compared with that obtained using isotope-tracer data to evaluate the performance of the applied method.

#### 4.3.1. Master recession curves (MRC)

The MRC method is a valuable tool for baseflow separation. It involves analyzing recession curves, which provide insights into hydrogeological processes related to

groundwater inflow and outflow. To construct the MRC, individual recession curves are aligned horizontally and cumulatively superimposed until the MRC includes most of the tail ends of recession curves. Researchers directly check the master recession curve to understand recession characteristics [32].

$$B_t = B_0 k^t \tag{2}$$

$$B_t = (B_0 - c)k^t + c \tag{3}$$

The exponential form (Equation (2)) is commonly used to fit the master recession. It provides a versatile way to model various streamflow behaviors. Equation (1) is an alternative form, but it has limitations in capturing the full range of streamflow variations.

The exponential form allows for a more flexible representation of baseflow dynamics. When fitting the master recession, it is preferable to use an extensive historical streamflow dataset rather than single events. Baseflow is a slow-moving process, and analyzing long-term data provides a more accurate representation of its behavior. To fit the master recession, hydrologists often perform initiating the analysis from the most current data points. This approach ensures that the most up-to-date information is considered when estimating baseflow. Hydrologists often visually fit the master recession curve to the streamflow data. This involves adjusting the parameters (such as (k) and (c)) until the fitted curve aligns well with the observed streamflow recession.

Duncan [32] demonstrate an effective method for baseflow separation, enhances our understanding of baseflow dynamics by accounting for variations across different sites. Typically, low flow preceding a hydrological event primarily consists of baseflow. The peak value occurs after the peak of total runoff. As quickflow (surface runoff) ceases, baseflow rejoins the total hydrograph. The baseflow recession follows an exponential function. During the rising limb (when discharge is increasing), modeled baseflow doesnot continue to decrease. Typically, one might expect all components of flow to increase as overall flow increases. However, it's essential to note that baseflow separation methods may not consistently preserve this feature.

The MRC approach comprises a single backward pass through the observed total flow data to fit an exponential master baseflow recession curve to smooth the connection between segments of the master recession. An additional constraint pro-hibiting negative quickflow, implied but not always stated in previous descriptions, must be strictly observed for correct operation of the smoothing algorithms.

#### 4.3.2. Nathan and McMahon's digital filtering method

The digital filtering technique was first applied for baseflow segmentation in 1990 [11]. Over recent years, this method has become the most widely used approach for baseflow segmentation worldwide. Its popularity stems from its ability to capture the rapid response of direct runoff processes in river basins. By combining characteristics of high-frequency signals (representing surface flow) and low-frequency signals (representing baseflow), the method effectively dissects the flow regime [2, 31]:

1. Separate the flow process into: direct flow and baseflow using digital filters.
2. The baseflow division equation [3] is as follows:
  - Surface flow at time step i:

$$Q_d(i) = \alpha Q_d(i-1) + \frac{1+\alpha}{2} [Q(i) - Q(i-1)] \tag{4}$$

- Baseflow at time step i:

$$Q_b(i) = Q(i) - Q_d(i) \tag{5}$$

where  $Q_d(i)$ ;  $Q_d(i-1)$  represent the filtered surface flow at time steps i and i-1;  $Q(i)$ ;  $Q(i-1)$  correspond to the total flow at time steps i and i-1;  $Q_b(i)$  represents the baseflow.

The filter coefficient  $\alpha$  is typically recommended to be 0.925 for daily discharge has been recommended [9, 11].

#### 4.3.3. Chapman’s modified equations for baseflow separation

Chapman [18] introduced modifications to Equation 12 as follows:

1. Direct Flow Component ( $Q_d$ ):

$$Q_d(i) = \frac{3\alpha - 1}{3 - \alpha} Q_d(i-1) + \frac{2}{3 - \alpha} [Q(i) - \alpha Q(i-1)] \quad (6)$$

2. Baseflow Component ( $Q_b$ ):

Chapman and Maxwell [18] suggest that during a specific time interval, the baseflow can be expressed as weighted average of the surface flow at the current and the previous time step:

$$Q_b(i) = kQ_b(i-1) + (1-k)Q_d(i) \quad (7)$$

where  $k$  represents the recession coefficient, typically set to 0.95.  $Q(i) = Q_b(i) + Q_d(i)$ , we can eliminate  $Q_d(i)$

$$Q_b(i) = \frac{k}{2-k} Q_b(i-1) + \frac{1-k}{2-k} Q(i) \quad (8)$$

3. Practical Application:

Researchers have compared various baseflow estimation techniques and found that Chapman and Maxwell’s proposed approach could be optimal in certain contexts [33]. The baseflow coefficients obtained using this method exhibit minor variability, and their Baseflow Index (BFI) remains relatively stable, within the range of 0.4 to 0.5. In practice, Equations 3 and 4 are commonly used as filtering equations:

$$q_t = \beta q_{t-1} + \frac{1}{2} (Q_t - Q_{t-1}) \quad (9)$$

$$b_t = Q_t - q_t \quad (10)$$

where  $q_t$  and  $q_{t-1}$  represent the filtered surface flow at  $t$  and  $t-1$ ;  $Q$  denotes the total flow;  $\beta$  is the filter parameter affecting baseflow attenuation. Empirical studies suggest that a value around 0.9 yields baseflow estimates that closely align with actual observations. In other words, this value helps us capture the real behavior of groundwater contributions to streamflow. Typically, values of 0.9, 0.925, and 0.95 are used for baseflow separation, with the most suitable parameters determined based on specific watershed characteristics. Factors like geology, vegetation, and climate influence the optimal value.

Arnold and Allen [34] conducted a rigorous study across six representative river basins in the western and eastern United States. They verified a method (likely the one using  $\beta$ ) and found that this method consistently produced similar results when applied multiple times, easy operation, few parameters which simplify the process, and fast implementation.

Mau and Winter [35] compared the results of the method (likely involving  $\beta$ ) with a graphic segmentation approach. The results showed good agreement between the two methods, reinforcing the reliability of the method using  $\beta$ .

#### 4.3.4. Eckhardt Filter method

Eckhardt [2] proposed the Eckhardt filter method, and its equation is as follows:

$$b_t = \frac{(1 - BFI_{max}) \alpha b_{t-1} + (1 - \alpha) BFI_{max} Q_t}{1 - \alpha BFI_{max}} \quad (11)$$

where  $\alpha$  represents the water retention constant, which can be determined through analysis of recession flow;  $BFI_{max}$  represents the maximum proportion of streamflow that comes from baseflow. Eckhardt [2] applied this method to study 65 randomly selected river

basins in the United States. They suggested that the  $BFI_{max}$  values for perennial rivers are 0.8, rivers have flow variations throughout the year (for seasonal rivers), the  $BFI_{max}$  value is 0.5, and the perennial rivers flow through hard rock formations, the  $BFI_{max}$  value for these rivers is 0.25.

The Eckhardt filter method is a powerful tool for baseflow separation. It operates by adjusting the Baseflow Index (BFI) values. When compared to alternative methods, the Eckhardt filter exhibits gradual changes in BFI, resulting in a smoother baseflow hydrograph. Under typical hydrological conditions, this filtering technique yields a more stable representation of baseflow. However, intriguingly, certain regions specifically semi-arid and humid areas deviate from this norm, especially where low-flow coefficients are small and intense rainfall occurs over short periods, river basins exhibit sharp and uneven hydrographs. These conditions are primarily due to excessive infiltration during high-flow periods and lower groundwater flow coefficients.

Xie et al. [36] conducted a study on 1,815 river basins across the United States to measure the baseflow. They used nine different methods that involve visual analysis and five that use computer algorithms to estimate these values. They applied a strict rule where only the water flow observed during dry periods was considered true baseflow. After analyzing the data, they determined that the method developed by Eckhardt was the most effective for predicting baseflow throughout the mainland United States, based on their extensive testing across all the river basins.

#### 4.3.5. Minimum smoothing method

This method divides an entire continuous streamflow sequence into non-overlapping blocks with a fixed width of 5 days. Within each block, the minimum value is determined, using a specified threshold. The rule involves identifying the minimum values to form inflection points and connecting these inflection points to obtain the baseflow hydrograph. This method is straightforward, easy to implement, and has been applied in various countries and regions.

Sun et al. [37] separated the baseflow from the total streamflow in the upper part of the Yitong River. This technique aims to estimate the maximum baseflow index ( $BFI_{max}$ ) accurately. The SMT aligns well with isotope-tracer data and exhibits stability and reliability in the Second Songhua River. Compared to other methods, it is believed that the smooth minimum method provides the smallest baseflow index values. However, there are certain challenges when applying this method for baseflow segmentation:

The lower envelope of the total streamflow, including some multi-segmented streamflow paths, is related to basin precipitation. The smooth minimum method includes partially unrecensed groundwater flow from previous floods, leading to increased groundwater flow and inconsistency with actual conditions. The baseflow hydrograph, defined as a smooth curve without inflection points, may not fully reflect the catchment's flow dynamics.

#### 4.3.6. The time-step method

It also known as the HYSEP method, is a computer program used for streamflow segmentation. It incorporates three different segmentation techniques: the fixed interval (FI), the sliding interval (SI), and the local minimum (LM) [16]. All three methods utilize empirical formulas to calculate direct runoff time:  $N = A^{0.2}$

where  $A$  represents the catchment area;  $N$  denotes the direct runoff time. The typical time interval falls within the range of 3 to 11 days. The nearest odd number to  $2N$  is chosen as the time interval, and baseflow calculations are performed based on this interval.

##### 1. Fixed Interval (FI):

For the time frame being studied, the smallest amount of water that was recorded flowing in the river each day is used to represent the baseflow.



The endpoint of this calculation is then used as the starting point for the next iteration.

**2. Sliding Interval (SI):**

For a given day, looking at a time range that extends  $(2N-1)/2$  days before and after that day. Within this time frame, we calculate the minimum flow rate. This minimum value is then used for analysis or comparison within the selected interval.

This value represents the minimum flow contributed by groundwater, baseflow, and a similar approach is used to calculate baseflow for the subsequent day.

**3. Local Minimum (LM):**

First, calculate the center within adjacent time steps.

The baseflow value at the center point, as well as the baseflow within the time range outside the center point, are determined using linear interpolation.

The method for calculating baseflow at the center point in the time step is as follows:

Choose the time interval of  $(2N-1)/2$  days before and after a minimum value day.

Assign this value as the baseflow for that day.

Then use the endpoint of this calculation as the starting point for the next iteration to compute baseflow at the center point of the subsequent time step.

Partington et al. [38] explored four ways to estimate baseflow. They considered methods like HYSEP [16], PART [39], BFLOW [32], and Hydro-GeoSphere (HGS) [40], HGS [40] ombined with a hydraulic mixing-cell approach, provided synthetic baseflow values for a V-shaped catchment. Li et al. [41] ested various recursive digital filters using synthetic data from HGS. The Lyne and Hollick filter performed well, closely matching HGS synthetic baseflow across diverse catchment conditions. Optimal filter parameters varied based on the specific hydrological context [2, 11, 17, 18, 42]. Su et al. [43] investigated the Eckhardt filter method. After calibrating it using hydrological signatures, the filter showed improved performance.

**Table 1.** Baseflow separation methods.

<b>Gourped approaches</b>	<b>Advantages</b>	<b>Disadvantages</b>
Graphical approaches	Based on physical reasoning	Problematic when multiple rainfall events overlap Not useful for baseflow separation over long periods.
Process-based	Based on fundamental rules governing subsurface flow Provide valuable insights into baseflow dynamics Shed light on intricate groundwater-surface water interactions.	Heavily dependent on the availability and quality of data Complexity involved
Tracer-based	Revealed groundwater responsiveness to rainfall events Provides reliable baseflow estimates	Labor-intensive, require extensive data and sampling Cannot be applied to past events due to the absence of necessary chemical data Uncertainty due to tracer measurements, and isotopic composition
Digital Filter	Yielded robust baseflow values	Lack a physical basis for application frequency and direction Limited by arbitrary constraints to prevent exceeding total streamflow or becoming negative. Focus on low-frequency streamflow, which is usually associated with baseflow. This might also contain quick surface runoff, especially after heavy rains

**4. Conclusion**

The study offers a in-depth perspective on baseflow separation methods, providing insights that are both practical and scientifically significant (Table 1). When comparing different methods for estimating baseflow from streamflow data, it’s clear that only a few

methods are grounded in physical science, particularly during periods when the streamflow is decreasing. Some methods estimate baseflow during rain events in a way that changes with the amount of rain, which seems logical but isn't based on physical principles. These methods can be very subjective, especially when rain events overlap.

The tracer-based technique provides an objective understanding of flow behavior and has gained recognition for its ability to study flow mechanisms, model moisture movement in soil, analyze water source components within a river basin, and monitor flow pathways.

Filter methods are more reliable in these cases and seem more rigorous than graphical methods. However, they too lack a physical basis for their application frequency and direction. They are also limited by arbitrary constraints to prevent baseflow estimates from exceeding total streamflow or becoming negative. Ideally, filters should work without these limits. Filters are designed to separate the steady baseflow from the total streamflow (Figure 1). These filters focus on the low-frequency part of the streamflow, which changes slowly and is usually associated with baseflow. However, some experts argue that this slow-changing part might also contain quick surface runoff, especially after heavy rains. This means that the filters might not be perfectly accurate.

The process-based approach improve this by using physical principles to estimate baseflow during both dry periods and when it's raining. Process-based method is more complex because it uses many different factors and an iterative process, which means it repeats steps to get closer to the correct estimate. But this complexity can also make it harder to get consistent results, especially when the streamflow changes rapidly, and the accuracy of hydrological models is heavily dependent on the availability and quality of data.

Various baseflow segmentation methods are known to produce divergent outcomes, primarily due to the inherent challenges in directly observing the flow process associated with each technique. Among various baseflow separation approaches, digital filter methods have gained popularity due to their simplicity and effectiveness, use numerical algorithms to partition streamflow into its constituent components. However, selecting appropriate filter parameters is crucial for accurate results.

To enhance the robustness of baseflow analysis, it is advantageous to combine different segmentation methods. This can be achieved by integrating the strengths of individual techniques to compensate for their respective limitations. For instance, one could apply a digital filter method to obtain a preliminary separation of baseflow and then refine the results using a more physically-based approach, such as recession curve analysis. This hybrid strategy leverages the simplicity and computational efficiency of digital filters while incorporating the detailed insights provided by physical methods, especially during varying flow regimes. The combined approach not only ensures consistency across different flow conditions but also tailors the analysis to the unique hydrological characteristics of the study area.

**Author contribution statement:** Conceived and designed the experiments; Analyzed and interpreted the data; wrote the draft manuscript and manuscript editing: N.Y.N.

**Acknowledgements:** This work was supported by the Ministry of Science and Technology of Vietnam through the project No. ĐTDL.CN-06.23.

**Competing interest statement:** The authors declare no conflict of interest.

## References

1. Hayashi, M.; Rosenberry, D.O. Effects of ground water exchange on the hydrology and ecology of surface water. *Ground Water* **2002**, *40*(3), 309–316.
2. Eckhardt, K. How to construct recursive digital filters for baseflow separation. *Hydrol. Process.* **2005**, *19*(2), 507–515.

3. Tong, X.W.A.; Illman, Y.J.; Park, D.L.; Rudolph, S.J.; Berg. Significance of groundwater flow in hydrologic models, a model comparison study in a small watershed. Annual report submitted to the Global Water Futures Programme. 2021.
4. Brutsaert, W.; Nieber, J.L. Regionalized drought flow hydrographs from a mature glaciated plateau. *Water Resour. Res.* **1977**, *13*(3), 637–644.
5. Troch, P.A.; Berne, A.; Bogaart, P.; Harman, C.; Hilberts, A.G.J.; Lyon, S.W.; Paniconi, C.; Pauwels, V.R.N.; Rupp, D.E.; Selker, J.S.; Teuling, A.J.; Uijlenhoet, R.; Verhoest, N.E.C. The importance of hydraulic groundwater theory in catchment hydrology: The legacy of Wilfried Brutsaert and Jean-Yves Parlange. *Water Resour. Res.* **2013**, *49*(9), 5099–5116.
6. Liang, X.Y.; Zhan, H.B.; Zhang, Y.K.; Schilling, K. Base flow recession from unsaturated-saturated porous media considering lateral unsaturated discharge and aquifer compressibility. *Water Resour. Res.* **2017**, *53*, 7832–7852. <https://doi.org/10.1002/2017WR020938>.
7. Tallaksen, L.M. A review of baseflow recession analysis. *J. Hydrol.* **1995**, *165*, 349–370.
8. Hewlett, J.D.; Hibbert, A.R. Factors affecting the response of small watersheds to precipitation in humid areas. In: Sopper, W.E.; Lull, H.W. (Eds.), *Int. Symp. on Forest Hydrol.* Oxford. Pergamon, New York, 1967, pp. 275–290.
9. Murphy, R.; Graszkiwicz, Z.; Hill, P.; Neal, B.; Nathan, R.; Ladson, T. Australian rainfall and runoff revision project 7: Baseflow for Catchment Simulation, Stage 1 report, P7/S1/004. Engineers Australia, 2009, pp. 1–111. Available online: [https://arr.ga.gov.au/\\_\\_data/assets/pdf\\_file/0006/40497/ARR\\_Project\\_7\\_Stage1\\_report\\_Final.pdf](https://arr.ga.gov.au/__data/assets/pdf_file/0006/40497/ARR_Project_7_Stage1_report_Final.pdf).
10. Hall, F.R. Base flow recessions – A review. *Water Resour. Res.* **1968**, *4*(5), 973–983.
11. Chow, V.T.; Maidment, D.R.; Mays, L.W. *Applied Hydrology*. McGraw-Hill. 1988.
12. Nathan, R.J.; McMahon, T.A. Evaluation of automated techniques for base flow and recession analyses. *Water Resour. Res.* **1990**, *26*(7), 1465–1473.
13. Brodie, R.S.; Hostetler, S. A review of techniques for analysing baseflow from stream hydrographs. Proceedings of the NZHS-IAH-NZSSS Conference, 28 November - 2 December 2005. Auckland, New Zealand, 2005.
14. Institute of Hydrology. Low flow studies report No. 3: The estimation of low flow characteristics in rivers. Institute of Hydrology. 1980.
15. Sloto, R.A.; Crouse, M.Y. HYSEP: A computer program for streamflow hydrograph separation and analysis. US Geological Survey Water-Resources Investigations Report 96-4040. 1996.
16. Linsley, R.K.; Jr, M.A.K.; Paulhus, J.L.H. *Hydrology for Engineers*. McGraw-Hill, New York, 1982, pp. 212.
17. Available online: <https://www.hec.usace.army.mil/confluence/hmsdocs/hmstrm/transform/unit-hydrograph-basic-concepts>.
18. Thakur, P.K.; Nikam, B.R.; Garg, V. et al. Hydrological parameters estimation using remote sensing and GIS for Indian region: A review. *Proc. Natl. Acad. Sci., India, Sect. A Phys. Sci.* **2017**, *87*, 641–659. <https://doi.org/10.1007/s40010-017-0440-z>.
19. Birtles, A.B. Identification and separation of major baseflow components from a stream hydrograph. *Water Resour. Res.* **1978**, *14*(5), 791–803. <https://doi.org/10.1029/WR014i005p00791>.
20. Yu, X.; Schwartz, F.W. Use of environmental isotopes to estimate groundwater recharge. In *Isotope Tracers in Catchment Hydrology*, 1999, pp. 281–310.
21. Lyne, V.; Hollick, M. Stochastic time-variable rainfall-runoff modeling. *Hydrol. Sci. Bull.* **1979**, *24*(3), 355–372. doi:10.1080/02626667909491834.

22. Chapman, T.G.; Maxwell, A.I. A comparison of baseflow indices, which describe streamflow recession. *Hydrol. Sci. J.* **1996**, *41*(3), 399–412. doi:10.1080/02626669609491577.
23. Furey, P.R.; Gupta, H.V. A physically based filter for separating base flow from streamflow time series, *Water Resour. Res.* **2001**, *37*(11), 2709–2722. <https://doi.org/10.1029/2001WR000243>.
24. Tularam, G.A.; Ilahee, M. Baseflow separation using recursive digital filters: A case study in the Upper Essequibo River Basin, Guyana. *Hydrol. Processes* **2008**, *22*(25), 4920–4930. <https://doi.org/10.1002/hyp.7130>.
25. Dincer, T.; Payne, B.R.; Florkowski, T.; et al. Snowmelt runoff from measurements of tritium and oxygen 18. *Water Resour. Res.* **1970**, *6*, 110–124.
26. Wels, C.; Cornet, R.J.; LaZerte, B.D. Hydrograph separation: A comparison of geochemical and isotopic tracers. *J. Hydrol.* **1991**, *122*, 253–274.
27. Sharpe, W.E.; Kimmel, W.G.; Young, E.S.; et al. Insitu bio assays of fish mortality in two Pennsylvania Streams acidified by atmospheric deposition. *Northeast. Environ. Sci.* **1983**, *2*, 171–178.
28. Gagen, C.J.; Sharpe, W.E. Net sodium loss and mortality of three salmonid species exposed to a stream acidified by atmospheric deposition. *Bull. Environ. Contam. Toxicol.* **1987**, *39*, 7–14.
29. Bazemore, D.E.; Eshleman, K.N.; Hollenbeck, K.J. The role of soil water in stormflow generation in a forested head water catchments: Synthesis of natural tracer and hydro metric evidence. *J. Hydrol.* **1994**, *162*, 47–75.
30. Gonzales, A.L.; Nonner, J.; Heijkers, J.; Uhlenbrook, S. Comparison of different base flow separation methods in a lowland catchment. *Hydrol. Earth Syst. Sci.* **2009**, *13*, 2055–2068. <https://doi.org/10.5194/hess-13-2055-2009>.
31. Eckhardt, K.A. Comparison of baseflow indices, which were calculated with seven different baseflow separation methods. *J. Hydrol.* **2008**, *352*, 168–173.
32. Duncan, H.P. Baseflow separation - A practical approach. *J. Hydrol.* **2019**, *575*, 308–313.
33. Kissel, M.; Schmalz, B. Comparison of baseflow separation methods in the German low mountain range. *Water* **2020**, *12*, 1740. <https://doi.org/10.3390/w12061740>.
34. Arnold, J.G.; Allen, P.M. Automated methods for estimating baseflow and groundwater recharge from streamflow records. *J. Am. Water Resour. Assoc.* **1999**, *35*(2), 411–424.
35. Mau, Y.; Winter, T.C. Comparison of base-flow estimates using graphical and digital-filter-based separation methods. *Ground Water.* **1997**, *35*(3), 453–459.
36. Xie, Y.; Zhang, Y.; Wang, D. Comparative evaluation of baseflow separation methods in the contiguous United States. *J. Hydrol.* **2020**, *590*, 125431.
37. Sun, J.; Wang, X.; Shahid, S.; et al. An optimized baseflow separation method for assessment of seasonal and spatial variability of baseflow and the driving factors. *J. Geogr. Sci.* **2021**, *31*, 1873–1894. <https://doi.org/10.1007/s11442-021-1927-8>
38. Partington, D.; Brunner, P.; Simmons, C.T.; Werner, A.D.; Therrien, R.; Maier, H.R.; Dandy, G.C. Evaluation of outputs from automated baseflow separation methods against simulated baseflow from a physically based, surface water- groundwater flow model. *J. Hydrol.* **2012**, *458*, 28–39.
39. Rutledge, A.T. Computer programs for describing the recession of ground-water discharge and for estimating mean ground-water recharge and discharge from streamflow records: Update (No. 98). US Department of the Interior, US Geological Survey. 1998.
40. Aquanty Inc. HydroGeoSphere. A three-dimensional numerical model describing fully-integrated subsurface and surface flow and solute transport. Retrieved from

Waterloo, Ontario, Canada. 2018. Available online: <https://www.aquanty.com/hgs-download>.

41. Li, L.; Maier, H.R.; Partington, D.; Lambert, M.F.; Simmons, C.T. Performance Assessment and improvement of recursive digital baseflow filters for catchments with different physical characteristics and hydrological inputs. *Environ. Modell. Softw.* **2014**, *54*, 39–52.
42. Boughton, W.C. A hydrograph-based model for estimating the water yield of ungauged catchments. In: *Hydrology and Water Resources Symposium*. Institution of Engineers Australia, Newcastle, NSW, 1993, pp. 317–324.
43. Su, C.H.; Peterson, T.J.; Costelloe, J.F.; Western, A.W. A synthetic study to evaluate the utility of hydrological signatures for calibrating a base flow separation filter. *Water Resour. Res.* **2016**, *52*(8), 6526–6540.

*Research Article*

# Applying the variable infiltration capacity (VIC) model to reconstructing streamflow data in the Da River basin at Muong Te hydrological station

Khuong Van Hai<sup>1\*</sup>, Giang Nguyen Tien<sup>2</sup>, Do Thi Ngoc Bich<sup>3</sup>

<sup>1</sup> Center for Water Resources Software technology; khuongvanhai@gmail.com

<sup>2</sup> Faculty of Hydrology, Meteorology and Oceanography, University of Science, Vietnam National University, Hanoi; No. 334 Nguyen Trai Street, Thanh Xuan District, Hanoi, Viet Nam; nguyentiengiang@hus.edu.vn; giangnt@vnu.edu.vn

<sup>3</sup> Water Resources Institute, Ha Noi, Viet Nam; No. 8 Phao Dai Lang, Lang Thuong, Dong Da, Ha Noi, Viet Nam; bichdam555@gmail.com; dtnbich@monre.gov.vn

\*Corresponding author: khuongvanhai@gmail.com; Tel.: +84-974183835

Received: 7 May 2024; Accepted: 5 June 2024; Published: 25 September 2024

**Abstract:** Reconstruction of streamflow in transnational river basins is of great significance in water resource planning and management in Vietnam. Among the ten biggest river basins (each having a total basin area of greater than 10,000 km<sup>2</sup>) there are eight transnational river basins, and Vietnam is located downstream in the five basins of those eight. These include the Mekong River with 92% of the area belonging to foreign countries; the Red River with 51% located abroad, mainly China; the Dong Nai River with 17% belonging to Cambodia; the Ma River with nearly 38% belongs to Laos and the Ca River with 35% belongs to Laos. This study uses numerical modeling methods to reconstruct the streamflow from China to Vietnam in the Da River basin at Muong Te hydrological station. The VIC model was applied with daily climate data (rain, wind speed, maximum and minimum temperature) from 1981 to 2020 to reconstruct streamflow at Muong Te station in the Da River basin. Combining the VIC Model and the Shuffled Complex Evolution method to determine the most suitable set of parameters for the Da River basin creates a powerful tool for studying hydrological processes on river basins. Research results also show that the streamflow reconstruction for the period before 2008 when the upstream reservoirs were not yet in operation is highly reliable.

**Keywords:** VIC; Da river; Muong Te; SCE.

---

## 1. Introduction

Streamflow reconstruction is an important issue in hydrology, especially in data-deficient river basins that lack/have no gauging stations. Data-deficient basins, data-scarce basins and basins without gauging stations are basins with limited meteorological and hydrological data [1]. Therefore, studies on water resources and flood and drought forecasts in such basins often have low reliability. The International Association of Hydrological Sciences (IAHS) in the years 2003-2012 initiated research related to hydrological forecasting for basins lacking gauging stations (prediction in ungauged basins - PUB) considering uncertain factors [1]. Most of the studies related to PUB were carried out after 2003. An example of previous studies [2], performed estimation of hydrological model parameters based on classification basins according to similarities in basin characteristics and geomorphological topography, instead of traditionally used methods, such as regression equations.

The small number of hydrological gauging stations creates challenges related to forecasting inaccuracy of streamflows. Regardless of the forecasting method used, streamflow forecast results need to be verified against observed/gauge data [3]. Therefore, to be able to identify accurate forecast results for locations without gauging stations, gauge data at neighboring locations are often required to compare with simulation results [4]. One of the commonly used approaches recently is to use data in many neighboring basins combined with regionalization methods to forecast runoff for data-deficient basins [5]. The effectiveness of this approach has been demonstrated when applying streamflow forecasts to basins lacking gauge data using large datasets such as CAMELS-US with 671 basins in the United States [6] or CAMELS GB with 671 catchments in the UK [7]. Regionalization methods can be used to interpolate the hydrological characteristics of data-deficient catchments based on the characteristics (geology, geomorphology, spatial meteorology) of neighboring catchments [8].

The VIC model [8–10] is a macroscale hydrological model that addresses the full energy and water balance, originally developed by Xu Liang at the University of Washington. VIC is a research model and in many different forms, it has been applied to most major river basins in the world, as well as globally. This is a grid-based semi-distributed hydrological model that quantifies the main hydrometeorological processes occurring at the atmospheric land surface. Typically, mesh resolution ranges from 1/8 to 2 degrees. The VIC model was first described as a single soil layer model [11]. The single-layer soil model requires three parameters: permeability parameter, evaporation parameter, and baseflow recession coefficient. In 1994, Liang et al generalized the two-layer VIC model (VIC-2L) to include multiple spatially varying soil and vegetation layers and evaporation within a single grid cell. In VIC-2L, infiltration, drainage from the topsoil to the subsoil, and surface and subsurface runoff are calculated for each vegetation cover (in addition to the statistical parameter of heterogeneity) of infiltration and flow processes in a vegetated cover existing in the original VIC model). VIC-2L was later modified to allow moisture diffusion between soil layers, and there was an additional 10cm thin layer of soil on top of the previous topsoil layer. In this way, the three-layer VIC model (VIC-3L) [9, 11–14] was created and the VIC-3L frame has been used since then. The model now allows for more than three soil layers if desired. Such a model was used in this study.

The issue of monitoring cross-border water resources has become increasingly challenging in recent years, as water resources become scarcer due to the need to exploit them to serve socio-economic goals within each country sharing the river basin. The Da river plays a vital role in Vietnam's socio-economic development and water-food-energy security nexus. It houses three of the largest reservoirs in the country - Lai Chau, Son La, and Hoa Binh - which provide ample water supply for the Red River delta and Hanoi, the capital and the economic and political center of Vietnam. Monitoring streamflow from abroad into Vietnam within the Da River basin faces several difficulties due to the current flow data measurement practice that relies primarily on technology dating back to the late 20th century. Additionally, the manual methods used for data collection require significant human resources, infrastructure, and investment in monitoring equipment. The situation is further compounded at the Da river's border with China, where monitoring and measuring streamflow is even more challenging, with most of the streamflow remaining unmeasured. While Ka Lang water resources station, which was built in 2016, uses automatic technology to measure flow, it is currently inactive. The Keng Mo station has been measuring and collecting flow data since 2020, but as it is a station built and managed by EVN, it presents difficulties in terms of accessibility, and the observed dataset is not long enough. Moreover, there is currently no discharge gauging station on the mainstream of the Da river located upstream of the Lai Chau hydropower plant to monitor streamflow timeseries of sufficient length. Therefore, within the scope of this article, a modeling method has been applied to

restore the streamflow at the Muong Te hydrological station, result of restore the streamflow supports effective management of the amount of water flowing into Vietnam from the up basin of the Da River through the country border.

## 2. Materials and Methods

### 2.1. Description of the study area

The Da River originates in Yunnan, one of China’s southern provinces, and flows into the Red River delta in Vietnam, where it merges with two other tributaries, the Lo River and the Thao River (Figure 1). The Red River then continues to Hanoi, the capital of Vietnam,

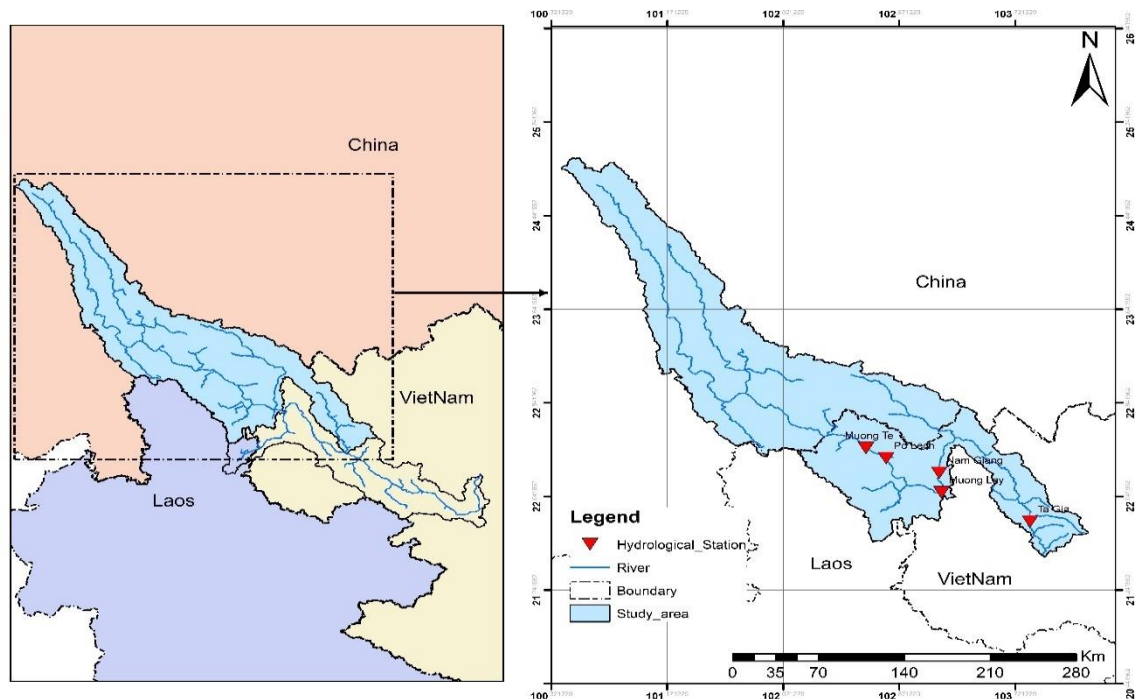


**Figure 1.** Map of the study area.

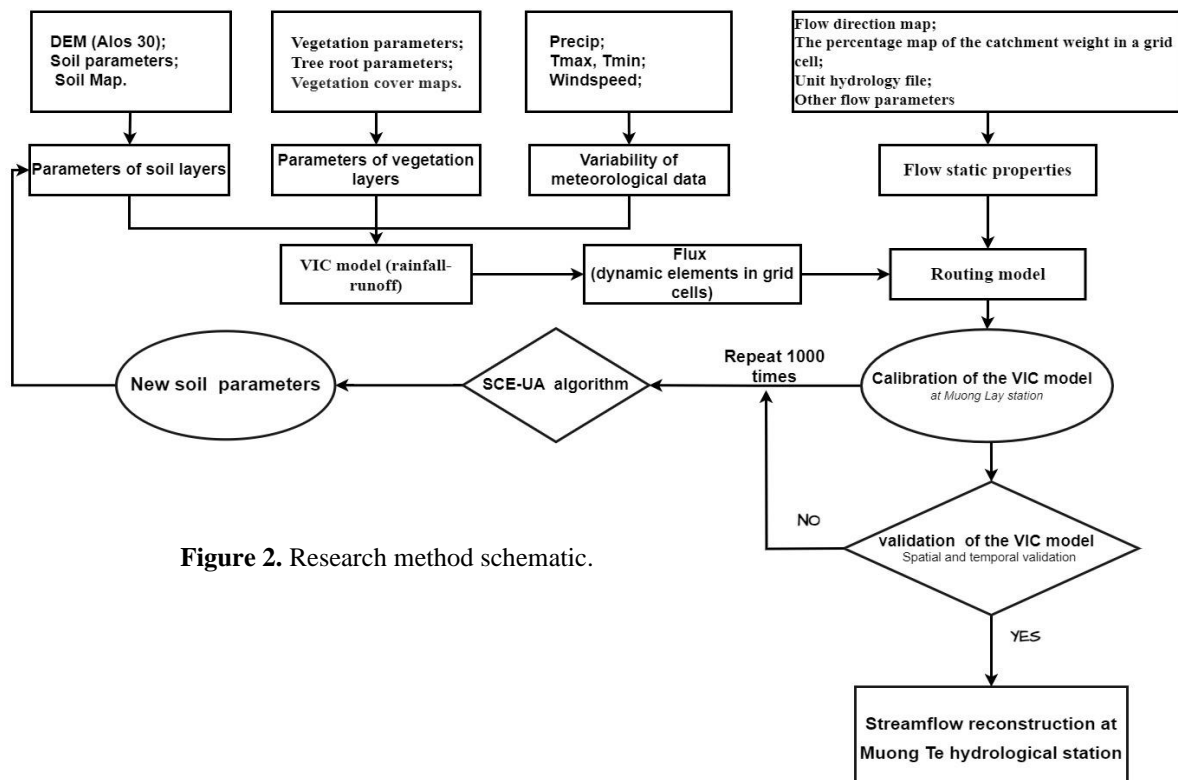


**Figure 2.** Research method schematic.



before flowing southeast to the East Sea. Numerous human interventions occur in and around this river without proper assessment or monitoring. Changes in land use as well as reservoir construction have a significant impact on this catchment area. The Da River generates substantial hydroelectric power, with dozens of dams in Yunnan and three large hydroelectric plants in Vietnam (EVN). However, the operating rules of the upstream dams are not publicly available. While there are hydrological and meteorological gauging stations in both country parts of the Da River catchment, little data from these stations is shared. A hydrological model has been used in this study to reconstruct the streamflow time series in the upstream part of the basin in Vietnam’s territory.

## 2.2. VIC model

### 2.2.1. VIC model overview

Before intervening in a water system, it is crucial to model the system to evaluate potential impacts. This process, which involves modeling a catchment’s physical characteristics and its rainfall-runoff processes, is referred to as hydrological modeling [15]. In this study, the VIC model will be used to simulate the Da River basin for several reasons:

(1) The VIC model is fully distributed and physically based, taking into account the spatial variability of inputs in great detail.

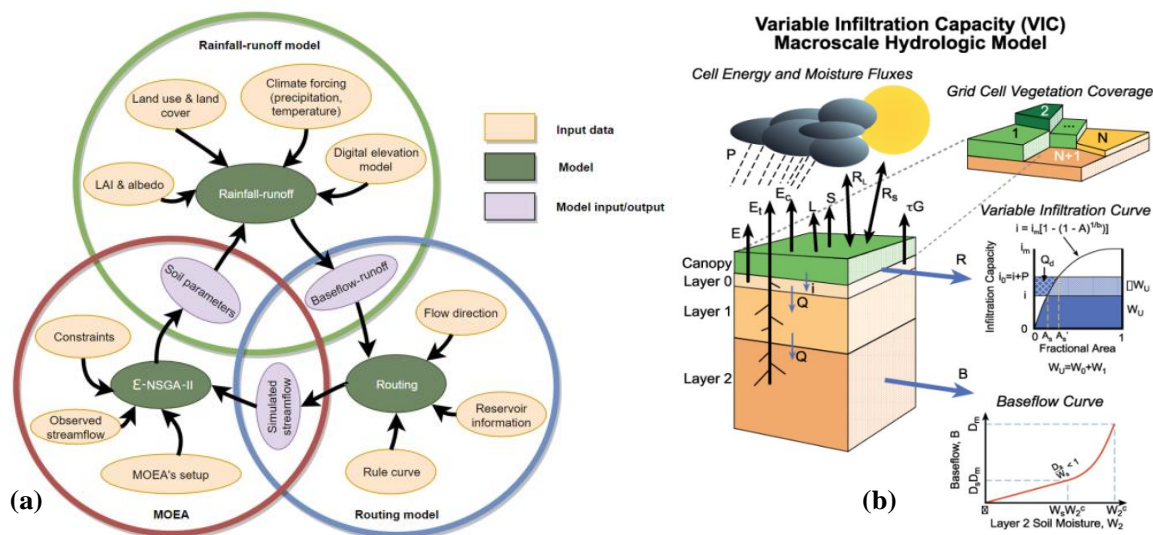


**Figure 3.** (a) Schematic overview of the VIC-model framework [16]; (b) Schematic overview of the mechanics behind the rainfall-runoff model.

(<https://www.hydro.washington.edu/Lettenmaier/Models/VIC/>).

(2) The VIC model is a hydrological land surface model, which means it employs quantitative methods to simulate the exchange of water, energy, and momentum fluxes between the land surface and the atmosphere.

(3) Human interventions, such as reservoirs and changes in land use and land cover, can also be simulated.

The VIC hydrological model is typically implemented using a framework consisting of three components, as illustrated in Figure 3a [17]. The rainfall-runoff model [18] serves as the foundation for simulating interactions between the atmosphere, land, and water flow. The mechanics of this part of the model are shown in Figure 3b. It utilizes climate forcings and the area's physical properties as inputs, producing gridded baseflow and runoff as outputs. The routing model [19] is performed separately and accumulates the gridded baseflow and runoff to determine streamflow at a selected outlet. This study utilizes the SCE-UA

optimization algorithm instead of the NSGA multi-objective genetic algorithm for model calibration as depicted in Figure 3a [20].

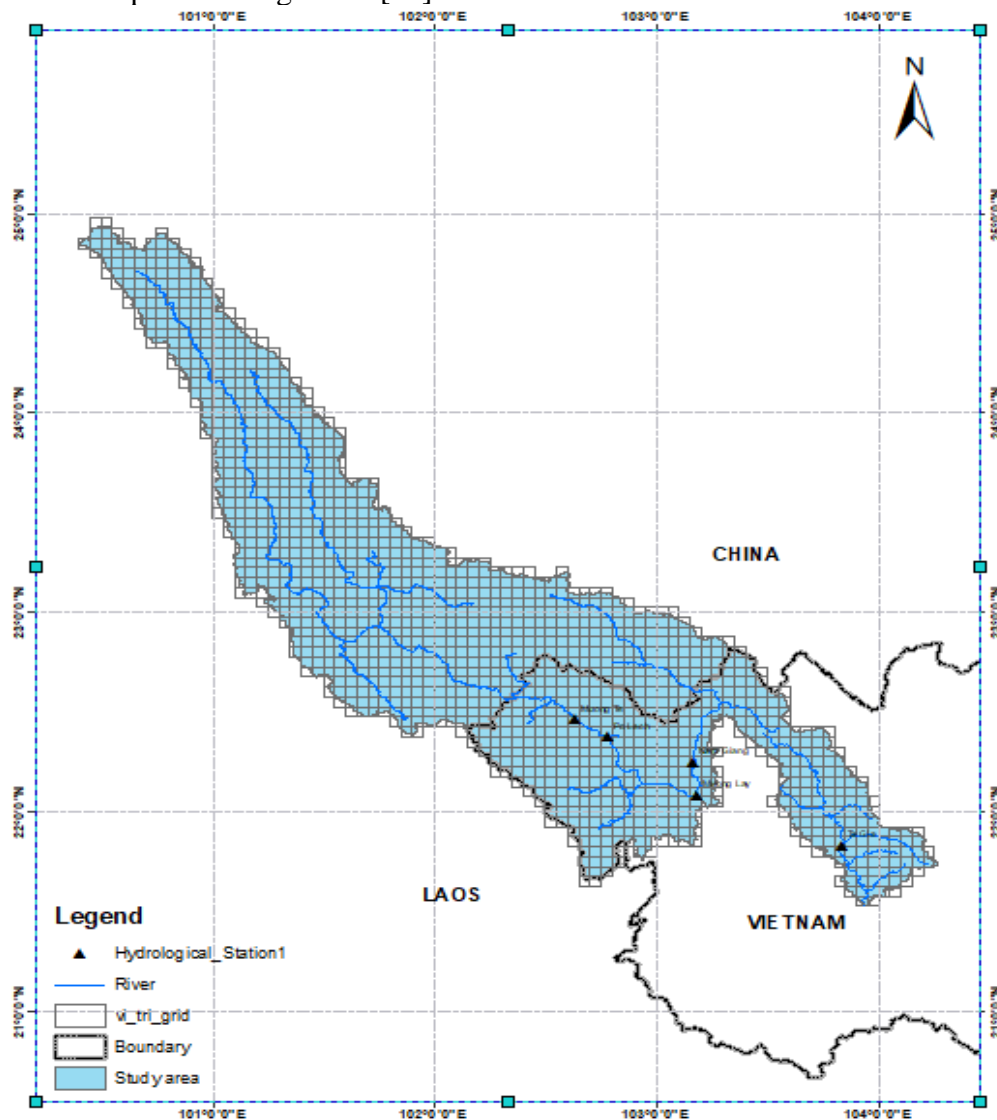


**Figure 4.** Set up VIC model for Da River.

### 2.2.2. Set up of the VIC model for the Da River basin

Simulation domain: The modeled Da River basin is divided into two regions including: Region 1 from upstream to the Vietnam - China border to Muong Lay station (Lai Chau Province).

Region 2 is the Nam Mu River basin containing two lakes, Ban Chat and Hoi Quang.

Simulation grid: The Da River basin is digitized into the VIC model with 3 soil layers, with a resolution of 0.05 degrees, the entire study area is divided into 16,146 points (78×69), including 4,134 simulation points (Figure 4).

### 2.3. Data collection

In this study, land use and land cover maps are employed, along with various vegetation properties such as LAI, albedo, and global and regional meteorological forcing time series. Additionally, a digital elevation model, flow direction map, flow characteristics, soil map with soil properties, and observed streamflow time series are utilized. To provide a clear overview of the sources for these datasets, Table 1 lists the datasets used, and a short description for each of these is given in the following subsections.

**Table 1.** Overview of the used datasets and their sources.

Datasets	Period	Purpose	Source
Station streamflow Vietnam	1981-2020	Discharge time series	Vietnam Meteorological and Hydrological Administration
Grid precipitation Vietnam (VnGP)	1981-2020	VIC model input	The Vietnam Gridded Precipitation (VnGP) Dataset: Construction and Validation [18]
Grid precipitation China (CHM)	1981-2020	VIC model input	The China Hydro-Meteorology dataset (Beijing Normal University) [19]
Grid wind speed and min/max temperature	1981-2020	VIC model input	ECMWF - EU [20]
Digital Elevation Model (DEM)	-	Set up the VIC model	ALOS30 [21]
Soil map & Soil properties	-	Set up the VIC model	FAO - Unesco, "Soil map of the world" [22]
Land Use & Land Cover maps	1992-2020	Set up the VIC model	Land Cover CCI Product User Guide Version 2 [23]

### 2.3.1. Meteorological forcing data files

The VIC model is capable of processing either daily (precipitation,  $T_{max}$ ,  $T_{min}$ , windspeed) or sub-daily meteorological data inputs, or a combination of both. VIC offers the flexibility of utilizing different variables and variable combinations as per the user's requirements. The global parameter file must contain a comprehensive description of the contents and formats of the meteorological data files.

### 2.3.2. Soil parameter file

The soil parameters for the VIC model are provided in a single ASCII file, where each row represents a unique grid cell. The fields in the file contain different parameter values for each cell. The soil parameter file serves three primary purposes: Firstly, it assigns a unique cell ID number to each grid cell, which acts as a database key to link the cell to its parameters in other parameter files. Secondly, it defines the soil parameters for each grid cell along with the geographic information such as the latitude and longitude of the grid cell center. Lastly, it defines the initial soil moisture conditions for use in the absence of an initial state file (Figure 5a).

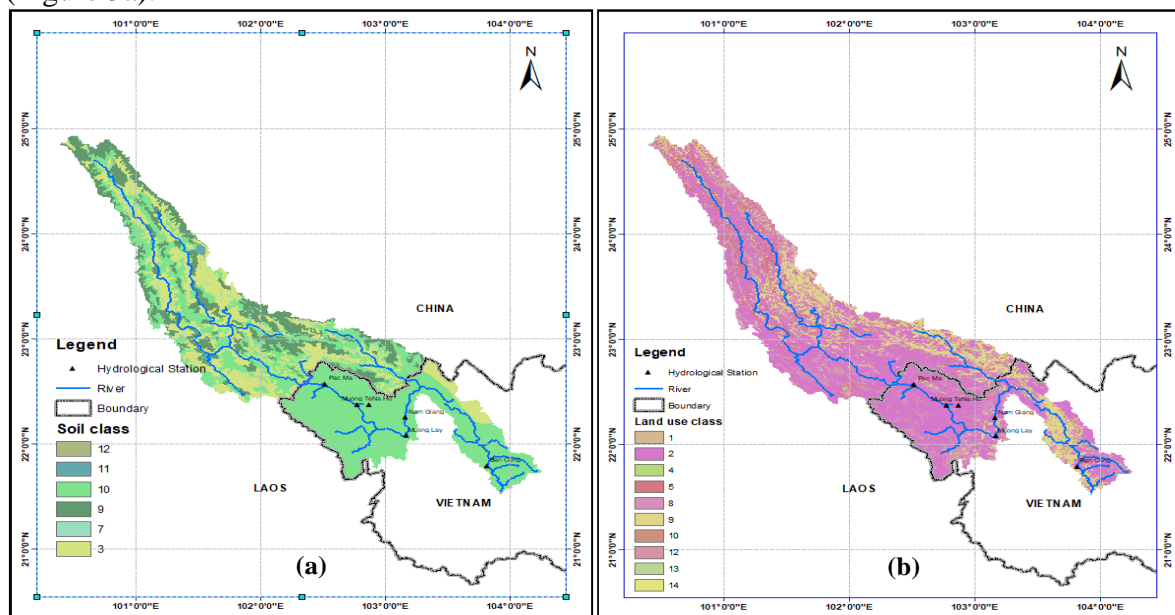


**Figure 5.** (a) Map of soil properties, (b) Land use and land cover maps.

### 2.3.3. Vegetation parameters and vegetation library

The vegetation parameters and vegetation library provide pertinent information regarding the number of vegetation types present in each grid cell, their partial coverage, and the required vegetation parameters for each vegetation type utilized in the VIC model. This information is presented in a columnar format as an ASCII file. Each grid cell is represented by a separate row, with each field containing a distinct parameter value.

### 2.3.4. Flow Direction

The flow direction file is a critical component of the routing model used in hydrological studies to establish connectivity between individual grid cells generated by the VIC model. The flow direction file provides header information to the model that knows the lower left latitude and longitude, the number of rows and columns, and grid cell resolution. Each grid cell in the file is assigned a number that represents the flow direction in the river and stream network.

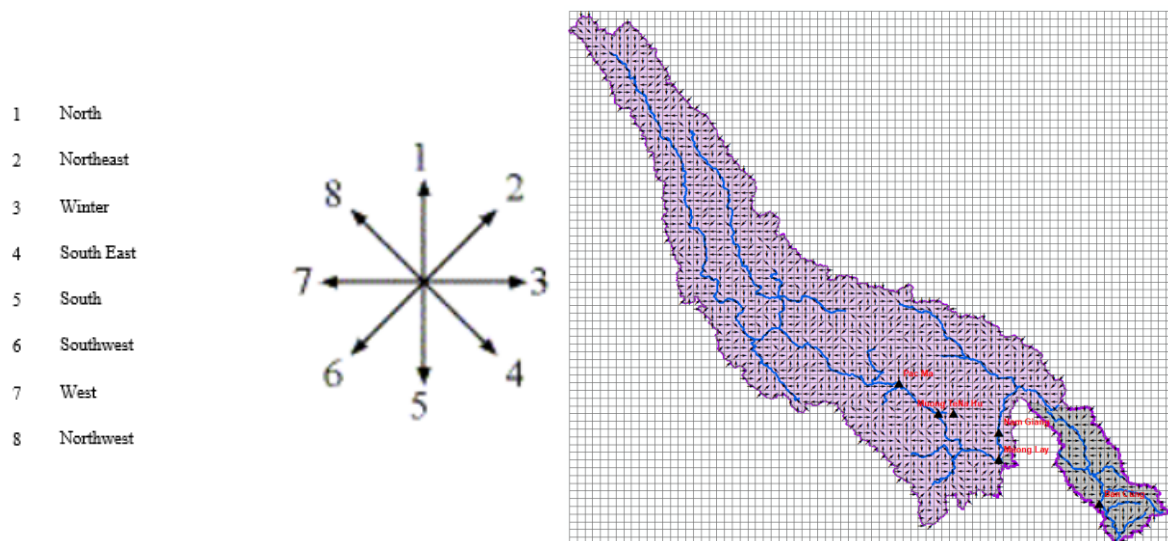


**Figure 6.** The flow direction map in the Da River basin.

## 3. Results and discussion

### 3.1. Calibration and validation of the VIC model

#### 3.1.1. Calibration of the VIC model

The determination of six soil parameters (bin, Ds, Dmax, Ws, D2, D3) is a challenging task, given their conceptual nature and the lack of observable, physical quantities [24, 25].

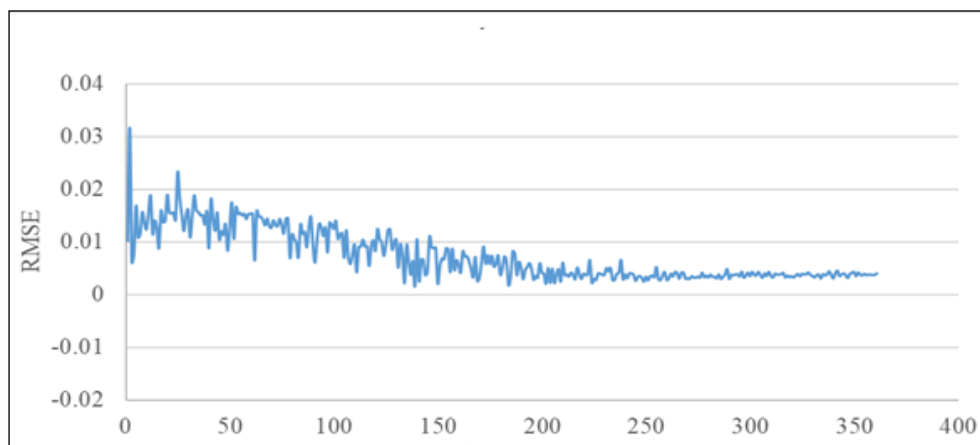


**Figure 7.** RMSE index convergence process using the SCE-UA algorithm (unit run-off is mm).

To address this issue, a calibration procedure was developed that utilizes an autocalibration script and the Shuffled Complex Evolution method, which was chosen for its ability to identify global optima with the right algorithmic parameters [26]. The calibration framework follows the VIC hydrological model [27], except for the parameter generation algorithm shown in Figure 2. The autocalibration script was run using a spatial resolution of 0.05°, which was a suitable resolution to mimic the Da River basin. Upon obtaining the optimal parameter set, the performance of the model was assessed using key performance indicators, specifically the NSE, BIAS, and RMSE.

The calibration of the VIC hydrological model employed the RMSE objective function to optimize six parameters, which were selected based on the RMSE index between observed discharge and simulated discharge at Muong Lay station during the years 1981-1995. The Shuffled Complex Evolution method was initially set up with 1000 iterations. After eliminating local disturbances, the RMSE indexes displayed an evolution of 380 RMSE indexes, showing the convergence of the simulated data series approaching the actual measured data series asymptotically. The convergence process of the objective function is illustrated in Figure 7. The results of the calibration process are provided in Table 2 and Figure 8.

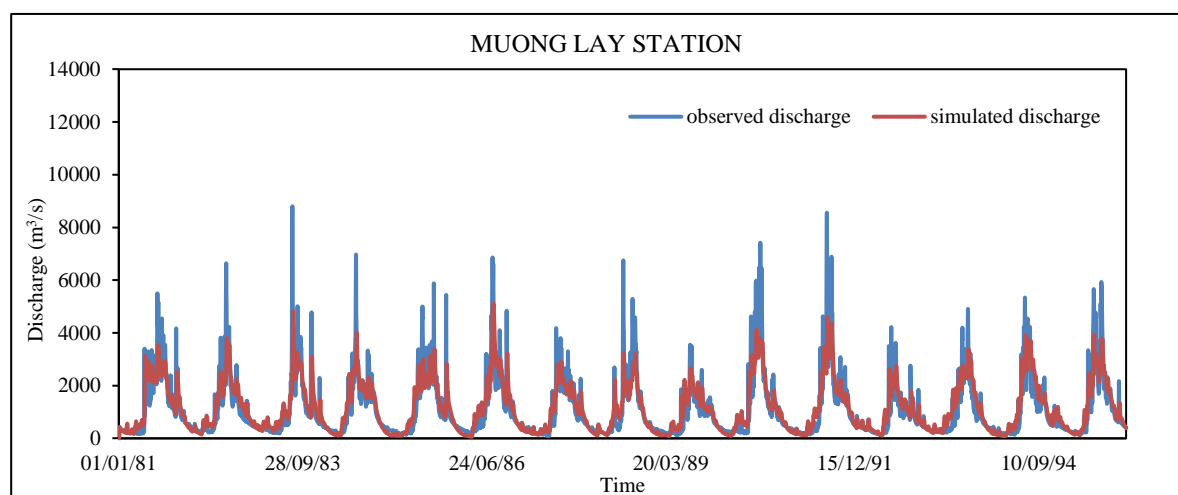


**Figure 8.** Simulated and observed daily discharge at Muong Lay station in the calibration period 1981-1995.

**Table 2.** Results of VIC model calibration of NSE, R<sup>2</sup>, RMSE, BIAS index.

Hydrology stations	NSE	R <sup>2</sup>	RMSE	BIAS
Muong Lay	0.78	0.86	444.3	114.9

The results of calibrating the VIC model show that the simulated discharge at Muong Lay station in the Da River basin is relatively consistent with the actual observed value, the reliability according to the NSE index is 0.78, the correlation coefficient is 0.86; the BIAS index is 114.9. The results of the adjusted simulation show that the VIC model parameters after adjustment are in close agreement with reality, which also means that the parameters after adjustment have relatively appropriately reflected the observed discharge from 1981-1995 in the Da River basin.

**Table 3.** VIC model calibration parameters.

No	Parameter	After calibration	Calibration range
1	bin	0.3151	0.002 - 0.495
2	Ds	0.7065	0.019 - 0.875
3	Dsmax	27.1525	2.653 - 29.983
4	Ws	0.7170	0.1 - 0.984
5	D <sub>2</sub>	0.3242	0.3 - 1.5
6	D <sub>3</sub>	1.4995	0.3 - 1.5

### 3.1.2. Spatially validation of the VIC model

Upon completion of the calibration process, it is imperative to verify the stability and suitability of the parameter set as outlined in Table 3. This study conducted an independent spatial validation at Nam Giang station during the years 1981-1995. The results are shown in Figure 9a and Table 4.

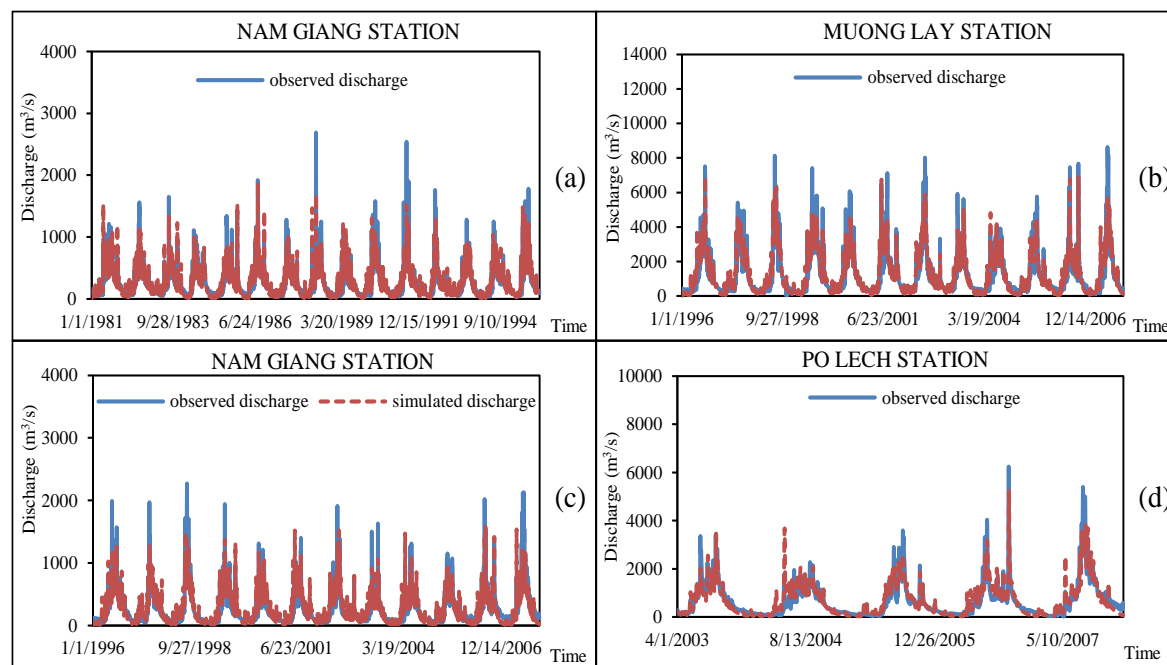


**Figure 9.** Simulated and observed discharge timeseries at: (a) Nam Giang station in the period 1981-1995; (b) Muong Lay station in the period 1996-2007; (c) Nam Giang station in the period 1996-2007; (d) Po Lech station in the period 2003-2007.

**Table 4.** Spatial independent validation results of NSE,  $R^2$ , RMSE, BIAS index.

Hydrology stations	NSE	$R^2$	RMSE	BIAS
Nam Giang	0.74	0.74	136.5	-8.9

After performing calibration and spatial validation on the VIC model, it was found that the simulated streamflow value at the Nam Giang station on the Da River basin is consistent with the observed value. The model’s reliability, as determined by the NSE index, is good at 0.74, while the correlation coefficient is also 0.74. However, the BIAS index is negative at -8.9.

Based on the results of spatially independent validation, it has been found that the VIC model parameters are in close agreement with reality. This also indicates that the calibration parameters reflect the relatively well-observed discharge from 1981 to 1995 in the Da River sub-basins. Therefore, the set of parameters mentioned in Table 3 is deemed qualified for conducting spatial and temporal independent validation. This will confirm the stability of the VIC model parameters for the Da River basin.

### 3.2. Spatial and temporal validation of the VIC model

The study aimed to validate selected model parameters using discharge observations in the Da River basin at three stations - Muong Lay, Nam Giang, and Po Lech. The six parameters selected for validation are listed in Table 3 for the three stations - Muong Lay, Nam Giang (1996-2007), and Po Lech (2003-2007). The results of spatial and temporal independent validation are presented in Figure 9b-9d and Table 5.

**Table 5.** Spatial and temporal independent validation results of NSE, R<sup>2</sup>, RMSE, BIAS index.

Hydrology stations	NSE	R <sup>2</sup>	RMSE	BIAS
Nam Giang	0.78	0.8	134.6	-8.7
Muong Lay	0.85	0.86	488.5	33.0
Po Lech	0.81	0.81	323	8.0

The VIC model’s spatial and temporal independent validation results indicate that the discharge values at certain locations in the Da River basin are consistent with the actual observed values. At the Nam Giang station, the NSE index is 0.78, which is a good grade, the correlation coefficient is 0.8, and the BIAS index is -8.7. At the Muong Lay station, the NSE index is 0.85, which is a good grade, the correlation coefficient is 0.86, and the BIAS index is 33.0. At the Po Lech station, the NSE index is 0.81, which is a good grade, the correlation coefficient is 0.81, and the BIAS index is 8.0.

The validation results indicate that the model parameters are consistent with reality, which implies that the validated parameters reflect the actual discharge from 1996 to 2007 in the Da River basin. Therefore, the parameters in Table 3 are qualified to simulate and reconstruct the flow from China to Vietnam on the Da River basin.

### 3.3. Streamflow reconstruction at Muong Te hydrological station

The reconstruction of streamflow data at Muong Te station for the period before and after large upstream reservoirs came into operation from 1981 to 2020 was done using the VIC model and the set of parameters selected in Table 3. The results of this simulation are presented in Figure 10.

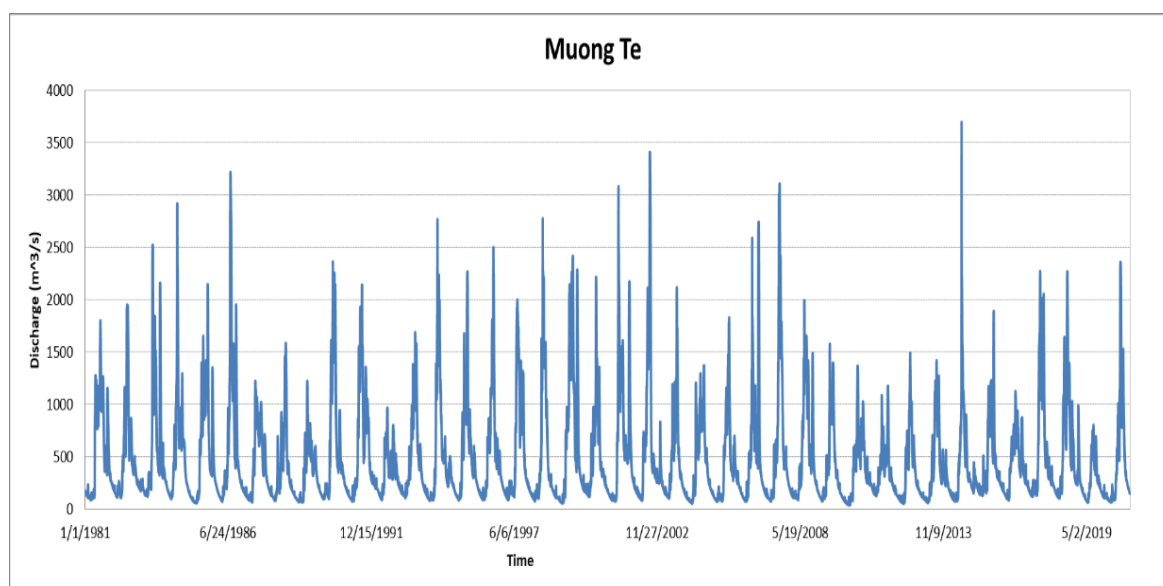


**Figure 2.** Results of streamflow reconstruction at Muong Te station in the period (1981-2020).

The results of streamflow reconstruction when considering correlation with the observed water level at Muong Te Station have a large decline in the period after 2007, Figure 11. For the period before 2008, the correlation coefficient between reconstructed streamflow and the actual water level observed is 0.78. In the period from 2008 to 2015, the correlation coefficient between the streamflow reconstruction and the actual observed water level decreased to 0.73. This result shows that the set of parameters in Table 3 is suitable for the reconstructed natural flow in the Da River basin. This recovery data plays an important role in researching and designing regulation reservoirs in the Da River basin and assessing the effects of water regulation reservoirs in Vietnam and China.

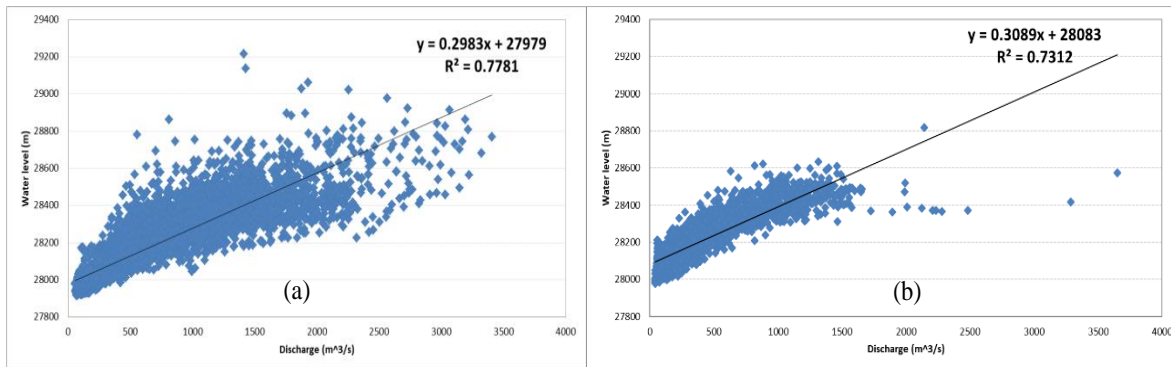


**Figure 3.** The correlation coefficient between streamflow reconstruction and actual water level observed at Muong Te station in the period before and after 2007.

### 3.4. Discussion

Da River and Red River are important in Vietnam's water resource security. Thus, there have been many studies applying simulation models on Da River and the Red River basins. The study [28] used the HEC-HMS model to simulate flow from 2003 to 2019, and simulation results were evaluated through 2 gauging stations (Ta Bu and Muong Lay) with Nash index ranging from 0.711 to 0.818; Study [29, 30] simulated daily streamflow on the Red River from 2005 to 2014, the simulation results were evaluated through 4 hydrological stations (Lao Cai, Yen Bai, Son Tay, and Hanoi) with Nash index ranging from 0.113 to 0.487; Yungang Li and his colleagues simulated the daily flow of the mainstream of the Red River on the Chinese side from 1961 to 2012. The simulation results were evaluated with the Nash index ranging from 0.85 to 0.89 [31]. In this study, the authors synchronized real observed rain data from China and Vietnam as input to the VIC model. To improve the simulation quality, the perturbed complex evolutionary algorithm [20, 32] was applied to calibrate the model's parameter set. The daily streamflow simulation results were evaluated with the Nash index ranging from 0.74 to 0.85 (Section 3.2), which shows a remarkable improvement compared with the previous studies conducted in Vietnam, and almost as good as the study conducted in China for the Red River. It is worth noting that Yungang Li and his colleagues used the observed meteorological and hydrological data, whereas this study utilized only measured discharge.

### 4. Conclusion

The monitoring of the discharge of water from China to Vietnam in the upstream area of Da River is challenging due to technological, economic, and natural conditions. As a result, discharge data is often incomplete or non-existent, making it difficult to plan and manage water resources in the basin. To address this, the VIC land surface hydrological model was used to simulate flow in the Da River basin by selecting appropriate parameters and data. The VIC model was combined with the Shuffled Complex Evolution method to determine the best set of parameters for the basin, creating a powerful tool for studying hydrological processes in river basins.

The research results showed that the streamflow at Muong Te station in the Da River basin between 1981 and 2020 was accurately restored using the VIC model. The streamflow reconstruction was exceptionally reliable for the period before 2008 when the upstream reservoirs were not yet put in operation. However, after 2008, the streamflow of the Da River was influenced by the regulation activities of flow-regulating reservoirs in China. Therefore, in-depth research is required to reconstruct the streamflow time series during this period by considering the hydrological processes in the basin and the regulation of reservoirs.



**Author contribution statement:** Designed the study conception: K.V.H.; collected data: G.N.T., K.V.H.; developed the theoretical research: G.N.T., K.V.H.; processed the data and performed the simulations: K.V.H.; analyzed the data: K.V.H.; contributed largely to revising the final manuscript: G.N.T., K.V.H., D.T.N.B.

**Acknowledgments:** This study is supported by project No. ĐTĐL.CN–06/23 of the 562–programme funded by Vietnam Ministry of Science and Technology

**Competing interest statement:** The authors declare no conflict of interest.

## References

1. Meko, D.M.; Woodhouse, C.A. Application of streamflow reconstruction to water resources management. In: Hughes, M.; Swetnam, T.; Diaz, H. (eds) *Dendroclimatology. Developments in Paleoenvironmental Research*, vol 11. Springer, Dordrecht. 2011, pp. 231–261. [https://doi.org/10.1007/978-1-4020-5725-0\\_8](https://doi.org/10.1007/978-1-4020-5725-0_8).
2. Ibrahim, A.B.; Cordery, I.A.N. Estimation of recharge and runoff volumes from ungauged catchments in eastern Australia. *Hydrol. Sci. J.* **1995**, *40*(4), 499–515. <https://doi.org/10.1080/02626669509491435>.
3. Moradkhani, H.; Sorooshian, S. General review of rainfall-runoff modeling: model calibration, data assimilation, and uncertainty analysis. *Hydrol. Model. Water Cycle* **2008**, 1–24. [https://doi.org/10.1007/978-3-540-77843-1\\_1](https://doi.org/10.1007/978-3-540-77843-1_1).
4. Samuel, R.D.; Tenenbaum, G. How do athletes perceive and respond to change-events: An exploratory measurement tool. *Psychol. Sport Exerc.* **2011**, *12*(4), 392–406. <https://doi.org/10.1016/j.psychsport.2011.03.002>.
5. Kratzert, F.; Klotz, D.; Shalev, G.; Klambauer, G.; Hochreiter, S.; Nearing, G. Towards learning universal, regional, and local hydrological behaviors via machine learning applied to large-sample datasets. *Hydrol. Earth Syst. Sci.* **2019**, *23*(12), 5089–5110. <https://doi.org/10.5194/hess-23-5089-2019>.
6. Addor, N.; Newman, A.J.; Mizukami, N.; Clark, M.P. The CAMELS data set: catchment attributes and meteorology for large-sample studies. *Hydrol. Earth Syst. Sci.* **2017**, *21*(10), 5293–5313. <https://doi.org/10.5194/hess-21-5293-2017>.
7. Coxon, G.; Addor, N.; Bloomfield, J.P.; Freer, J.; Fry, M.; Hannaford, J.; Howden, N.J.K.; Lane, R.; Lewis, M.; Robinson, E.L.; Wagener, T.; Woods, R. CAMELS-GB: hydrometeorological time series and landscape attributes for 671 catchments in Great Britain. *Earth Syst. Sci. Data* **2020**, *12*(4), 2459–2483. <https://doi.org/10.5194/essd-12-2459-2020>.
8. Göttinger, J.; Bárdossy, A. Comparison of four regionalisation methods for a distributed hydrological model. *J. Hydrol.* **2007**, *333*(2), 374–384. <https://doi.org/10.1016/j.jhydrol.2006.09.008>.
9. Liang, X.; Wood, E.F.; Lettenmaier, D.P. Surface soil moisture parameterization of the VIC-2L model: Evaluation and modification. *Glob. Planet. Change* **1996**, *13*(1–4), 195–206. [https://doi.org/10.1016/0921-8181\(95\)00046-1](https://doi.org/10.1016/0921-8181(95)00046-1).
10. Hamman, J.J.; Nijssen, B.; Bohn, T.J.; Gergel, D.R.; Mao, Y. The variable infiltration capacity model version 5 (VIC-5): Infrastructure improvements for new applications and reproducibility. *Geosci. Model Dev.* **2018**, *11*(8), 3481–3496. <https://doi.org/10.5194/GMD-11-3481-2018>.
11. Liang, X.; Wood, E.F.; Lettenmaier, D.P. Surface soil moisture parameterization of the VIC-2L model: Evaluation and modification. *Glob. Planet. Change* **1996**, *13*(1–4), 195–206. [https://doi.org/10.1016/0921-8181\(95\)00046-1](https://doi.org/10.1016/0921-8181(95)00046-1).
12. Zhao, Q.; Ye, B.; Ding, Y.; Zhang, S.; Yi, S.; Wang, J.; Shangguan, D.; Zhao, C.; Han, H. Coupling a glacier melt model to the variable infiltration capacity (VIC) model for hydrological modeling in north-western China. *Environ. Earth Sci.* **2013**,

- 68, 87–101. <https://doi.org/10.1007/s12665-012-1718-8>.
13. Wang, G.Q.; Zhang, J.Y.; Jin, J.L.; Pagano, T.C.; Calow, R.; Bao, Z.X.; Liu, C.S.; Liu, Y.L.; Yan, X.L. Assessing water resources in China using PRECIS projections and a VIC model. *Hydrol. Earth Syst. Sci.* **2012**, *16*, 231–240. <https://doi.org/10.5194/hess-16-231-2012>.
  14. Gao, H.; Tang, Q.; Shi, X.; Zhu, C.; Bohn, T.; Su, F.; Sheffield, J.; Pan, M.; Lettenmaier, D.; Wood, E.F. Water budget record from variable infiltration capacity (VIC) model. 2010, pp. 120–173. Available online: [https://eprints.lancs.ac.uk/id/eprint/89407/1/Gao\\_et\\_al\\_VIC\\_2014.pdf](https://eprints.lancs.ac.uk/id/eprint/89407/1/Gao_et_al_VIC_2014.pdf) (Accessed 20 April 2023).
  15. Gou, J.; Miao, C.; Duan, Q.; Tang, Q.; Di, Z.; Liao, W.; Wu, J.; Zhou, R. Sensitivity analysis-based automatic parameter calibration of the VIC model for streamflow simulations over China. *Water Resour. Res.* **2020**, *56*(1), e2019WR025968. <https://doi.org/10.1029/2019WR025968>.
  16. Dang, T.D.; Chowdhury, A.F.M.K.; Galelli, S. On the representation of water reservoir storage and operations in large-scale hydrological models: Implications on model parameterization and climate change impact assessments. *Hydrol. Earth Syst. Sci.* **2020**, *24*(1), 397–416. <https://doi.org/10.5194/HESS-24-397-2020>.
  17. Anees, M.T.; Abdullah, K.; Nawawi, M.N.M.; Ab Rahman, N.N.N.; Piah, A.R.Mt.; Zakaria, N.A.; Syakir, M.I.; Omar, A.K.M. Numerical modeling techniques for flood analysis. *J. African Earth Sci.* **2016**, *124*, 478–486. <https://doi.org/10.1016/J.JAFREARSCI.2016.10.001>.
  18. Nguyen-Xuan, T.; Ngo-Duc, T.; Kamimera, H.; Trinh-Tuan, L.; Matsumoto, J.; Inoue, T.; Phan-Van, T. The Vietnam gridded precipitation (VnGP) dataset: Construction and validation. *SOLA* **2016**, *12*, 291–296. <https://doi.org/10.2151/SOLA.2016-057>.
  19. Han, J.; Miao, C.; Gou, J.; Zheng, H.; Zhang, Q.; Guo, X. A new daily gridded precipitation dataset for the Chinese mainland based on gauge observations. *Earth Syst. Sci. Data* **2023**, *15*(7), 3147–3161. <https://doi.org/10.5194/ESSD-15-3147-2023>.
  20. Datasets ECMWF. Available online: <https://www.ecmwf.int/en/forecasts/datasets> (Accessed on 05 June 2024).
  21. Dataset ALOS@EORC. Available online: [https://www.eorc.jaxa.jp/ALOS/en/dataset/aw3d30/aw3d30\\_e.htm](https://www.eorc.jaxa.jp/ALOS/en/dataset/aw3d30/aw3d30_e.htm) (Accessed on 05 June 2024).
  22. FAO/UNESCO Soil Map of the World. FAO soils portal. Food and Agriculture Organization of the United Nations. Available online: <https://www.fao.org/soils-portal/data-hub/soil-maps-and-databases/faounesco-soil-map-of-the-world/en/> (Accessed on 05 June 2024).
  23. Clamarche, “Land Cover CCI product user guide version 2.0”.
  24. Demaria, E.M.; Nijssen, B.; Wagener, T. Monte Carlo sensitivity analysis of land surface parameters using the Variable Infiltration Capacity model. *J. Geophys. Res. Atmos.* **2007**, *112*(D11), 1–15. <https://doi.org/10.1029/2006JD007534>.
  25. Wi, S.; Ray, P.; Demaria, E.M.C.; Steinschneider, S.; Brown, C. A user-friendly software package for VIC hydrologic model development. *Environ. Model. Softw.* **2017**, *98*, 35–53. <https://doi.org/10.1016/J.ENVSOFT.2017.09.006>.
  26. Duan, Q.; Sorooshian, S.; Gupta, V.K. Optimal use of the SCE-UA global optimization method for calibrating watershed models. *J. Hydrol.* **1994**, *158*(3-4), 265–284. [https://doi.org/10.1016/0022-1694\(94\)90057-4](https://doi.org/10.1016/0022-1694(94)90057-4).
  27. Dang, T.D.; Chowdhury, A.F.M.K.; Galelli, S. On the representation of water reservoir storage and operations in large-scale hydrological models: Implications on

- model parameterization and climate change impact assessments. *Hydrol. Earth Syst. Sci.* **2020**, *24(1)*, 397–416. <https://doi.org/10.5194/HESS-24-397-2020>.
28. Linh, B.H.; Phuong, T.A. Assessment of the impact of reservoirs on flow variations on the Da River. *VN J. Hydrometeorol.* **2021**, *731*, 97–107. [https://doi.org/10.36335/VNJHM.2021\(731\).97-107](https://doi.org/10.36335/VNJHM.2021(731).97-107).
  29. Luong, N.D. Application of VIC hydrological model for simulating river flow of red river system to support water resource management. *J. Sci. Technol. Civ. Eng. HUCE* **2017**, *11(6)*, 198–204.
  30. Hiep, N.H.; Luong, N.D.; Nga, T.T.V.; Hieu, B.T.; Ha, U.T.T.; Duong, B.D.; Long, V.D.; Hossain, F.; Lee, H. Hydrological model using ground- and satellite-based data for river flow simulation towards supporting water resource management in the Red River Basin, Vietnam. *J. Environ. Manage.* **2018**, *217*, 346–355. <https://doi.org/10.1016/J.JENVMAN.2018.03.100>.
  31. Li, Y.; He, D.; Li, X.; Zhang, Y.; Yang, L. Contributions of climate variability and human activities to runoff changes in the upper catchment of the Red river basin, China. *Water* **2016**, *8*, 414. <https://doi.org/10.3390/w8090414>.
  32. Duan, Q.; Sorooshian, S.; Gupta, V. Effective and efficient global optimization for conceptual rainfall-runoff models. *Water Resour. Res.* **1992**, *28(4)*, 1015–1031. <https://doi.org/10.1029/91WR02985>.

*Research Article*

# The integration of GNSS RTK and IMU with extended particle filter

Duong Thanh Trung<sup>1\*</sup>

<sup>1</sup> Hanoi University of Mining and Geology; duongthanhtrung@humg.edu.vn

\*Corresponding author: duongthanhtrung@humg.edu.vn; Tel.: +84–932202162

Received: 15 April 2024; Accepted: 14 June 2024; Published: 25 September 2024

**Abstract:** Global navigation satellite system is now widely applied for various applications. For high accuracy requirements such as surveying and mobile mapping system, real-time kinematic positioning (GNSS RTK) is commonly used. In the open sky, GNSS RTK can achieve centimeter level of accuracy in case of RTK fixed solution. However, in the GNSS-denied or -noisy environment such as under tree canopy or under bridge, GNSS RTK accuracy becomes worse. To overcome this issue, this study applies an integrated system consisting of an GNSS RTK module and Inertial Measurement Unit (IMU) to continuously provide navigation solutions including position, velocity, and attitude. For data fusion, Extended Particle Filter (EPF) is used in this research. EPF is considered as a hybrid estimation strategy to overcome the limitations of Extended Kalman Filter, that is popularly used in data fusion. The experimental results indicated the benefit of the integrated system, particularly in the GNSS hostile environment. In addition, the testing result illustrated that the performance of EPF is significant compared to that of EKF.

**Keywords:** GNSS RTK; IMU; Kalman Filter; Integration.

---

## 1. Introduction

Mobile Mapping System (MMS) has been widely applied for collecting geo-spatial data. In principle, MMS has two main steps: (1) capturing images by cameras or point clouds by laser scanners of objects of interest and (2) transforming them into mapping frames based on the internal and exterior orientation parameters [1, 2]. In the MMS, the position and orientation of the mapping sensors are popularly determined based on the integration of the Global Navigation Satellite System (GNSS) and Inertial Measurement Unit (IMU). Due to the low-cost and small size Micro-Electro-Mechanical System (MEMS) IMU is commonly used. However, the performance of the MEMS IMU is restricted, particularly in case of no additional constraint. [3] indicated that with the integration of GNSS and MEMS IMU in open sky areas such as highways and routes between countries, the position accuracy can reach the centimeter level. However, the position and attitude accuracy of MEMS IMU based in the downtown area where GNSS signals are often obstructed still do not meet the requirement of precise mapping with land-based MMS.

The main purpose of this study is thus to improve the performance of MMS utilizing GNSS/MEMS IMU integration while reducing their cost and size. Two kinds of error are presented in the error theory manner: systematic error and noise affecting the performance of the system. With MEMS IMUs, systematic errors are mainly from biases and scale factors of the gyroscopes and accelerometers. Calibration is implemented for treatment. However, intensive calibration with professional equipment would increase the cost significantly. In a practical sense, aid measurements from GNSS and other integrated sensors can compensate for the systematic error of the IMU. Developing an effective integration strategy is thus the

key to reducing the effect of systematic errors in an IMU. Although stable in the long term, GNSS measurements suffer from many sources of deterministic errors, such as ionosphere, troposphere delay, time synchronization error, and multipath [4]. For reliable aid measurements, GNSS data processing is considered.

Unlike systematic errors, noise is a form of un-deterministic error that can be treated by stochastic processing. For this task, the behavior of noise should first be modeled. The general theory about noise modeling was presented by [5] and the behavior of noise in an INS was described by [6, 7]. In general, the noise behavior in INS is divided into four types: white noise, random constant, random walk, and exponentially correlated random. Calibration is necessary and the noise is modeled by an appropriate mathematical process to understand the behavior of sensor noise. The Gauss-Markov process is popularly used to describe and model the behavior of noise. Given that the noise has been modeled, it is accounted for in the estimation process (i.e., Kalman filter (KF)) to obtain the highest probability of the output solutions.

The two effective ways to restrict these kinds of errors to improve the performance of the integrated navigation system are improving GNSS solution using GNSS Realtime Kinematic Positioning (RTK) and using optimal estimation algorithms. While GNSS RTK is easy to archive using enclosed commercial GNSS RTK receivers, this research focuses on estimation strategies. For estimation, the KF [8] is popularly known as an optimal estimation strategy. The KF aims to determine the state vector of the system states based on the minimization of covariance. The advantage of the KF is its reliability and simplicity. The main limitation of KF is that it can only be applied on linear function and assuming Gaussian noises. When the state and measurement model functions are non-linear, Linearized KF (LKF) or Extended KF (EKF) are applied instead of KF for estimation. In these strategies, non-linear functions are linearized keeping the first order of Taylor series expansion. The calculation sequence is similar to that of KF. However, LKF and EKF have limitations that were reported by several researchers [9–12]. The limitations of LKF or EKF are that only small errors are allowed during estimation and the presence of nonlinear error behavior might violate the assumption, thus generating biased solutions. Choosing an appropriate INS error model in KF-based systems is also not a trivial task [13].

One of the approaches to improve the performance of the integrated system is sampling-based filter approach such as Particle Filters (PF) [14, 15] and Unscented Kalman filter (UKF) [10, 13]. A typical and early developed algorithm of sampling-based filtering approaches is the PF. In the PF, the set of points (particles) is generated randomly with associated weights. The details of the PF were presented by [14, 16]. Besides the advantages that have been reported, PF also has several disadvantages that make it unpopular in integration. PF relies on important sampling, thus requires the design of a proposal distribution that can approximate the posterior distribution reasonably well. Designing such proposals is generally hard [14, 15]. Another improvement of sampling-based filter methods is using a hybrid scheme between generic PF and other linear Gaussian estimation methods. The study [17] introduced hybrid methods in which EKF and UKF Gaussian approximations are used as the proposal distribution for PF. The simulation result shows that this hybrid scheme, particularly PF based on UKF, performs better than other linear Gaussian estimation methods such as EKF and UKF. The study [18] applied and evaluated the performance of UPF, UKF, and EKF with INS/GPS integration using MEMS IMU. The results indicate that the improvement of non-linear, non-Gaussian estimation compared with EKF was about 10% to 20%. The study [19] evaluated the feasibility of some estimations for non-linear function in positioning. The study [20] evaluated the performance of a low-cost INS/GPS integration system using the street return algorithm.

In general, the advantage of sampling-based methods over KF-based methods is that it can be applied on a non-linear function with arbitrary density distribution. Their performance

is thus better than that of KF-based methods. Some limitations of sampling-based methods were still reported. The choice of an optimal proposal probability density function to draw samples is difficult to implement. The manner of generating the samples is also a difficult task for certain applications. Computational burden is the main disadvantage of these algorithms for real-time applications. In order to deal with non-Gaussian noise in the GNSS/IMU system, this study applies a non-linear, non-Gaussian estimation algorithm, called Extended Particle Filter (EPF) to improve the performance of the system.

## 2. Methods

### 2.1. Integration strategy

In the integration scheme, the GNSS carrier-phase measurements are processed using a base station. The GNSS RTK module provides positions and velocities in the navigation frame as the updating measurements for the data fusion engine such as EKF. Angular rates and specific forces, the output of IMU is processed based on an INS mechanization to provide position, velocity, and attitude. In data fusion engine, EKF is first applied. A set of particles is generated based on Gaussian approximation from EKF output. EPF is then applied to provide optimal solutions. Figure 1 shows the integration scheme.

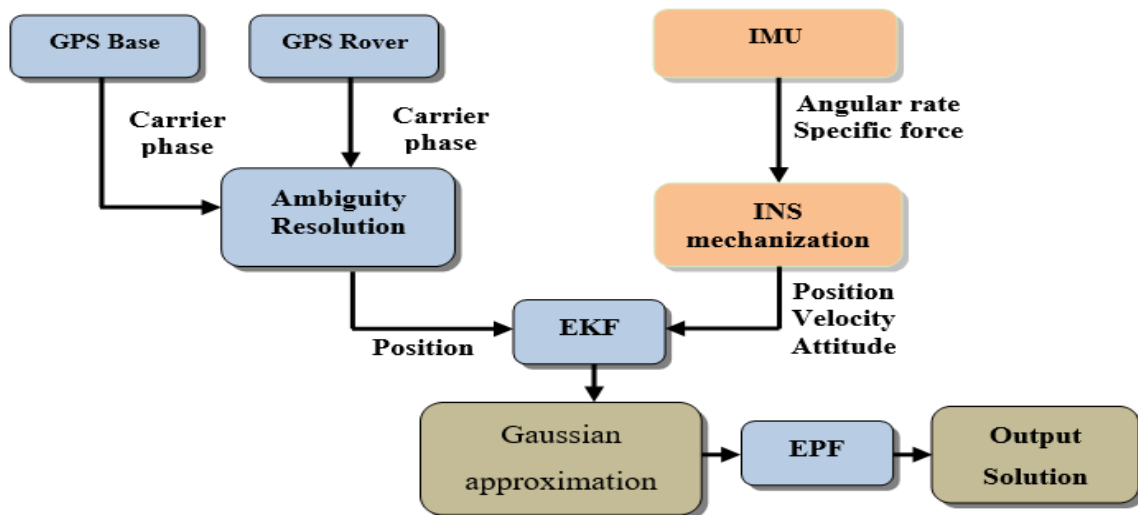


**Figure 1.** The integration scheme.

### 2.2. Extended Kalman Filter

EKF is the combination of nonlinear and linearized filtering techniques. In the prediction step, the nonlinear function is directly used to time-update the state vector, but the associated covariance is estimated based on the Jacobian matrix:

$$x_k = f(x_{k-1}) + w_{k-1} \tag{1}$$

where  $x_k$  is the state vector consisting of position, velocity, and attitude at time  $k$ ;  $w$  is system noise. Components of state vector is described in the below equation:

$$x_{21 \times 1} = [r^n v^n r_b^n b_g b_a s_g s_a]^T \tag{2}$$

where  $r^n$ ,  $v^n$ , and  $r_b^n$  are position, velocity, and attitude of the system in the navigation frame;  $b_g$ ,  $b_a$ ,  $s_g$ , and  $s_a$  are the biases and scale factors of the IMU, respectively.

In the measurement update step, state vector is propagated through the nonlinear measurement equation to calculate the innovation in the next step:

$$z_k = h(x_k) + n \tag{3}$$

where  $z_k$  is an updating measurement;  $h(x_k)$  is a function of a state vector;  $n$  is the measurement noise.

Figure 2 depicts the process and the performance of the EKF.

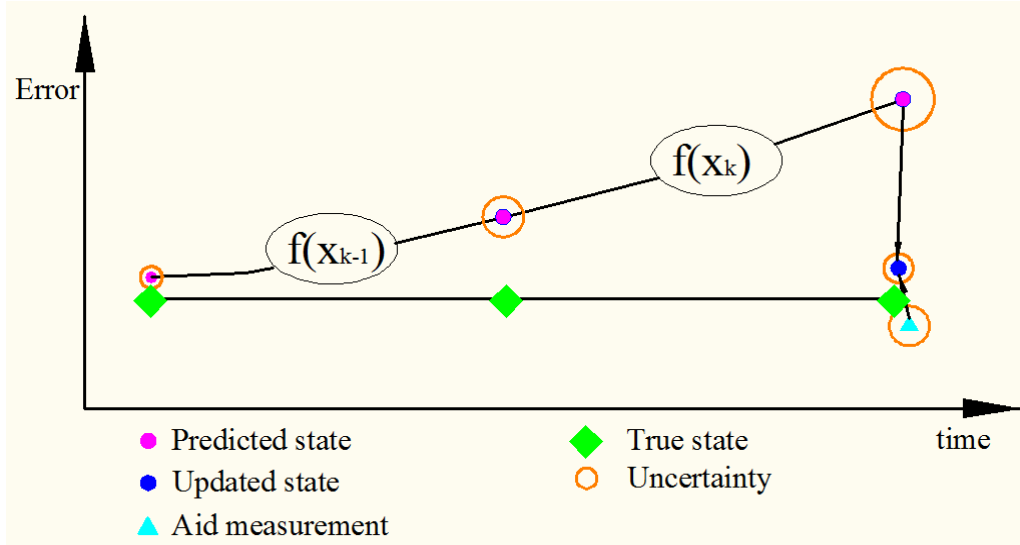


**Figure 2.** The process and performance of the EKF.

### 2.3. Estimation with Extended Particle filter

Generally, the hybrid estimation strategies use a Gaussian approximation as the proposal distribution to generate particles. A Gaussian approximation of  $P(x_k | x_{k-1}, z_{0:k})$  using EKF is called Extended Particle Filter (EPF). In these strategies, first, EKF is implemented to obtain the Gaussian approximation of  $P(x_k | x_{k-1}, z_{0:k})$  including estimates of the state and their covariances. Then the particles are sampled based on those estimates.

$$\hat{x}_k^i = f(X_{k-1}^i, w^i) \tag{4}$$

With associated weight

$$w_k^i = \frac{p(z_k | \hat{x}_k^i) p(\hat{x}_k^i | X_{k-1}^i)}{N(\hat{x}_k, P_k)} \tag{5}$$

where  $P(x_k | x_{k-1}, z_{1:k-1})$  denotes the distribution density function of  $x_k$  given  $x_{k-1}$  and  $z_{1:k-1}$ ;  $N(\cdot)$  denotes the Gaussian distribution;  $\hat{x}_k, P_k$  are mean and covariance approximated by EKF.

The state vector and covariance matrix of the current time epoch are determined by weighted average of the generated particle:

$$\hat{x}_k^- = \sum_{i=0}^N w^i X_k^i \tag{6}$$

$$P_{xx}^- = \sum_{i=0}^N w^i (X_k^i - \hat{x}_k^-) (X_k^i - \hat{x}_k^-)^T \tag{7}$$

Figure 3 describes the flowchart of the hybrid estimation and Figure 4 illustrates the principle of this estimation strategy.

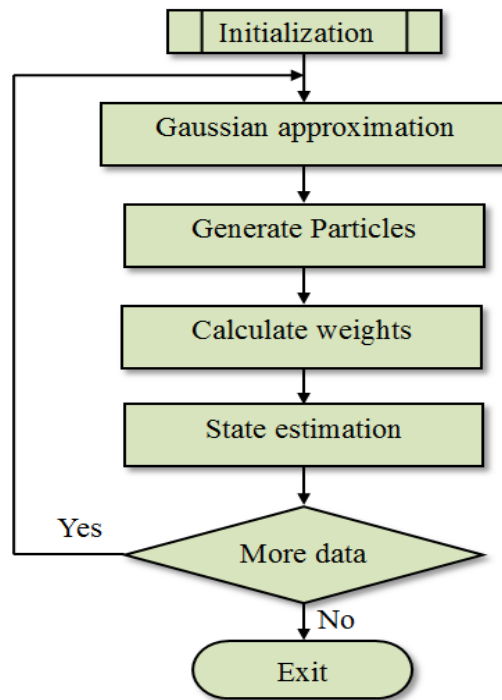


**Figure 3.** Flowchart of Extended Particle Filter.

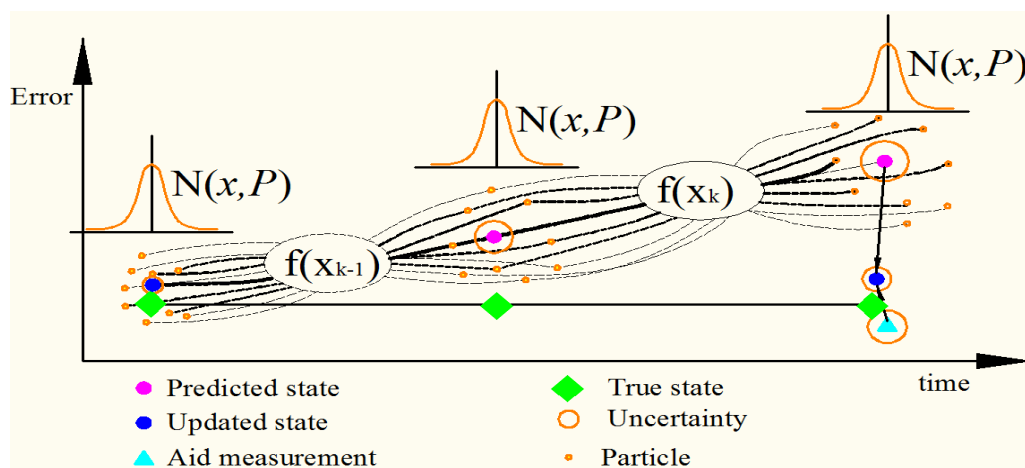


**Figure 4.** Principle of Extended Particle Filter with Gaussian approximation.

### 3. Experiment and discussion

The purpose of the experiment is to evaluate the performance of the integrated system in comparison with a stand-alone GNSS receiver and between estimation strategies, including EKF and EPF. For those purposes, three systems were set up on a platform to evaluate the performance of the given system and methodology. The reference system is a dual frequency RTK GNSS receiver, Leica viva GS16. The system is connected with the VNGEONET CORSs for RTK fixed solutions. In addition, various check points were built along the reference trajectory. The coordinates of the check points were determined by using a total station, the accuracy is guaranteed at the level of centimeter. The first testing system is a single frequency GNSS receiver, GNSS EVK-NEO M8T to provide Single Point Positioning (SSP) solution. The second testing system is the integration of the GNSS RTK module, Ublox ZED-F9P and an IMU, Xsens-MTi-3. Specification of the integrated system is described in table 1. The integrated system and testing platform is depicted in Figures 5a, 5b.



**Table 1.** The specification of main components.

Devices	Unit	Value
Number of concurrent GNSS	GNSS system	4
Position accuracy	m	0.01 m + 1 ppm
Output rate	Hz	1 Hz
Gyroscope	Unit	Value
In-run Bias	[°/s]	10
Noise density	[°/s/√Hz]	0.007
Non-linearity	[%FS]	0.1
Accelerometer		
In-run Bias	[mg]	0.03
Noise density	[mg/√Hz]	120
Non-linearity	[%FS]	0.5

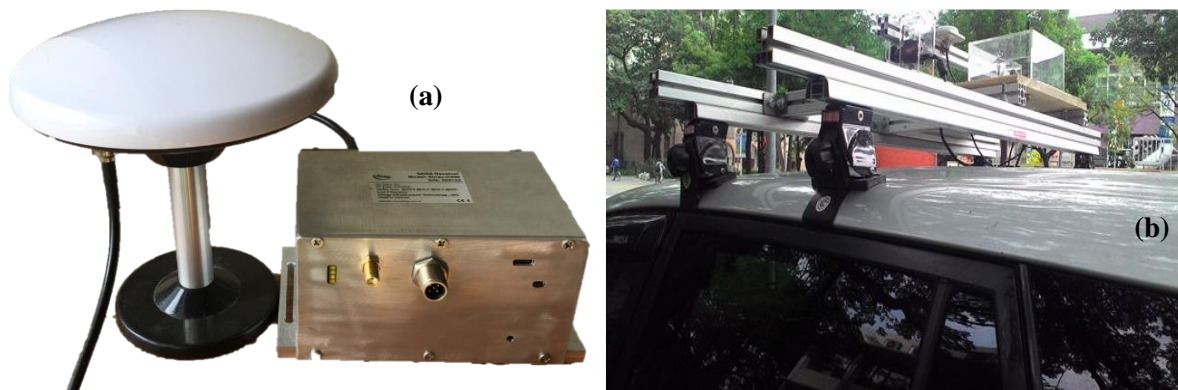


**Figure 5.** The integrated system (a) and testing platform (b).

The data were collected continuously under different environment scenarios, including in open sky view and GNSS-denied view in Hanoi, Vietnam (Figure 6). The integrated GNSS RTK/IMU data is processed by a software module written in C++ programming language with two algorithms, EKF and EPF. The graphical user interface of the software module can be seen in Figure 7a. For analysis, four output solutions including GNSS SSP, GNSS RTK, GNSS RTK/IMU with EKF and GNSS RTK with EPF are compared with GPS time synchronization. The trajectory of the test can be seen in Figure 7b. For detailed analysis, enlargements of two typical testing scenarios including in the open sky view and under bridge view as shown in Figures 8a, 8b. The numerical analysis can be seen in Tables 2, 3.



**Figure 6.** Testing scenarios in open sky view (a) and GNSS-denied view (b).

**Table 2.** Numerical results in the open sky view area.

	Availability (%)	Min(m)	Max(m)	Mean(m)	Std. Deviation(m)
GNSS SSP	99	0.450	9.610	2.400	1.560
GNSS RTK	95	0.002	0.720	0.030	0.026
GNSS RTK/IMU EKF	99	0.003	0.810	0.040	0.035
GNSS RTK/IMU EPF	99	0.003	0.710	0.040	0.032

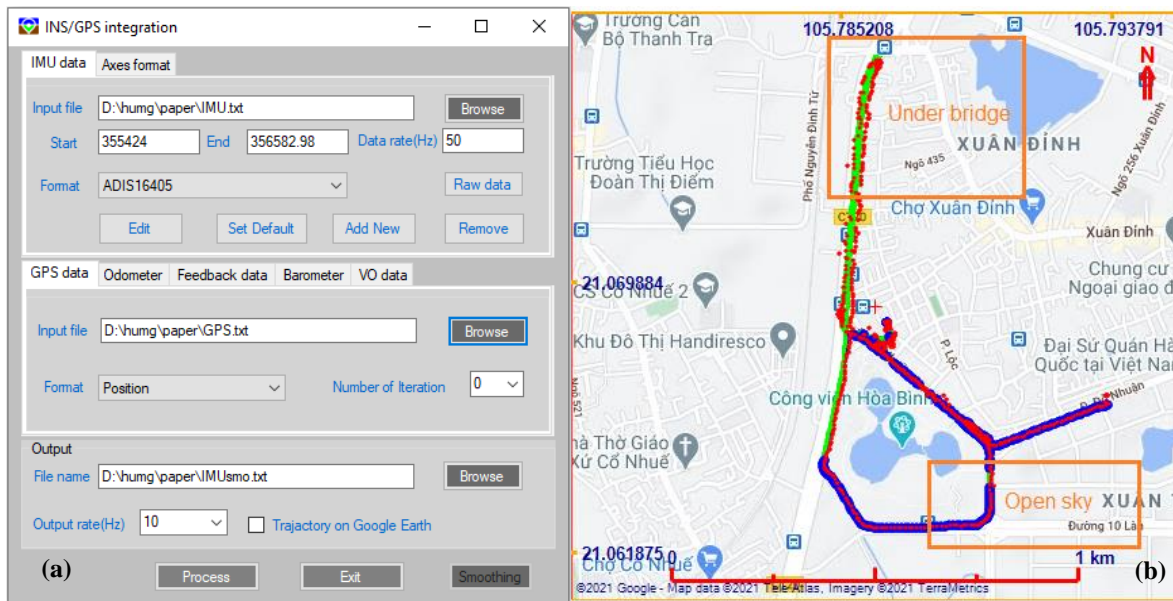


**Figure 7.** (a) GUI of the software module, (b) Testing trajectory of the test.

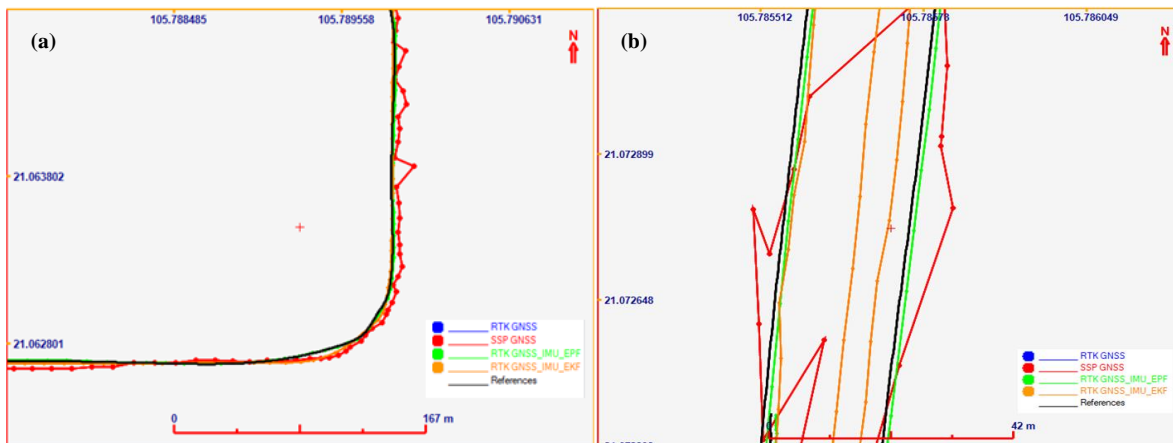


**Figure 8.** (a) Enlargement of scenario open sky view area in the test, (b) Enlargement of under bridge area in the test.

**Table 3.** Numerical result in the under-bridge area.

	Availability (%)	Min(m)	Max(m)	Mean(m)	Std. Deviation(m)
GNSS SSP	72	0.120	20.600	4.650	5.560
GNSS RTK	57				
- SSP	20	0.05	5.820	3.540	4.563
- RTK float	0				
- RTK fixed	0				
GNSS RTK/IMU_EKF	99	0.015	10.530	2.401	3.403
GNSS RTK/IMU EPF	99	0.012	1.530	1.240	1.340

From the test, in the open sky, GNSS can continuously provide solutions with homogenous accuracy. GNSS RTK can provide a position at accuracy about 3 centimeters while GNSS SSP can provide 1.5-meter level of accuracy. Consequently, the integration of GNSS RTK/IMU with EKF or EPF can provide navigation solution at accuracy of about 3-4 centimeters. In this case EKF or EPF do not help to improve the accuracy of the system because the position update mainly relies on the GNSS RTK.

In the under-bridge environment, accuracy, and availability of GNSS degrade seriously. The availability of GNSS SPP solution is 72% at accuracy of about 6 meters. In this testing scenario, GNSS RTK cannot provide RTK fixed solution any time, only RTK float solution

of 20% and 57% of SSP. Overall positional standard deviation of GNSS RTK is about 5 meters. In contrast, with the integration of GNSS RTK and IMU, availability of navigation solution is still at 99%. In this case, the performance of EPF is better than that of EKF with standard deviation of 1.3m compared to 3.4m in the EKF.

#### 4. Conclusions

This research evaluates the performance of an integration scheme that combines the GNSS RTK and IMU and an estimation strategy called EPF.

Field test in different environmental scenarios were implemented to collect data for analyzing the performance of the different integration architecture and estimation strategies.

The result from the experiment indicated that the integration of GNSS RTK/IMU enables to seamlessly provide navigation solution in any environmental scenarios. However, the positional accuracy of the system mainly relies on the position provided by GNSS.

The EPF with non-Gaussian noise estimation performs a significant improvement in terms of positional accuracy compared to that of EKF.

**Author contribution statement:** Designed the study conception: D.T.T.; collected data: D.T.T.; developed the theoretical research: D.T.T.; processed the data and performed the simulations: D.T.T.; analyzed the data: D.T.T.; contributed largely to revising the final manuscript: D.T.T.

**Acknowledgments:** This study is supported by project No. ĐT.CNKK.QG.011/23 funded by Ministry of Industry and Trade of the Socialist Republic of Vietnam.

**Competing interest statement:** The authors declare no conflict of interest.

#### References

1. Toth, C.K. R&D of mobile LIDAR mapping and future trends. Proceedings of SPRS, Baltimore, Maryland, 9–13 March 2009.
2. Rau, J.Y.; Habib, A.F.; Kersting, A.P.; Chiang, K.W.; Bang, K.I.; Tseng, Y.H.; Li, Y.H. Direct Sensor Orientation of a Land-Based Mobile Mapping System. *Sensors* **2011**, *11*, 7243–7261.
3. Huang, Y.W.; Chiang, K.W. The Applicability analysis of LC and TC low cost MEMS IMU/GPS POS systems for land based MMS. Proceeding of the ENC-GNSS, 2009.
4. Seeber, G. Satellite geodesy. Walter de Gruyter, Berlin, New York, 2003.
5. Shin, E.H. A quaternion-based unscented Kalman filter for the integration of GPS and MEMS INS. Proceedings of ION GNSS, Long Beach, California, 21–24 September 2004.
6. Titterton, D.H.; Weston, J.L. Strapdown inertial navigation technology, second edition. American Institute of Aeronautics and Astronautics, Reston, USA, 2004.
7. Rogers, R.M. Applied mathematics in integrated navigation systems. Third Edition, AIAA, Virginia, USA, 2007.
8. Kalman, R.E. A new research approach to linear filtering and prediction problem. *J. Basic Eng.* **1960**, *82*, 35–45.
9. Brown, R.G.; Hwang, P.Y.C. Introduction to random signals and applied Kalman filtering. John Wiley & Sons Inc., 1997.
10. Julier, S.J.; Uhlmann, J.K. New extension of the Kalman filter to nonlinear systems. Proceedings of the SPIE, 1997, pp. 182–193.
11. Chiang, K.W.; Noureldin, A.; El-Sheimy, N. Multi-sensors integration using neuron computing for land vehicle navigation. *GPS Solutions* **2003**, *6*(3), 209–218.

12. El-Sheimy, N.; Abdel-Hamid, W.; Lachapelle, G. An adaptive neuro-fuzzy model for bridging GPS outages in MEMS-IMU/GPS land vehicle navigation. Proceedings of ION GNSS, Long Beach, California, 21–24 September 2004.
13. Shin, E.H. Estimation techniques for low-cost inertial navigation. UCGE Reports Number 20156, 2005.
14. Gordon, N.J.; Salmond, D.J.; Smith, A.F.M. Novel approach to nonlinear/non-Gaussian Bayesian state estimation. *IEE Proceedings F (Radar Signal Processing)* **1993**, *140*(2), 107–113.
15. Haug, A.J. A tutorial on Bayesian estimation and tracking techniques applicable to nonlinear and non-gaussian processes. MITRE technical report, 2005.
16. Lee, J.K. The estimation method for an Integrated INS/GPS UXO geolocation system. Technical Report No. 493, The Ohio State University, Columbus, Ohio, 2009.
17. Van Der Merwe, R.; Doucet, A.; De Freitas, N.; Wan, E. The unscented particle filter. *Adv. Neural Inf. Process. Syst.* **2000**, 584–590.
18. Duong, T.T.; Chiang, K.W. Non-linear, non-Gaussian estimation for INS/GPS integration. *Sensor Letter* **2012**, *10*(6), 1081–1086.
19. Dung, P.T.; Trung, D.T. Ability of filtering algorithms for non-linear model used for positioning. *J. Min. Earth Sci.* **2017**, *58*(4), 34–42.
20. Thang, N.V.; Thang, P.M.; Tan, T.D. The performance improvement of a low cost INS/GPS integration system using the street return algorithm. *VN J. Mech.* **2012**, *34*(4), 271–280.

*Research Article*

# Application of geomechanical models to predict sand production and propose well completion solutions for Well X in the Hai Thach field

Duyen Quang Le<sup>1\*</sup>

<sup>1</sup> Hanoi University of Mining and Geology, Hanoi, Vietnam; lequangduyen@humg.edu.vn

\*Corresponding author: lequangduyen@humg.edu.vn; Tel.: +84–982380188

Received: 27 April 2024; Accepted: 15 June 2024; Published: 25 September 2024

**Abstract:** Sand production is a serious problem during oil and gas production in unconsolidated sandstone formations. It can rapidly damage downhole and surface equipment. Therefore, oil and gas contractors constantly seek methods to control sand production. However, in unconsolidated sandstone formations, sand production typically occurs during the later stages of production. Some wells encountered sand production from the beginning stage, while others could be produced without having sand production if managed properly. This indicates that sand production is influenced by both reservoir properties and well production operating conditions. Reservoir properties can be determined during the exploration phase. Additionally, several researchers have demonstrated that sand production mechanisms are linked to these reservoir parameters. In this paper, we employ a geomechanical model to predict the critical reservoir pressure and critical drawdown pressure values leading to sand intrusion and subsequently propose well completion strategies of Expandable Sand Screens to prevent sand production and optimise production performance processes to enhance the efficiency of oil and gas exploitation investments. The accurate assessment of sand occurrence in production process potential enables investors to make mindful decisions regarding sand control measures for specific wells. Sand control is an expensive and risky undertaking; however, it is crucial for wells with high sand production potential to prevent damage to surface equipment and operational complications caused by sand.

**Keywords:** Geomechanical modeling; Sand intrusion; Pressure; Sand control; Well completion.

---

## 1. Introduction

The Hai Thach field is located in block 05-2, the south part of the Nam Con Son basin, on the continental shelf of southern Vietnam. The field is 330 km southeast of Vung Tau city, an oil and gas field in a deep-water area of 134 m. The field produces from miocene unconsolidated sandstone reservoirs (Dong Nai formation, BIII sand), middle miocene (upper and lower Con Son formation, BII.2.20, BII.2.30, and BII.1.10 Sands), lower miocene (upper and lower Bach Ho formation, BI.2.20, BI.2.30, BI.1.20 sands), lower oligocene (lower Tra Tan formation, E.10 and E.20 sands), and pre-tertiary basement. The structural configuration of the Hai Thach gas field includes horseshoe-shaped faults trending north, northeast, and south-southeast (MMH & LMH) and block-type shoulder faults trending east (MMF) located below the main discontinuous unit (MMU). Most faults are truncated at MMU, but a few faults extend and overthrust the UMA unit. Well X drilled on the horseshoe-shaped structure of the Hai Thach field [1, 2]. The cross-sections of some of the gas reservoirs that Well X will penetrate are shown in Figure 1.

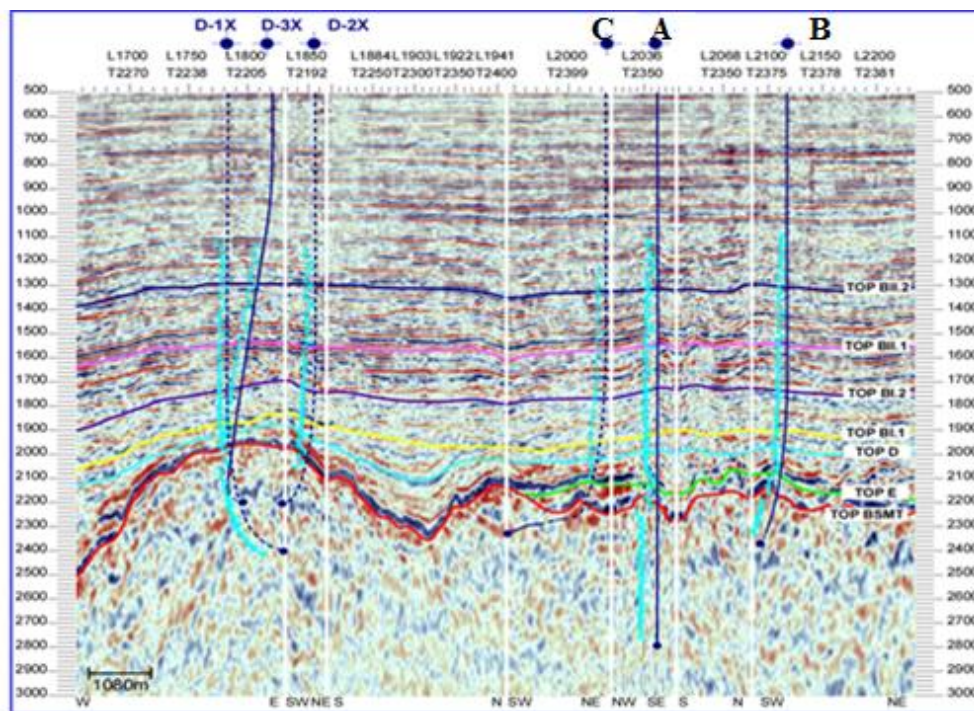


Figure 1. Geological Cross-Sections of the Hai Thach field.

Sand production in the oil and gas production process occurs when a significant number of solid particles detach from the formation. These particles are carried by the fluid flow into the well and to the surface along with the produced hydrocarbons.

These solid particles can be different in composition and size, but they are primarily sand particles with a size range of 0.60 mm to 4.75 mm. When the amount of these solid particles exceeds the allowable limit, sand control measures must be implemented to protect the well, downhole equipment, and ensure safe and efficient production. This allowable limit depends on the equipment, type of sand, reservoir conditions, and company strategy [3]. A common benchmark for comparison is 0.1% of the total produced volume.

The reservoir lithology in the Hai Thach field is mainly weakly consolidated sandstone. Sand production in these reservoirs occurs in two stages. The specific form of sand production varies depending on the characteristics of the reservoir. To effectively control sand production, it is essential to understand the characteristics of the reservoir being produced and select the appropriate treatment method.

## 2. Materials and methods

### 2.1. Pressure model

When a well is drilled into a formation, the rock material is displaced upwards. The wellbore wall is only supported by the drilling fluid pressure in the wellbore. If this fluid pressure is not balanced with the in-situ stresses, stress redistribution occurs around the wellbore. This can lead to a total stress greater than the formation's resistance, resulting in failure.

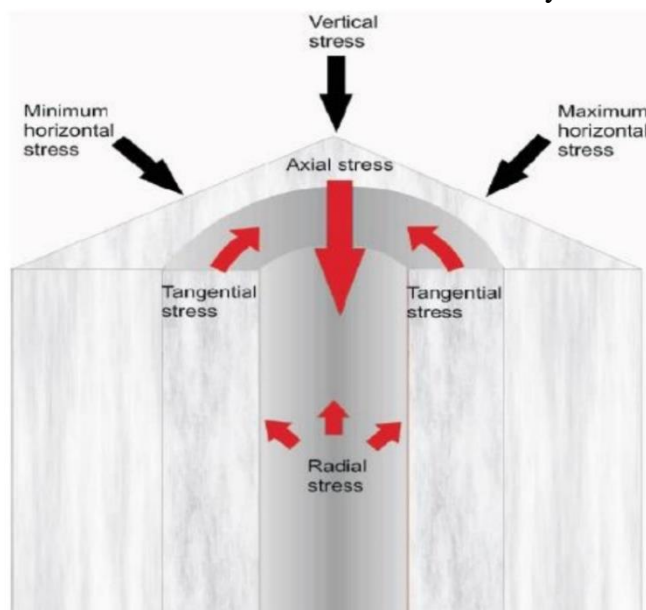


Figure 2. In-situ stress model around a drilled wellbore

The various stresses and pressures include:  $\sigma_v$  is the vertical stress;  $\sigma_H$  is the maximum horizontal stress,  $\sigma_h$  is the minimum horizontal stress;  $p_f$  is the drilling fluid pressure in the formation;  $p_w$  is the flowing pressure of fluid from the formation into the well;  $\sigma_\theta$  is the tangential stress;  $\sigma_r$  is the radial stress;  $\sigma_z$  is an axial stress, typically vertical.

The determination of new stresses around a wellbore involves considering the inclination angle ( $i$ ) and the azimuth angle ( $\theta$ ). According to reference [21], the new stress values can be calculated using the following formulas:

$$\sigma_x = \sigma_H \cos^2 \theta \cos^2 i + \sigma_h \sin^2 \theta \cos^2 i + \sigma_v \sin^2 i \tag{1}$$

$$\sigma_y = \sigma_H \sin^2 \theta + \sigma_h \cos^2 \theta \tag{2}$$

$$\sigma_z = \sigma_H \cos^2 \theta \sin^2 i + \sigma_h \sin^2 \theta \sin^2 i + \sigma_v \cos^2 i \tag{3}$$

When considering a soil or rock element on the wellbore wall, the stresses are distributed according to a cylindrical coordinate system with coordinates ( $r, z, \theta$ ).

$$\tau_{xy} = \frac{1}{2}(\sigma_H - \sigma_h) \sin 2\theta \cos i \tag{4}$$

$$\tau_{xz} = \frac{1}{2} \sin 2i(\sigma_v - \sigma_H \cos^2 \theta - \sigma_h \sin^2 \theta) \tag{5}$$

$$\tau_{zy} = \frac{1}{2}(\sigma_H - \sigma_h) \sin 2\theta \cos i \tag{6}$$

When analyzing stress distribution around wellbores, the polar coordinate system is often used to represent the stress components. The stress values for soil or rock elements surrounding the wellbore in polar coordinates are shown in Figure 3.

Wellbore Stability Analysis Using the Fracture-Strain Model for Vertical Well X: The fracture-strain model for vertical wells assumes that the principal stresses are perpendicular to the wellbore axis are shown in Figure 4. This implies that the stresses at the wellbore wall can be represented by:

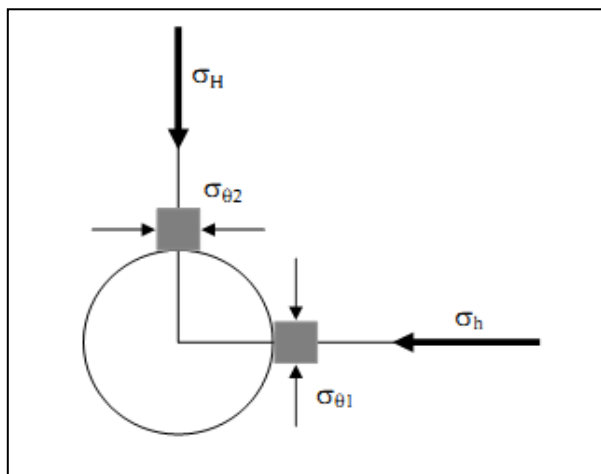


**Figure 4.** Tangential stress at the wellbore wall [5].

While other stress components also contribute to wellbore failure, their effects are considered negligible in this model [6].

To establish a sand production model, it is crucial to identify the time or location at which wellbore failure initiates, leading to sand intrusion. To prevent this phenomenon, the maximum effective tangential stress ( $\sigma_{\tau 1} - p_w$ ) must be less than the effective strength ( $U$ ) of the formation. This can be expressed as:

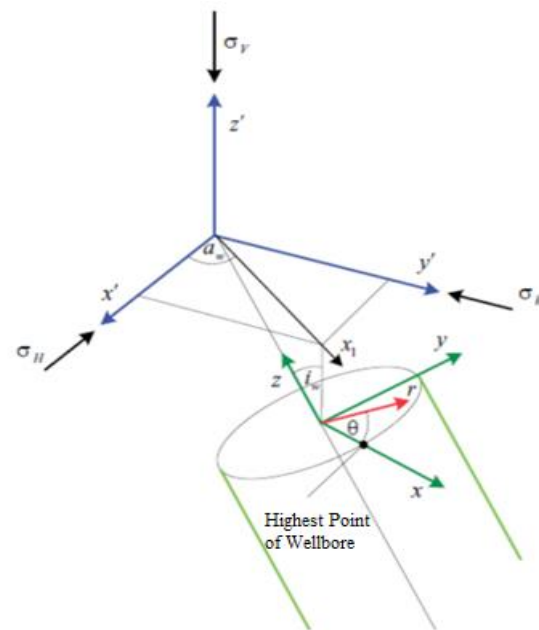


**Figure 3.** Stress state at the wellbore.

The model is based on the premise that wellbore failure occurs when the tangential stress at the wellbore wall exceeds a certain

$$\sigma_{\tau 1} - p_w \leq U \tag{7}$$

According to [3], the bottomhole pressure value to prevent sand production is determined as follows:

$$p_w \geq \frac{3\sigma_H - \sigma_h - U}{2 - A} - P_o \frac{A}{2 - A} \tag{8}$$

The critical drawdown pressure (CDP) is defined as the maximum reduction in wellbore pressure from reservoir pressure that can be applied without causing wellbore failure. It can be determined using the following equation:

$$p_w = P_o - CDP \tag{9}$$

Substituting Equation (7) into Equation (8), we obtain:

$$P_o = \frac{1}{2} [3\sigma_H - \sigma_h - U + CDP(2 - A)] \tag{10}$$

or

$$CDP = \frac{1}{2 - A} [2P_o - (3\sigma_H - \sigma_h - U)] \tag{11}$$

While the wellbore fracture model presented earlier can be applied to vertical wells, adjustments are necessary for inclined wells due to their non-vertical orientation. These adjustments account for the influence of wellbore inclination on stress distribution and formation failure.

The critical reservoir pressure (CRP) is defined as the reservoir pressure drop corresponding to a CDP of zero. This implies that at this pressure, formation failure can occur under any further pressure reduction. The relationship between CRP and CDP can be expressed as:

$$CRP = \frac{3\sigma_H - \sigma_h - U}{2} \tag{12}$$

The formation strength (U) represents the maximum stress that the formation can withstand before failure. It is typically determined through laboratory experiments on thick-walled cylindrical samples with outer-to-inner diameter ratios ranging from 3 to 3.8. [6–8]. The expression for U is given by:

$$U = 3.1TWC \tag{13}$$

The thick-walled cylinder strength (TWC) can be determined experimentally or through empirical formulas [5]:

$$TWC = 83UCS^{0.5242} \tag{14}$$

The aforementioned formulas and parameters can be incorporated into a computational model to assess the critical reservoir pressure (CRP) and formation failure potential. The model can be implemented using Excel to perform calculations and generate results.

## 2.2. Data collection and processing

Well X research was carried out in reservoir E20, this is a well with a vertical well completion zone, with coefficient stress change ratio is 0.62 and reservoir has Max. Perforation diameter 1.965inch, bio elastic is 1, depletion is zero percent, The average particle diameter is 300 μm with reservoir data given in Table 1.

**Table 1.** Input data for well X in reservoir E20 GOC [1].

Well Diameter (in)	True vertical depth (TVD) (m)	Inclination (deg.)	Azimuth (deg.)	Poisson's ratio (MPa)	Pore pressure (deg.)	Unconfined Compressive strength (Psi)	Vertical stress (Psi)	Min Horizontal Stress (Psi)	Max Horizontal stress (Psi)	Mean grain diameter (μm)
12.25	2266	52.7	230.5	0.26	3197	1870	6650	4959	5207	204.8



### 3. Results and discussion

#### 3.1. Calculate sand generation pressure for well X

By using Microsoft Excel software and using the formulas from (1) to (11), with the data of well X given in Table 1. The study can determine the intermediate parameters of stresses as shown in Table 2.

**Table 2.** The calculation results of the stress.

$\sigma_x$	$\sigma_y$	$\sigma_z$	$\tau_{xy}$	$\tau_{xz}$	$\tau_{zy}$
6173.61	4900	5626.38	99.34	751.75	141.88

After calculating the stress components, we calculate the intermediate components and the resulting pressure drop is given in Table 3.

**Table 3.** The calculation results of physical and mechanical components of rock.

A	TWC	U	CRP	CDP	CBHFP
0.67	4222.45	10302.78	1659.03	2536.45	813.54

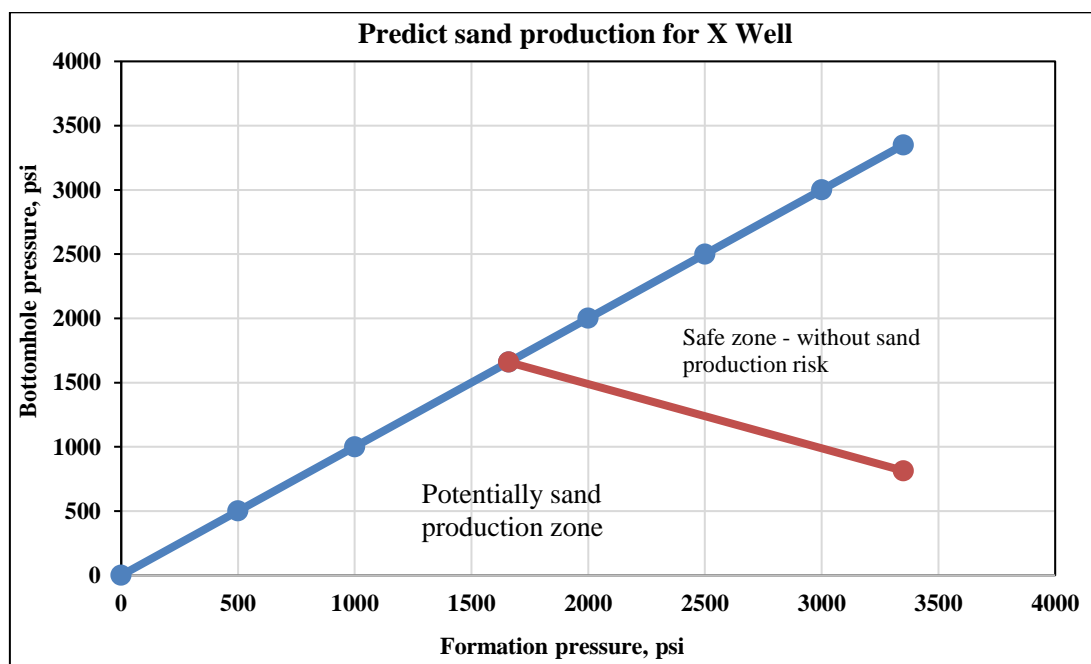


**Figure 5.** Critical drawdown pressure results for well X.

The presented model is constructed based on data that elucidates the influence of reservoir pressure and drawdown on formation failure. The X-axis represents reservoir pressure, while the Y-axis represents wellbore pressure. A diagonal line (in blue) denotes the positions where reservoir pressure equals wellbore pressure, dividing the graph into two sections. The upper portion represents the scenario of overbalanced drilling and injection, while the area below the line represents the drawdown process during well production. The failure line (safe zone - without sand production risk) is also depicted on the graph. In Figure 5, the failure line (in red) intersects the diagonal line at a pressure of approximately 1659 psi. This represents the threshold below which wellbore pressure should not fall to prevent sand production. This failure line varies depending on the specific rock strength and completion method employed. Rock strength is typically determined by the Unconfined Compressive Strength (UCS) value. The failure line illustrates the pressure conditions under which

reservoir and wellbore pressures can cause formation failure. In the presented graph, the region (Safe zone - without sand production risk) encompasses pressure conditions above the failure line, indicating the absence of sand production. Conversely, the area to the left represents the zone where formation failure and potential sand production occur [9–11].

We get the results of the sand production zone pressure, the results for well X are shown in Figure 5. We determine the maximum wellbore decline pressure (Max. Drawdown, CBHFP) is 8.13.54 psi and the maximum decline reservoir pressure (Max. Depletion Reservoir Pressure) is 3350 psi (Figure 5). Therefore, controlling bottom pressure to maintain reservoir pressure within the threshold of not generating sand will optimize the exploitation process.

### 3.2. Proposed completion solutions for Well X using gravel-packed screens

The type of screen, screen mesh size, and gravel size (if using gravel packing) should be carefully designed and selected based on the specific characteristics and properties of the formation. Gravel packing design procedure for wells [12]: Particle size analysis based on core samples; gravel selection; screen selection; gravel transport fluid selection; method for placing gravel mixture at the well bottom. This study introduces a method for particle size analysis based on core samples and presents the selection criteria of gravel and screen. After analyzing the grain size distribution of the reservoir sand, the authors selected the gravel packing material and then, based on the screen selection criteria, calculated the screen opening size and selected the Expandable SandScreen.

Currently, there are many types of sand screens available worldwide, such as Expandable Screens, Con-Slot screens, gravel-pack screens, etc. This study focuses on one type of sand screen, the Expandable Screen. This type of sand screen is expandable and can be adjusted in size, making it a new product in this field with significant advantages over previous sand screens. Expandable Screens can replace both conventional and modern sand control techniques due to their superior design: they eliminate the annular space between the wellbore and the screen, maximizing the flow area inside the production tubing and stabilizing the flow within the tubing [13–15].

Expandable Sand Screens (ESS) represent a significant advancement in sand control technology, addressing the issue of sand production by utilizing an expanding screen that fills the annular gap between the wellbore and the formation. This innovative design not only eliminates the need for gravel packing but also provides enhanced formation support. Additionally, the installation of ESS reduces the required casing size during wellbore completion and facilitates easy intervention for adjustments [16].

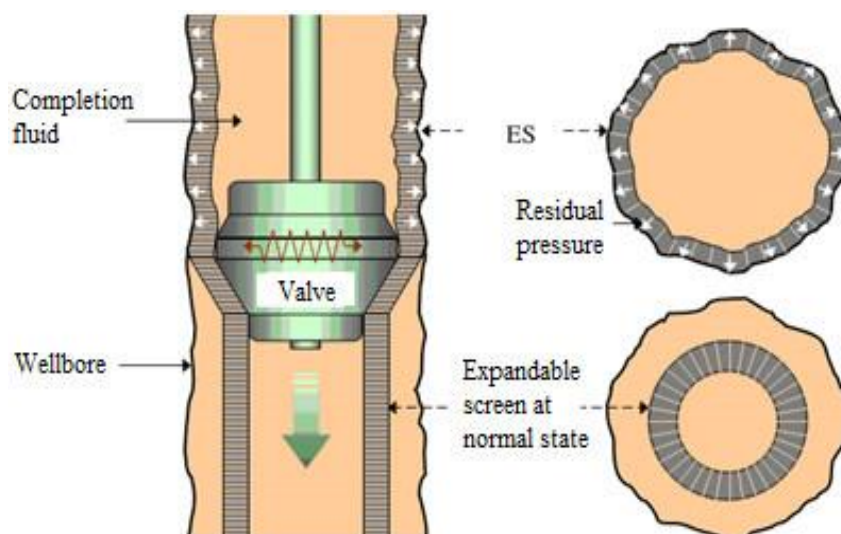


**Figure 6.** Expandable Screen [14].

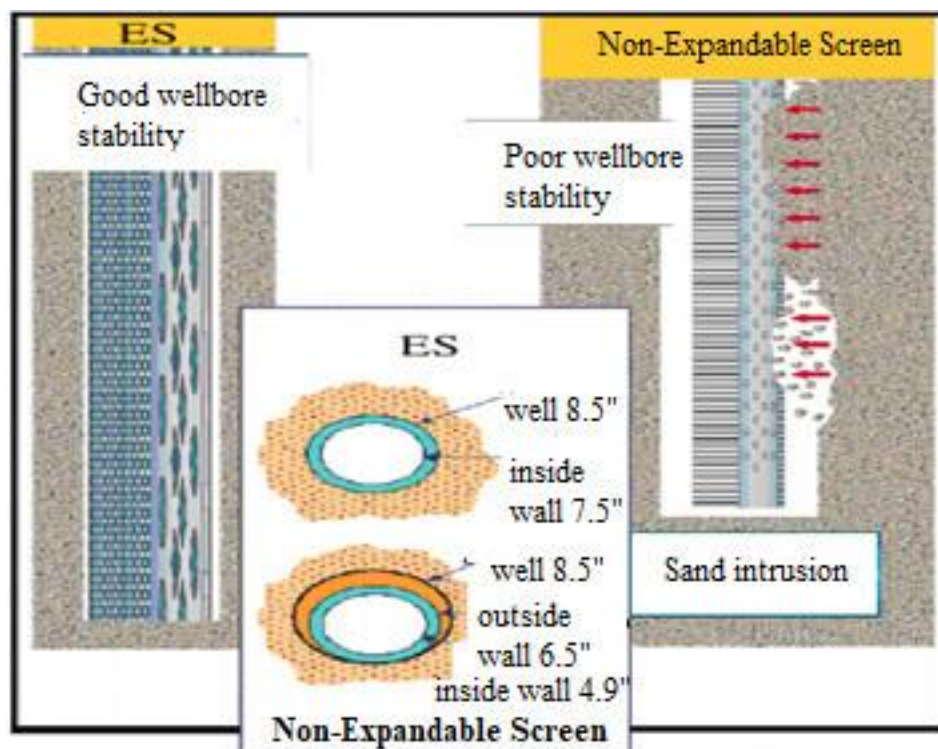


Figure 7. Expandable Screen around annulus [17].

Expandable sand screens (ESS) have revolutionized sand control equipment by eliminating the annular gap between the wellbore and the screen [18]. This innovative design maximizes the flow area within the production tubing, eliminating turbulent flow along the annular space and minimizing erosion of the wellbore. Consequently, ESS contributes to enhanced wellbore stability.

Compared to open-hole completions and gravel packing techniques, ESS offers a more uniform pressure drawdown and a less variable inflow characteristic. These advantages translate into improved production capabilities, particularly in horizontal wells. Additionally, ESS implementation in multilateral wells is significantly simpler compared to conventional sand control methods, which often involve complex installation procedures and are prone to operational issues [19–20].

#### 4. Conclusion

Given the complexities of the oil and gas industry and the ever-increasing demand for energy, the pursuit of optimized sand control methods remains crucial. Sand production, especially in large quantities, can lead to severe consequences, including sand accumulation in wellbores and surface equipment, erosion of both downhole and surface equipment, and formation collapse.

Utilizing geomechanical models to determine sand production pressure serves as a valuable tool in sand management and mitigation strategies. These models enable the identification of sand production thresholds and critical drawdown pressures for the formation. Armed with this information, petroleum engineers and mining technology experts can promptly implement effective reservoir management measures to minimize sand production and optimize reservoir extraction.

For gas wells in the Hai Thach field, expandable screen (gravel-packed screen) sand control methods have been proven suitable for wells experiencing sand intrusion after a period of production. However, their implementation requires:

- Elimination or filling of the annular gap;
- Creation of the smallest possible choke or elimination of sand accumulation;

- Minimize pressure loss during fluid flow;
- Reduction or elimination of gravel bag damage;
- Enhanced formation support.

**Author contribution statement:** Generating the research idea; statement of the research problem; analysis of research results and data preparation; wrote the draft manuscript: D.L.Q.

**Acknowledgments:** This paper was funded by the IPR research group.

**Competing interest statement:** The authors declare no conflict of interest.

## References

1. Chatterjee, A.; Kustamsi, A. Geomechanical model update in Hai Thach field, off shore Vietnam. Technical document, 2015.
2. Dzung, T.Q.; Tung, H.T. The model to predict sand production for production wells at Cuu Long basin. *Sci. Technol. Dev. HCM National Univ.* **2014**, *17(3)*, 172–178.
3. Willson, S.M.; Moschovidis, Z.A.; Cameron, J.R. Palmer, new model for predicting the rate of sand production. Paper presented at the SPE/ISRM Rock Mechanics Conference, Irving, Texas, 2002.
4. Palmer, I.; Vaziri, H.; Willson, S.; Moschovidis, Z.; Cameron, J.; Ispas, I. Predicting and managing sand production: A new strategy. Paper presented at the SPE Annual Technical Conference and Exhibition, Denver, Colorado, 2003.
5. Bellarby, J. Well completion design, volume 56. Oxford, United Kingdom: Elsevier's Science & Technology Department, 2009.
6. Zare-Reisabadi, M.; Safari-Beidokhti, M.; Kaffash, A.; Bataee, M. Sand production prediction and well completion optimization. *Int. J. Pet. Geosci. Eng.* **2014**, *2(4)*, 361–374.
7. Holt, R.M.; Horsrud, P.; Raaen, A.M.; Risnes, R.; Fjaer, E. petroleum related rock mechanics. 2<sup>nd</sup> Edition. Hungary: Elsevier Publications, 2008.
8. Palmer, I.D.; Higgs, N.; Technologies, H.; Ispas, I.; Baksh, K.; Krieger, K.O.; PLC, B.P. Prediction of sanding using oriented perforations in a deviated well, and validation in the field. Paper presented at the SPE International Symposium and Exhibition on Formation Damage Control, Lafayette, Louisiana, USA, 2006.
9. Sundli, K.C. Prediction of critical drawdown pressure for a gas reservoir prone to sand production in western offshore, India, and its suitability for CO<sub>2</sub> sequestration. *Mar. Pet. Geol.* **2024**, *165*, 106854.
10. Gwamba, G.; Changyin, D.; Bo, Z. Investigating unary, binary and ternary interactive effects on pressure drawdown for optimal sand production prediction. *J. Pet. Sci. Eng.* **2022**, *218*, 111010.
11. Tung, H.T.; Thi, L.T.H.; Nam, T.H.; Quan, L.V.; Cuong, T.V. Applying analytical models to predict the sand production capacity of Miocene gas reservoirs, Hai Thach mine, Nam Con Son basin. *Pet. J.* **2016**, *12*, 16–26.
12. Gharagheizi, F. Prediction of sand production onset in petroleum reservoirs using a reliable classification approach. *Petroleum* **2017**, *3(2)*, 280–285.
13. Abass, H.H.; Habbtar, A.H.; Shebatalhamd, A.; Aramco, S. Sand control during drilling, perforation, completion and production. Paper presented at the Middle East Oil Show, Bahrain, 2003.
14. Ohen, H.A. Calibrated wireline mechanical rock properties model for predicting and preventing wellbore collapse and sanding. Paper presented at the SPE European Formation Damage Conference, The Hague, Netherlands, 2003.
15. Halliburton. Halliburton Sand Control Available online: <https://www.halliburton.com/en/completions/well-completions/sand-control/screen-technology>.
16. Bellarby, J. Well completion design. Aberdeen, 2009.

17. Golan, M.; Whitson, C.H. Well performance. 2<sup>nd</sup> Eds., Prentice Hall, 1996.
18. Li, F. Research on the failure analysis and prediction method of casing deformation under the synergistic effect of sand production and corrosion. *Eng. Fail. Anal.* **2023**, *154*, 107706.
19. Yan, W.; Li, F.; Leng, G.; Wang, H.; Ma, Z.; Yun, B.; Li, X.; Deng, J. Sand control screen erosion-failure prediction method in weakly consolidated sandstone reservoir. *Geoenergy Sci. Eng.* **2023**, *224*, 211616.
20. Aadboy, B.S.; Looyeh, R. Petroleum rock mechanics drilling operations and well design. Second Edition, Gulf Professional Publishing, 2019.

*Research Article*

# **Combining UAV and satellite images to assess forest changes: A case study in Phuoc Thuan commune, Xuyen Moc district, Ba Ria - Vung Tau province in the period 2020-2023**

**Tran Ngoc Huyen Trang<sup>1,2,3\*</sup>, Dao Ngoc Duc<sup>4</sup>, Le Van Trung<sup>1,2</sup>, Vo Le Phu<sup>1,2\*</sup>**

<sup>1</sup> Faculty of Environment and Natural Resources, Ho Chi Minh City University of Technology (HCMUT); [tnhtrang.sdh222@hcmut.edu.vn](mailto:tnhtrang.sdh222@hcmut.edu.vn); [volephu@hcmut.edu.vn](mailto:volephu@hcmut.edu.vn); [lvtrung@hcmut.edu.vn](mailto:lvtrung@hcmut.edu.vn)

<sup>2</sup> Vietnam National University Ho Chi Minh City (VNU-HCM); [tnhtrang.sdh222@hcmut.edu.vn](mailto:tnhtrang.sdh222@hcmut.edu.vn); [volephu@hcmut.edu.vn](mailto:volephu@hcmut.edu.vn); [lvtrung@hcmut.edu.vn](mailto:lvtrung@hcmut.edu.vn)

<sup>3</sup> Department of Geodesy, Cartography and GIS, Ho Chi Minh City University of Natural Resources and Environment; [tnhtrang.sdh222@hcmut.edu.vn](mailto:tnhtrang.sdh222@hcmut.edu.vn)

<sup>4</sup> Long Thanh Protective Forest Management Board; [daongocduc1991@gmail.com](mailto:daongocduc1991@gmail.com)

\*Corresponding author: [tnhtrang.sdh222@hcmut.edu.vn](mailto:tnhtrang.sdh222@hcmut.edu.vn); [volephu@hcmut.edu.vn](mailto:volephu@hcmut.edu.vn);

Tel.: +84–98615481; +84–933902908

Received: 27 May 2024; Accepted: 8 July 2024; Published: 25 September 2024

**Abstract:** In recent years, Unmanned Aerial Vehicles (UAVs) technology has advanced substantially, which created new opportunities in developing monitoring applications for forest resources management. UAVs are capable of flying and capturing at varying altitudes, angles, and attaining precise images. These collected data are continuously, quickly, efficiently, and crucially provide insight into forest health situations. Importantly, these captured images cover other useful factors such as changes in the status of biodiversity, deforestation, and forest recovery. The aim of this study is to combine UAV images with satellite imagery for a powerful tool in monitoring and evaluating forest dynamics and resources. Accordingly, Landsat 8 images in 2020, UAV images 2023 and GIS technology were employed to create a forest map in Xuyen Moc district, Ba Ria - Vung Tau province allowing an evaluation of changes in forest area over a spanning period of 2020-2023. The results indicated that the forest area changed at a rate of 4.1% (9.37 ha) in which the largest change was bare land with a substantial decrease of 8.08 ha meanwhile restored forests increased a remarkable area of 7.85 ha over the period 2020-2023. These changes were detected by overlaying forest maps 2020 and 2023 with the accuracy is 90.6% and Kappa coefficient was 0.87%. The findings suggest that the latest application of UAVs coupled with GIS technology brought significant conveniences with images retrieved from UAVs, providing a quick, reliable and competitive approach to the management practices of forest resources.

**Keywords:** UAV; Forest map; Forest change map; Landsat.

---

## **1. Introduction**

Forests, those priceless natural treasures and the lungs of our planet, play a vital role in the Earth's ecosystem [1–2]. Their influence extends to maintaining natural balance and mitigating climate change. However, forests are under threat, grappling with issues such as habitat loss, illegal logging, and forest fires. To safeguard and sustainably manage these vital ecosystems, monitoring forest developments becomes an essential and crucial task [3–4].

Unmanned Aerial Vehicles (UAVs) have gained popularity across various fields, including agriculture, forestry, surveying and mapping, urban management, and fast delivery of useful information for decision-makers [5–7]. Their efficiency and productivity have made them becoming an indispensable tool for a wide range of environmental and natural resources management. UAVs not only reduce production costs but also enhance accuracy and improve service quality and customer relationships [8]. These applications underscore the significant impact drones have on industries worldwide. Presently, UAV-based applications in the field of forest research encompass a diverse range of tasks, including resource inventory, disease mapping, forest development monitoring, species classification, and fire monitoring and assessment. These applications primarily focus on different domains as enumerated as below.

**Resource inventory:** UAVs are employed to assess and quantify forest resources, including tree density, canopy cover, and vegetation distribution. The study [9] conducted a study by using point clouds and digital elevation models, particularly the Canopy Height Model (CHM), to inventory forests between 2013 and 2015. Estimating tree height using UAV photos provides accurate information about biomass volume, supporting forestry management activities.

**Disease mapping:** By capturing high-resolution imagery, UAVs aid in identifying and mapping diseases affecting trees and other vegetation. The Convolutional Neural Network (CNN) algorithm on UAV images is frequently employed for disease detection in plants. Research has focused on various plant species, with grapes and watermelon being particularly notable. Over 10 types of diseases have been identified, with fungi accounting for more than 60% of cases, while the remainder are caused by viruses, nematodes, and abiotic factors [10].

**Species classification:** UAVs contribute to species identification and classification, crucial for biodiversity monitoring and conservation efforts. In a comparative study using the EfficientNetV2 model alongside other widely used transfer learning models (ResNet50, Xception, DenseNet121, InceptionV3, and MobileNetV2), the results demonstrate that EfficientNetV2 achieves recognition rates of up to 99% for seven plant species. This impressive outcome was achieved by the research team [11].

**Forest development monitoring:** Tracking changes in forest structure, growth, and regeneration over time is facilitated by UAVs. Investigating six forest plots with varying structures, the research reveals that changes in canopy height patterns directly mirror forest degradation. The fine texture corresponds to a uniform distribution of small tree canopies, indicative of ongoing regeneration after overexploitation [12].

**Fire monitoring and assessment:** UAVs play a pivotal role in monitoring forest fires, assessing their impact, and aiding in post-fire recovery efforts. Additionally, UAVs are instrumental in quantifying spatial distances within forested areas and estimating soil movements following harvest activities. The successful deployment of UAVs in forestry hinges on several key features such as Flexibility in flight planning, Cost-effectiveness, Reliability and autonomy, and Timely availability of high-resolution data [13, 14].

Satellite images play a crucial role in monitoring natural resources (water, land, forest), which perform numerous advantages for tracking and safeguarding valuable resources. Satellites equipped with a variety of sensors capture high-resolution imagery of the Earth's surface. Optical sensors provide visible and infrared imagery, while multispectral and hyperspectral sensors collect data across several narrow bands. This enables detailed land cover classification and vegetation analysis [15]. To monitor forest changes from the past (specifically, when UAV images were not available in 2020) up to 2023, Landsat 8 satellite images can be freely downloaded from online platforms [16, 17]. The 8th generation satellite - Landsat 8 was successfully launched into orbit on November 2, 2013. Landsat 8's primary mission is to deliver crucial information across various domains, including energy and water management, forest monitoring, environmental resource assessment, urban planning, disaster

recovery, and agriculture. Multispectral image bands with a 30-meter resolution offer valuable insights for creating forest maps and evaluating forest health [18, 19].

Forest monitoring involves precisely identifying the various types of forests and the land designated for existing forest development. It aims to quantify changes in forest volume over time, considering each forest type and the primary objectives of the campaign. This information is crucial for strategic forest management, protection, and development planning. The process typically includes gathering data on tree density, forest cover, fluctuations in forest area, and other relevant factors such as vegetation, animal species, and environmental conditions [20]. Monitoring forest developments plays a critical role in assessing forest health and management. It enables the detection of forest degradation and identification of threats to the forest environment, including environmental destruction, illegal mining, and forest fires. By collecting data and closely monitoring forests, forest managers and environmental organizations can implement measures to safeguard forests, strengthen their capacity to combat forest fires, and propose effective management policies for the protection and preservation of forest ecosystems [21]. A forest status map is a thematic map that delineates the boundaries of forest status plots based on the current forest classification system. These maps are overlaid onto topographic maps, with each map corresponding to a specific scale. This practice aligns with Clause 6, Article 2 of Circular No. 31/2018/TT-BNNPTNT, issued by the Ministry of Agriculture and Rural Development on November 16, 2018 [22].

The forest change map is a widely employed tool for analyzing, managing, and monitoring forest dynamics. These maps draw upon data from diverse sources, including satellite images, aerial photographs, ground-based measurements, and other geospatial information. By leveraging image analysis techniques and geostatistical methods, forest change maps facilitate the identification, classification, and quantification of forested areas, enabling the assessment of their temporal changes over time [23]. Forest change maps serve the purpose of documenting and monitoring alterations in both the extent and condition of forests within a specific region. These maps offer insights into the fluctuations whether growth or decline of forested areas over time. Researchers, governmental bodies, and environmental organizations rely on these maps to gain an overview of the forest state and track the ecosystem changes occurring within these vital ecosystems [24].

## **2. Materials and Methods**

### *2.1. Study area*

The study area is located in Phuoc Thuan commune, which falls within the Xuyen Moc district of Ba Ria - Vung Tau province, situated in the Southeast region of Vietnam (Figure 1). The study area covers 2.23 km<sup>2</sup> within the total land area of Phuoc Thuan commune, which spans 52.02 km<sup>2</sup>. The forest area of this current study is a part of the renowned primeval forest of Binh Chau - Phuoc Buu. Being referred to as the “green lung” of Xuyen Moc district, this forest area is the harbors of about 800 plant species and over 350 animal species, including several rare and unique inhabitants.

### *2.2. Method for acquiring image data using UAV and creating forest maps in 2023*

UAV data was collected using a DJI Matrice M300 aircraft and a DJI Zenmuse L1 sensor (Figure 2). The Matrice 300 RTK is the most advanced UAV with a range of new safety features, high-tech solution design, expanding capabilities and exploring previously unexplored areas of work. DJI Zenmuse L1 integrates a Livox lidar sensor, high-precision IMU and a 1-inch CMOS sensor camera, 20MP resolution and mechanical shutter on a Zenmuse 3-axis stabilized gimbal. In particular, Zenmuse L1 can also be exploited to create real-time terrain-aware flight paths.



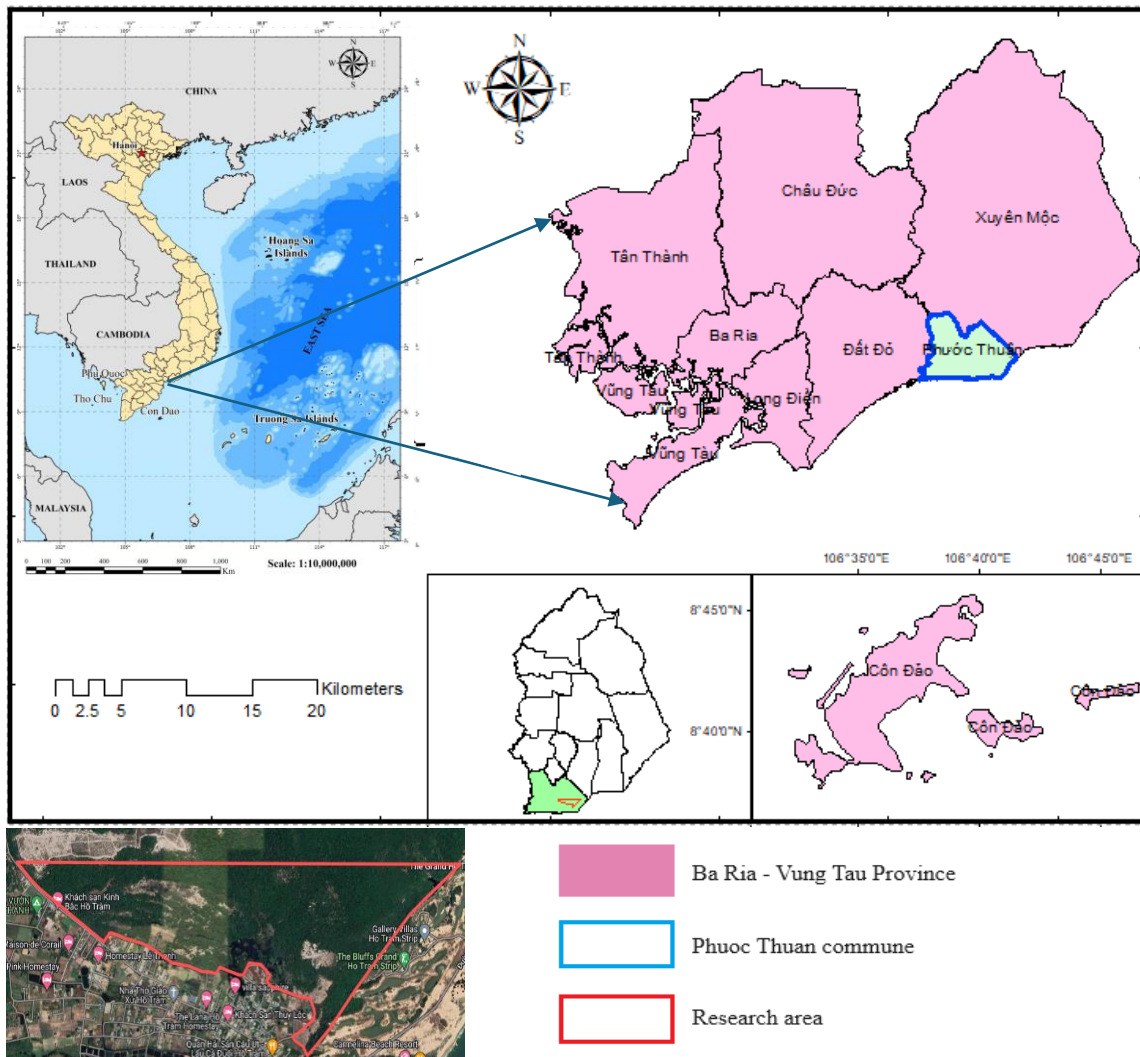


**Figure 1.** The study area is located in Phuoc Thuan commune, Xuyen Moc district, Ba Ria Vung Tau province.



**Figure 2.** DJI Matrice M300 UAV and DJI Zenmuse L1 sensor.

Using two benchmarks of basis cadastral coordinates, specifically Nui Le and Theo Neo, provided by the Survey and Mapping Data Center, serves as the foundation for establishing a base station. This base station facilitates the transmission of signals to the UAV, enabling them to conduct aerial photography using GNSS RTK technology (Figure 3). The Hi-Target V30 satellite positioning device serves as the base station, strategically positioned at the benchmark of basis cadastral coordinates. The base station plays a crucial role in receiving signals from multiple satellites simultaneously, across various frequency bands. Its primary objective is to ensure accuracy. Subsequently, it transmits and corrects signals to the UAV

which now functions as a rover. Throughout the flight and image capture process, the UAV continuously receives satellite signals, akin to the base station on the ground. Simultaneously, it receives correction signals from the base station. By comparing and calculating this information, the UAV derives the most precise results in terms of coordinates and altitude for each image projection center [25, 26].

To survey the entire study area, from November 13 to 14, 2023, we conducted 10 flights at an altitude of 150 meters. Both the overlap along track and the overlap across track were set at 80%. The total implementation time for this comprehensive aerial survey exceeded 7 hours, resulting in a set of 1100 images.

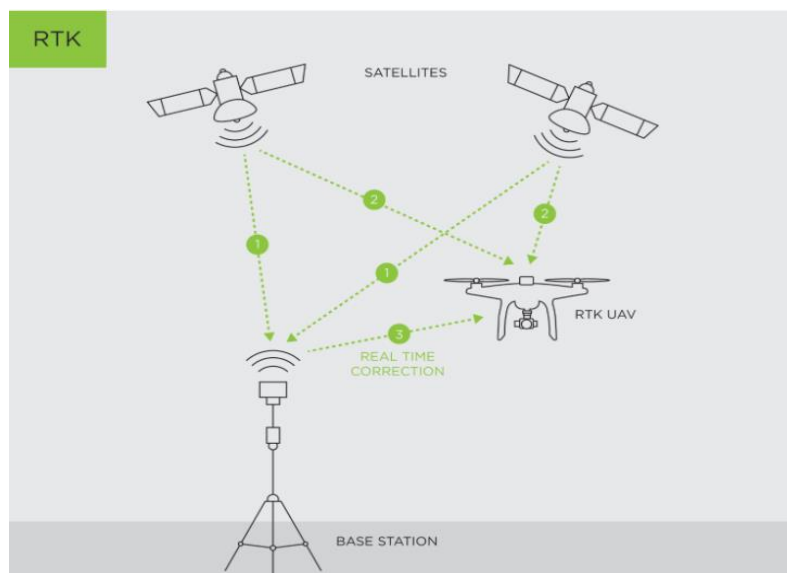



**Figure 3.** The operational principle behind the signal reception of UAV RTK [27].

Agisoft Metashape software was used to process images and create the orthomosaic of the study area. After collecting information about the research area, determine the task of image interpretation. UAV images, with their exceptionally high resolution, reveal distinct characteristics for each class of objects. When observing these images, the unique features of different objects become evident. Use direct reading and drawing diagnostics including color, shape, size, pattern, shadow, texture, indirect standards including distribution standards and relationships between objects to interpret using eyes and then digitize types: water, bare land, recovering forests, growing forests (Table 1).

**Table 1.** Identifying characteristics of the types to be interpreted.

Class	Image on orthomosaic	Identifying characteristics
Water		Ash gray color, very smooth structure.
Bare land		White mixed with green and black spots.
Recovering forests		Light green color, very fine structure.
Growing forests		Green color, smooth structure.

Class	Image on orthomosaic	Identifying characteristics
Old forests		Dark green color, quite smooth structure mixed with black shadow.

After digitizing the data of 5 layers, the forest map in 2023 was edited by using ArcGIS software.

### 2.3. Method for creating forest map in 2020 using satellite images

Download Landsat 8 image dated on 14 November 2020 with radiation correction, orthogonal geometry correction, using ground control points and DEM. Convert the image coordinates to the coordinate system with the local meridian axis of Ba Ria - Vung Tau province which is 107 degrees 45 minutes, then crop the image according to the boundary of the study area.

The Normalized Difference Vegetation Index (NDVI) is a crucial metric in remote sensing and environmental monitoring. It provides valuable insights into vegetation health and density. The NDVI quantifies the greenness or vegetation vigor of an area based on spectral data [28]. It is calculated using the reflectance values from two specific bands: Red band (usually around 650-680 nm wavelength); Near-infrared (NIR) band (typically around 750-900 nm wavelength) [29]. The NDVI formula is as follows:

$$NDVI = \frac{NIR - Red}{NIR + Red} \tag{1}$$

NDVI images are calculated at a resolution equal to that of Landsat 8 images, which is 30 meters. Comparing documents on the boundaries of forest subdivisions reported by the local authority, combined with the opinions of experts in the field of forestry through expert consultation, NDVI thresholds were divided into five classes as shown in Table 2.

**Table 2.** NDVI threshold for forest classification.

Class	NDVI thresholds
Water	$NDVI \leq -0.07$
Bare land	$-0.07 < NDVI \leq -0.01$
Recovering forests	$-0.01 < NDVI \leq 0.05$
Growing forests	$0.05 < NDVI \leq 0.11$
Old forests	$NDVI > 0.11$

Maps created from satellite images always have certain errors that can stem from the image acquisition method of the device’s sensor to the image classification process. Therefore, classification accuracy is often used to evaluate the quality of classified satellite images. Create 277 randomly distributed sample points on the classification results and Google Earth images, then build a classification error matrix.

Forest change map for the period 2020-2023 was created by overlaying the forest map in 2020 and the forest map in 2023. Use the query tool to search for unchanging and changing forest types, then label the areas of the forest change map.

### 3. Results

In 2020, a forest map was created using Landsat 8 satellite imagery. The map’s accuracy was assessed post-classification, utilizing 277 sample points. These points were used to evaluate five distinct land cover types: water, bare land, recovering forest, growing forest, and old forest. The classification accuracy results are documented in Table 3.

**Table 3.** The results of post-classification accuracy assessment.

Land cover type	Classified total	Reference total	Number correct	Producers Accuracy (%)	Users Accuracy (%)
Water	9	9	9	100.0	100.0
Bare land	51	49	48	98.0	94.1
Recovering forests	32	35	30	85.7	93.7
Growing forests	68	85	65	76.5	95.6
Old forests	117	99	99	100.0	84.6

Overall accuracy (%) = 90.6%; Kappa coefficient = 0.87.

The overall accuracy and kappa coefficient, as indicated in Table 3, demonstrate a strong agreement between the classification results and the reference data source. In 2020, a thematic map was created for the study area, covering 2.23 km<sup>2</sup>. Within this area, various land cover types were identified, including water (occupying 0.02 km<sup>2</sup>), bare land (covering 0.34 km<sup>2</sup>), recovering forest (encompassing 0.10 km<sup>2</sup>), growing forest (spanning 0.22 km<sup>2</sup>), and old forest (dominating the landscape at 1.55 km<sup>2</sup>) (Table 4). This comprehensive map provides valuable insights into the distribution and dynamics of land cover within the specific study area.

**Table 4.** Distribution of forest land types in the 2020 forest map.

Land cover type	Number of Polygons	Area (km <sup>2</sup> )	Percentage of Area
Water	6	0.02	0.9
Bare land	111	0.34	15.2
Recovering forests	35	0.10	4.5
Growing forests	55	0.22	9.9
Old forests	53	1.55	69.5
Total	260	2.23	100.0

The 2020 forest map was established in the VN-2000 coordinate system, the map scale is 1:10,000 with map components such as north arrow, location diagram, legend (Figure 4).

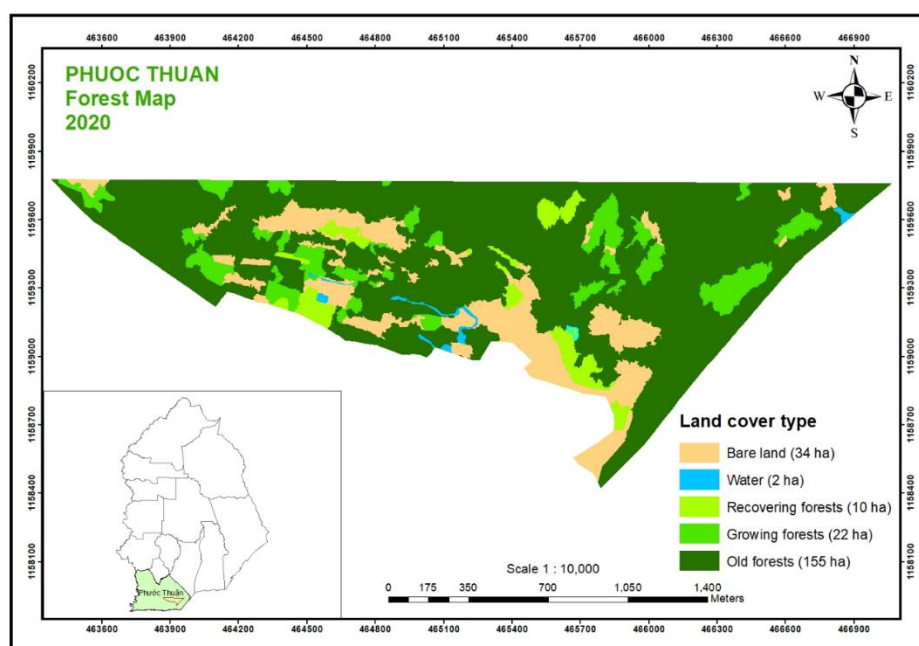


**Figure 4.** Forest map of Phuoc Thuan commune, Xuyen Moc district, Ba Ria - Vung Tau province in 2020.

Derived from an image map with an impressive resolution of 2.89 centimeters, the 2023 forest map exhibits exceptional sharpness. Consequently, the results of interpretation and digitization align remarkably well with the outcomes from field tests. In 2023, the forest

cover spans a total area of 2.23 km<sup>2</sup>. Within this area, water cover constitutes 0.9%, bare land occupies 11.2%, recovering forests account for 8.1%, growing forest encompasses 9.8%, and old forests comprise 70%.

**Table 5.** Distribution of forest land types in the 2023 forest map.

Land cover type	Number of Polygons	Area (km <sup>2</sup> )	Percentage of Area
Water	6	0.02	0.9
Bare land	87	0.25	11.2
Recovering forests	57	0.18	8.1
Growing forests	52	0.22	9.8
Old forests	58	1.56	70.0
<b>Total</b>	<b>260</b>	<b>2.23</b>	<b>100.0</b>

From the forest map in figure 5, the dark green color represents old forests that occupy most of the area in the study area.

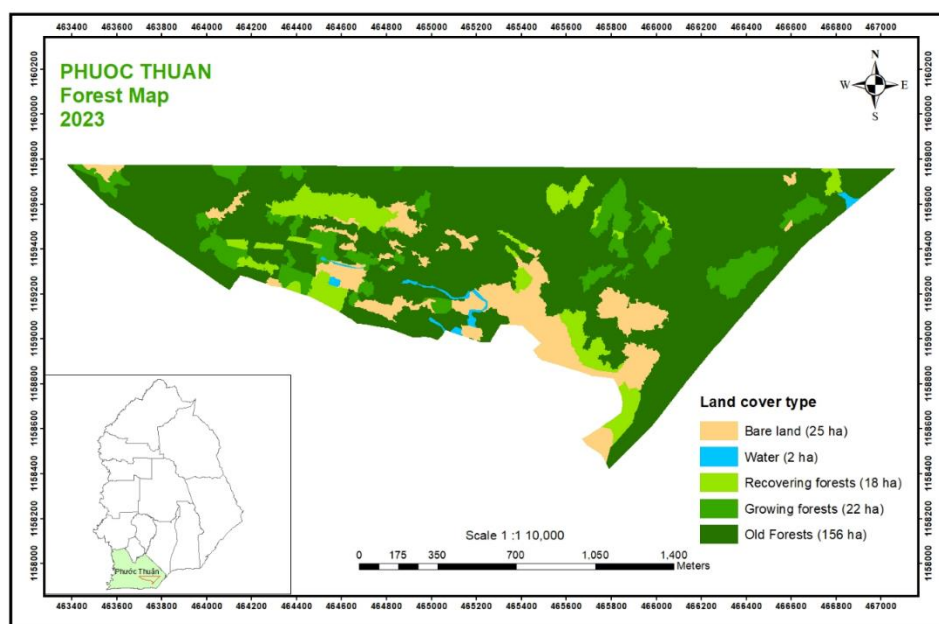


**Figure 5.** Forest map of Phuoc Thuan commune, Xuyen Moc district, Ba Ria - Vung Tau province in 2023.

Overlay the forest map from 2020 with the forest map from 2023 to detect changes in forest types. The variation results on the map in Figure 6 indicate that certain locations within the study area have experienced changes in cover types, as depicted by the scattered red polygons. The water surface did not change during this assessment period. In the period 2020-2023, the forest area to be changed is 9.37 hectares, accounting for 4.1% (Table 6a). Specifically, bare land decreased by a substantial area of 8.08 hectares, while restored forests increased by a remarkable area of 7.85 hectares (which includes the area from bare land changed to recovering forest and from recovering forest to growing forest). Additionally, growing forests had a slight decrease of approximately 0.39 hectares, while old forests increased around 0.62 hectares (Table 6b). These alterations reflect the dynamic and intricate nature of forest ecosystems, where various land categories undergone transformations over time.

**Table 6a.** Changes in land cover types.

ID	Land cover type 2020	Land cover type 2023	Area (ha)
1	Old forests	Bare land	0.11
2	Bare land	Recovering forests	8.19
3	Recovering forests	Growing forests	0.34
4	Growing forests	Old forests	0.73
<b>Total</b>			<b>9.37</b>

**Table 6b.** The change (increase or decrease) in the area of each type of land cover type.

ID	Land cover type	Area (ha)
1	Water	0.00
2	Bare land	-8.08
3	Recovering forests	+7.85
4	Growing forests	-0.39
5	Old forests	+0.62

In the span of three years, Table 6a illustrates a remarkable transition from bare land to recovering forest land. This shift is driven by investments in tree planting to protect the environment for both humans and creatures. Initially in a recovering state, the forest gradually regained ecological balance, growing in height and canopy. It then transitioned to a growing forest. Simultaneously, the forest evolved from a growing to an old forest. However, selective tree cutting occurs even in old forests to prepare space for new saplings, ensuring a balance between regeneration and conservation. This dynamic interplay reflects nature’s intricate dance, emphasizing the need for sustainable forest management.

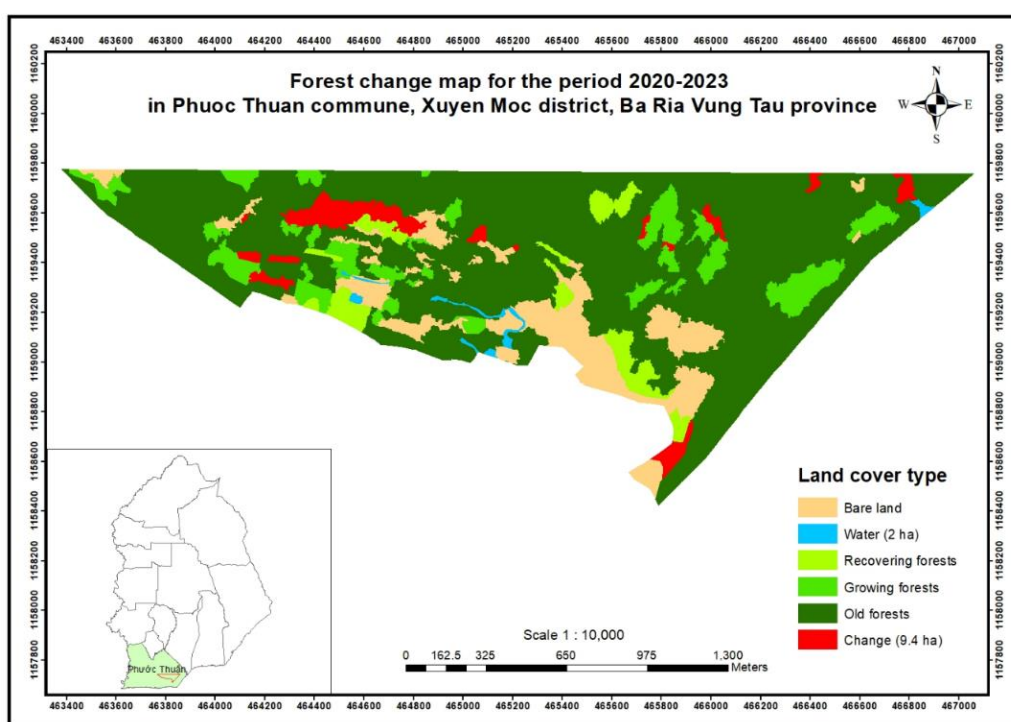


**Figure 6.** Forest changemap for the period 2020-2023.

#### 4. Discussion

The purpose of error matrix for Landsat images is to compare the classification results on Landsat 8 images with Google Earth images (or in the field). The accuracy assessment of the forest by on-site examination (in the field) is not a good idea, because it is impossible to recognize what type of forest when standing in a location in the forest. Instead, we can only see the tree trunks, not the tree canopy. Meanwhile, UAV images have higher resolution than Google Earth images, visual interpretation on UAV images has achieved reliable results. Therefore, the accuracy of the 2023 forest map (by UAV) was not evaluated.

In this study, we examined the synergy of UAV data and Landsat 8 image data from a previous time to assess changes in forest types and other land covers, including water and bare land. Due to the relatively short research period (3 years), only approximately 4.1% of the total land area experienced alterations.

There is a fact that we are examining the feasibility of UAV deployment to monitor forest growth and development over time. Unfortunately, due to the absence of UAV data in 2020,

we had to reply on Landsat 8 data as an alternative. Therefore, this is a limitation of this study in which imagery data is not the same type. Of course, this aspect was mentioned in the Conclusion section for future directions.

Compared to the results from the study [30], it shows that using a combination of UAV images with Quickbird and Ikonos satellite images will result in only a small difference in resolution when overlaying the map, thereby yielding more reasonable results. The 12-year study period also revealed significant changes in forest cover. The results demonstrate the transformation from forest land to urban land or vacant land with different construction forms. While it is necessary to pay for the use of high-resolution satellite images (Quickbird, Ikonos) to achieve similar resolution as UAV images, the Landsat 8 images used in our study are free and can be easily downloaded from the providers' platforms.

## 5. Conclusion

The research findings indicate that various methods can be employed to generate forest maps, including those for monitoring and managing forest changes. In this particular study, both UAV (Unmanned Aerial Vehicle) photos and Landsat 8 satellite images were effectively deployed to create forest maps for the years 2020 and 2023. The analysis revealed that 9.37 hectares of forest area underwent changes during this period, accounting for approximately 4.1% of the total area investigated. The observed movement trend aligns with natural laws and forest development principles. Forest maps generated using UAVs offer flexibility, allowing access to challenging and hazardous areas such as mudflats or regions with dense tree root networks. Additionally, UAVs capture images at a finer resolution compared to satellite images, resulting in better image quality. While UAVs provide advantages, using satellite images remains more cost-effective, and satellite data also facilitates the collection of historical image data. In summary, both UAVs and satellite imagery play crucial roles in forest mapping, each offering distinct benefits. Researchers and forest managers can choose the most suitable approach based on their specific needs and available resources.

In order to objectively assess the accuracy, it is essential to consider the differences in resolution and accuracy between UAV images and Landsat 8 satellite images, which are essential factors to perform a better and more reliable forest map. In order to achieve these, field verification data becomes crucial. Additionally, expanding the assessment over multiple periods and a broader research area will allow us to demonstrate the progression of changes and understand the underlying patterns of forest dynamics within the region. Notably, these study's results reflect the imagery data from Landsat 8 (2020) and UAV (2023), which are not the same type of data. These results provided an acceptable insight into perspective of data absent in the past. However, future directions of this barrier can be solved to tackle missing and absence of past data and information. Once this obstruction is unveiled, the data to provide the management practices of forest and natural resources will be more reliable and is a huge improvement.

**Authors' contribution:** Conceptualization: T.N.H.T., D.N.D., V.L.P., L.V.T.; Methodology: T.N.H.T., D.N.D., V.L.P., L.V.T.; Data processing: T.N.H.T., D.N.D.; Writing - original draft: T.N.H.T., D.N.D., V.L.P., L.V.T.; Writing, reviewing and editing: T.N.H.T., V.L.P.

**Declaration:** The authors collectively declare that this article is the result of their research, not previously published elsewhere, and not copied from previous studies; there is no conflict of interest among the authors.

**Acknowledgements:** The authors would like to express our thankfulness to Ho Chi Minh City University of Technology (HCMUT), VNU-HCM for the support of time and facilities for this study.

## References

1. Paulinus, C.A.; John, J.I.I., Colman, C.I. Our forests, our environment, our sustainable livelihoods. *Eur. J. Acad. Essays*. **2015**, 2(4), 6–19.
2. David, O.E. Importance of forest and trees in sustaining water supply and rainfall. *Niger. J. Educ. Health Technol. Res.* **2016**, 1–8.
3. Per, A.; Terrence, B.; Michael, M. Challenges and solutions for forest biodiversity conservation in Sweden: Assessment of policy, implementation outputs, and consequences. *J. Land*. **2023**, 12(5), 1098.
4. Kandasamy, G.; Sabariswaran, K.; Mathiyazhagan, N. Influences of wildfire on the forest ecosystem and climate change: A comprehensive study. *J. Environ. Res.* **2024**, 240(2), 117537.
5. Mingyang, L.; Yibo, Z.; Chao, H.; Hailong, H. Unmanned aerial vehicles for search and rescue: A survey. *J. Remote Sens.* **2023**, 15(13), 1–35.
6. Tiberiu, P.B.; Gheorghe, F.B.; Constantin, B. The use of drones in forestry. *J. Environ. Sci. Eng.* **2016**, 557–562.
7. Trung, L.V.; Phu, V.L.; Trang, T.N.H.; Khai, H.Q. Opportunities and challenges of UAV application for monitoring the construction progress and updating the geographic database in urban area of Ho Chi Minh City, Vietnam. *IOP Conf. Series: Earth Environ. Sci.* **2023**, 1170, 012014.
8. Asif, A.L.; Awais, K.J.; Rashid, A.L.; Haque, N. Unmanned aerial vehicles: A review. *J. KeAi Chin. Global Impact. Cognit. Robotics.* **2022**, 3, 8–22.
9. Tristan, R.H.; Nicholas, C.C.; Peter, L.M.; Piotr, T.; Patrick, C. Unmanned aerial systems for precision forest inventory purposes: A review and case study. *For. Chron.* **2017**, 93, 71–81.
10. Ruben, C.; Cagatay, C.; Ayalew, K. Plant disease detection using drones in precision agriculture. *Springer - Precis. Agric.* **2023**, 24, 1663–1682.
11. Girma, T.; Isabella, G.; Gianni, G.; Fulvio, G.; Stefano, A.; Ivan, S. Automated identification and classification of plant species in heterogeneous plant areas using unmanned aerial vehicle-collected RGB images and transfer learning. *Drones* **2023**, 7(599), 2–19.
12. Clément, B.; Julie, B.; Pierre, C.; Lilian, B.; Hélène, D.; Johan, O.; Renan, L.R.; Louis, R.; Lucas, M.; Plinio, Läderach, S.P.; Gond, V. UAV-based canopy textures assess changes in forest structure from long-term degradation. *Ecol. Indic.* **2020**, 115, 106386.
13. Chiara, T. et al. Forestry applications of UAVs in Europe: A review. *Int. J. Remote Sens.* **2016**, 33(8-10), 2427–2447.
14. Simon, E. et al. Towards operational UAV-based forest health monitoring: Species identification and crown condition assessment by means of deep learning. *J. Comput. Electron. Agric.* **2024**, 219, 1–17.
15. Sunandana, R. Natural resource management using remote sensing and geographic information systems. *J. Environ. Sci. Eng.* **2023**, 79–91.
16. Amit, K.R.; Nirupama, M.; Akansha, S.; Krishna, K.S. Landsat 8 OLI satellite image classification using convolutional neural network. Proceeding of the International Conference on Computational Intelligence and Data Science (ICCIDS 2019), 2020, pp. 987–993.
17. Ridwan, M.A. et al. Applications of Landsat-8 data: A survey. *Int. J. Eng. Technol.* **2018**, 436–441.
18. Chaudhary, S.K.; Pandey, A.C.; Parida, B.R. Forest fire characterization using Landsat-8 satellite data in Dalma wildlife sanctuary. *J. Remote Sens. Earth Syst. Sci.* **2022**, 5, 230–245.



19. Katsuto, S.; Tetsuji, O.; Nobuya, M. Detecting forest changes using dense Landsat 8 and Sentinel-1 time series data in tropical seasonal forests. *J. Remote Sens.* **2019**, *11*, 1–22.
20. Badea, O.; et al. Forest monitoring - assessment, analysis and warning system for forest ecosystem status. *J. Not. Bot. Horti. Agrobo.* **2013**, *41(2)*, 613–625.
21. Sumalika, B.; Qiongyu, H.; Anupam, A.; Myat, S.M.; Franz-Eugen, A.; Peter, L. A multi sensor approach to forest type mapping for advancing monitoring of sustainable development goals (SDG) in Myanmar. *J. Remote Sens.* **2020**, *12*, 1–21.
22. MARD. Circular No. 31/2018/TT-BNNPTNT of the Ministry of Agriculture and Rural Development: Regulations on forest boundary delineation. 2018.
23. Katsuto, S.; Wataru, M.; Takahisa, F.; Ronald, C. E. Mapping land use/land cover changes and forest disturbances in Vietnam using a Landsat temporal segmentation algorithm. *J. Remote Sens.* **2023**, *15(3)*, 1–17.
24. Hansen, M.C.; Ruth, S.D. Detecting long-term global forest change using continuous fields of tree-cover maps from 8-km advanced very high resolution radiometer (AVHRR) data for the years 1982-99. *J. Ecosystems.* **2004**, *7(7)*, 695–716.
25. Martínez, C.P.; Agüera, V.F.; Carvajal, R.F. Accuracy assessment of RTK/PPK UAV-photogrammetry projects using differential corrections from multiple GNSS fixed base stations. *J. Geocarto Int.* **2023**, *38(1)*, 1–21.
26. Remzi, E.; Remzi, A.; Remzi, A. A comparative analysis of UAV-RTK and UAV-PPK methods in mapping different surface types. *Eur. J. For. Eng.* **2021**, *7(1)*, 12–25.
27. Ferntech Commercial Company. RTK and PPK survey drones, what is the difference? Available online: <https://www.ferntechcommercial.co.nz/news/rtk-and-ppk-survey-drones-what-is-the-difference>.
28. Meeragandhi, G. et al. NDVI: Vegetation change detection using remote sensing and GIS – A case study of Vellore District. Conference: Elsevier Procedia 3<sup>rd</sup> International Conference on Recent Trends in Computing 2015 (ICRTC-2015) At: SRM University, Delhi Campus, 2015, 57, 1199–1210.
29. Bhandari, A.K.; Kumar, A.; Singh, G.H. Feature extraction using normalized difference vegetation index (NDVI): A case study of Jabalpur City. *J. Procedia Technol.* **2012**, *6*, 612–621.
30. Jumaat, N.F.H.; Ahmad, B.; Dutsenwai, H.S.; Land cover change mapping using high resolution satellites and unmanned aerial vehicle. *IOP Conf. Series: Earth Environ. Sci.* **2018**, *169*, 1–6.

# Table of content

- 1** Ninh, L.V.; Tuan, N.H.; Tuan, N.C.; Anh, L.N.; Giang, N.T.; Van, C.T. Applying a two-dimensional open-source hydrodynamic model to evaluate the riverbed change in the upstream of the Cuu Long River, An Giang Province. *J. Hydro-Meteorol.* **2024**, *20*, 1–14.
- 15** Phuc, L.Q.; Ha, L.T.T.; Long, N.Q. Stress distribution under coal pillars in the case of multi-seam mining: A case study at Thong Nhat Coal Mine, Vietnam. *J. Hydro-Meteorol.* **2024**, *20*, 15–23.
- 24** Ha, L.T.T. Multi-sensor points cloud data fusion for 3D building models: A case study in Halong city, Vietnam. *J. Hydro-Meteorol.* **2024**, *20*, 24–36.
- 37** Nhu, N.Y. A review on baseflow separation methods. *J. Hydro-Meteorol.* **2024**, *20*, 37–51.
- 52** Hai, K.V.; Giang, N.T.; Bich, D.T.N. Applying the variable infiltration capacity (VIC) model to reconstructing streamflow data in the Da River basin at Muong Te hydrological station. *J. Hydro-Meteorol.* **2024**, *20*, 52–65.
- 66** Trung, D.T. The integration of GNSS RTK and IMU with extended particle filter. *J. Hydro-Meteorol.* **2024**, *20*, 66–74.
- 75** Duyen, L.Q. Application of geomechanical models to predict sand production and propose well completion solutions for Well X in the Hai Thach field. *J. Hydro-Meteorol.* **2024**, *20*, 75–83.
- 84** Trang, T.N.H.; Duc, D.N.; Trung, T.V.; Phu, V.L. Combining UAV and satellite images to assess forest changes: A case study in Phuoc Thuan commune, Xuyen Moc district, Ba Ria - Vung Tau Province in the period 2020-2023. *J. Hydro-Meteorol.* **2024**, *20*, 84–95.